



**TECHNISCHE
UNIVERSITÄT
WIEN**

DISSERTATION

Simulation of the Flame-Flow Interaction of Dust Explosions in Closed Vessels

ausgeführt zum Zwecke der Erlangung des akademischen Grades
eines Doktors der technischen Wissenschaften eingereicht an der

Technischen Universität Wien
Fakultät für Maschinenwesen und Betriebswissenschaften

von

Clemens Gößnitzer

Matrikelnummer: 01126267

Große Neugasse 22–24/1/15, 1040 Wien, Österreich

unter der Leitung von

ao. Univ.-Prof. Dr. Herbert Steinrück

Institut für Strömungsmechanik und Wärmeübertragung, E322

begutachtet von

assoz. Univ.-Prof. Dr.

Stefan Pirker

Department of Particulate

Flow Modelling

JKU Linz

ao. Univ.-Prof. Dr.

Helfried Steiner

Institut für Strömungslehre

und Wärmeübertragung

TU Graz

Ich nehme zur Kenntnis, dass ich zur Drucklegung meiner Arbeit unter der Bezeichnung 'Dissertation' nur mit Bewilligung der Prüfungskommission berechtigt bin.

Eidesstattliche Erklärung

Ich erkläre an Eides statt, dass die vorliegende Arbeit nach den anerkannten Grundsätzen für wissenschaftliche Abhandlungen von mir selbstständig erstellt wurde. Alle verwendeten Hilfsmittel, insbesondere die zugrunde gelegte Literatur, sind in dieser Arbeit genannt und aufgelistet. Die aus den Quellen wörtlich entnommenen Stellen sind als solche kenntlich gemacht. Das Thema dieser Arbeit wurde von mir bisher weder im In- noch Ausland einem Beurteiler zur Begutachtung in irgendeiner Form als Prüfungsarbeit vorgelegt. Diese Arbeit stimmt mit der von den Begutachtern beurteilten Arbeit überein.

Wien, im April 2019

Clemens Gößnitzer

Abstract

Dust explosions pose a risk for many different industries. Materials which are normally harmless can set off a disastrous deflagration inside closed vessels, due to their dispersion and high specific surface area. To mitigate the effects of such an event, explosion suppression devices can be installed. They detect an explosion, and shoot an extinguishing agent into the vessel, preventing it from rupture.

The commonly used models to predict the behaviour of a dust explosion are based on a one-dimensional approximation. Thus, these models are only valid for perfect spheres where ignition happens in the centre. For vessels of a different geometry, empiric shape factors have to be used. Additionally, the velocity field and the shape of the flame front cannot be predicted. For industrial applications, the correct prediction of the pressure-time evolution of an explosion event is most important.

In this thesis, the models used to design such devices are improved. We make the following assumptions: An explosion happens in a closed vessel. Initially, there is quiescent fluid which is assumed to be an ideal gas. The fuel and oxidiser are premixed. Friction, heat conduction and heat loss to the surroundings are neglected. The flame front is assumed to be infinitely thin. Thus, we consider it to be a gasdynamic discontinuity.

Since the thickness of the flame is neglected, the front is intrinsically unstable. This instability is called Darrieus-Landau instability and was first discovered in the 1940s. However, experiments showed that plane, stable flame fronts are possible. Thus, over the last decades scientists improved the so-called ‘flame sheet’ models, where the flame is infinitely thin. Those improvements included mechanisms of stabilisation.

Dust explosions are inherently turbulent. Turbulence can distort the flame front. Here, an averaged, smooth flame front is assumed. The burning velocity, i.e. the relative velocity of the flame front with respect to the unburnt gas just ahead of it, depends on the local curvature and the thermodynamic state. This is similar to the Markstein model for laminar combustion.

Experimental data show that the typical speeds induced by a deflagration are much smaller than the speed of sound. Thus, an asymptotic expansion with respect to small squares of a reference Mach number leads to negligible errors. However, in that case, major simplifications are achieved: The leading-order pressure and the divergence of the flow field are time-dependent only. Each material element preserves its entropy, except at the flame front, where entropy is produced.

Due to the special structure of the problem, Helmholtz decomposition is applied to the velocity field. This yields a divergence-free and irrotational part of the velocity and a scalar and vector potential. Both potentials are governed by Poisson’s equations. The geometry of the vessel is assumed to have a symmetry axis. Thus, three-dimensional, rotational symmetric simulations are possible.

Abstract

At the flame front, the entropy, the vorticity and the normal velocity experience a jump. To fulfil these jump conditions, Lagrangian mesh points moving with the flow are used. Additionally, a boundary element method, called panel method, is used to find the scalar potential. The vector potential is found by spectral methods, using sine, cosine and Bessel functions.

Two different methods are used to verify the implementation. First, comparison of the full simulations with the one-dimensional theory shows excellent agreement. Second, the results from the linear stability analysis were reproduced using a simpler model, for describing unconfined combustion inside a channel with almost no pressure change.

Comparison of the simulation results with experimental data yields the effective burning velocity at reference state. The available data suggest a linear dependency of the burning velocity on the deflagration index. Additionally, the shape of the flame front and the flow field can be visualised, which cannot be done by the simple one-dimensional approximations. Future extensions could account for different ratios of specific heats in unburnt and burnt gas, or to consider explosion venting and an influence of the vessel walls on the burning velocity.

Kurzfassung

Staubexplosionen stellen für viele Industriezweige eine große Gefahr dar. Aufgrund der feinen Verteilung, und damit einhergehend großen spezifischen Oberfläche können selbst Materialien, die unter normalen Umständen nicht explosiv sind, eine verheerende Deflagration in geschlossenen Behältern auslösen. Um die Auswirkungen eines solchen Ereignisses abzuschwächen, gibt es Explosionsunterdrückungsanlagen. Diese erkennen eine beginnende Explosion, und bringen ein Löschmittel in den Kessel ein, was ein Bersten verhindert.

Die bisher verwendeten Modelle zur Vorhersage von Staubexplosionen basieren auf einer eindimensionalen Vereinfachung, welche nur für einen kugelförmigen Kessel mit zentrischer Zündung gültig ist. Für alle anderen Geometrien müssen empirische Formfaktoren verwendet werden. Weiters kann keine Vorhersage des Geschwindigkeitsfelds oder der Form der Flammenfront gemacht werden. Für industrielle Anwendungen ist die richtige Vorhersage des Druckverlaufs einer Staubexplosion essentiell.

In dieser Arbeit werden die zur Auslegung solcher Anlagen verwendeten Modelle verbessert und erweitert. Die Modellannahmen sind die folgenden: Eine Explosion breite sich in einem geschlossenen Behälter, gefüllt mit ruhendem Fluid, welches als ideales Gas angenommen wird, aus. Edukte der Verbrennung seien ideal vermischt. Reibung, Wärmeleitung und Wärmeverlust an die Umgebung seien vernachlässigbar. Die Flammenfront sei unendlich dünn; sie wird somit als eine gasdynamische Diskontinuität modelliert.

Aufgrund der Annahme, die Dicke der Flamme sei vernachlässigbar klein, entstehen intrinsische Instabilitäten, welche die Front deformieren. Dieses Phänomen, auch Darrius-Landau-Instabilität genannt, wurde zuerst Mitte des vergangenen Jahrhunderts beschrieben. Nachdem in Experimenten aber die Existenz stabiler Flammenfronten gezeigt wurde, entwickelten eine Reihe von Wissenschaftlern verbesserte Modelle, welche Stabilisierungsmechanismen beinhalten.

Staubexplosionen sind inhärent turbulent. Turbulente Schwankungsbewegungen der Geschwindigkeit können zu einer fein strukturieren, rauen Flammenfront führen. Hier betrachten wir eine gemittelte, glatte Flammenfrontfläche. Die Flammengeschwindigkeit, also die relative Geschwindigkeit der Flammenfront bezogen auf die Geschwindigkeit des unverbrannten Gases, hängt von der lokalen Krümmung und dem thermodynamischen Zustand ab. Das Modell ähnelt dem Markstein-Model für laminare Verbrennung.

Der Vergleich mit Experimenten zeigt, dass die typischen Geschwindigkeiten, welche bei Deflagrationen auftreten, sehr viel kleiner sind als die Schallgeschwindigkeit. Daher führt eine asymptotische Entwicklung nach kleinen Quadraten der Mach-Zahl zu einem vernachlässigbaren Fehler, ermöglicht aber wesentliche Vereinfachungen des Modells: So ist der Druck in führender Ordnung nur eine Funktion der Zeit; gleiches gilt für die Divergenz des Geschwindigkeitsfelds. Weiters ist jedes materielle Fluidelement isentrop, ausgenommen direkt an der Flammenfront, wo Entropie produziert wird.

Kurzfassung

Durch die spezielle Struktur des zu lösenden Problems ist eine Aufteilung des Geschwindigkeitsfelds nach Helmholtz in einen divergenz- und einen rotationsfreien Anteil sinnvoll. Dies führt auf zwei zu lösende Poisson-Gleichungen für das Skalar- und Vektorpotential, um die Gesamtgeschwindigkeit zu erhalten. Weiters werden nur Geometrien berücksichtigt, welche eine Symmetrieachse besitzen. Dies ermöglicht dreidimensionale, aber rotationssymmetrische Simulationen.

An der Flammenfront müssen Bedingungen bezüglich des Sprungs der Feldgrößen Entropie, Wirbelstärke und Normalgeschwindigkeit erfüllt werden. Dies geschieht einerseits mittels Lagrange-Gitterpunkten, welche sich mit der Strömung mitbewegen, und andererseits über die Art der Verfolgung der Flammenfront. Das Skalarpotential wird mithilfe von Randelementmethoden, genannt Panel-Verfahren, berechnet. Für die Bestimmung des Vektorpotentials werden spektrale Methoden, Entwicklungen nach Kreis- und Bessel-Funktionen, verwendet.

Um die Implementierung zu verifizieren, wurden zwei Ansätze verfolgt: Einerseits zeigt der Vergleich einfacher Simulationen in einem unendlich langen Zylinder und einer Kugel eine perfekte Übereinstimmung zur eindimensionalen Theorie. Andererseits wurde mittels eines vereinfachten Modells, eine offene Kanalströmung ohne wesentlichen Druckanstieg, die lineare Stabilitätsanalyse nachvollzogen.

Der Vergleich der Simulationsergebnisse mit experimentellen Daten ermöglicht die Bestimmung der effektiven Flammengeschwindigkeit. Die verfügbaren Daten lassen einen linearen Zusammenhang zwischen Flammengeschwindigkeit und Deflagrationsindex vermuten. Weiters kann die Flammenfrontposition und das Strömungsfeld visualisiert werden, etwas, das die eindimensionalen Modelle nicht können. Mögliche Erweiterungen wären die Berücksichtigung von unterschiedlichen Isentropenkoeffizienten in unverbranntem und verbranntem Gas, oder die Berücksichtigung von Explosionsentlüftungen und ein Einfluss der Kesselwand auf die Flammengeschwindigkeit.

Danksagung

Zuallererst gebührt meinem Betreuer, Herbert Steinrück, mein aufrichtiger Dank. Er hat mich während der vergangenen Jahre begleitet, motiviert und mir die Welt der Mathematik ein bisschen näher gebracht. Wenn ich mit einer Frage zu ihm gekommen bin, hat er sich dafür stets Zeit genommen, und hat keine Mühen und Kosten gescheut, ein produktives Umfeld zu schaffen.

Die manchmal sehr heitere, dann wieder hochkonzentrierte Stimmung im Bürozimmer verdanke ich meinen Zimmerkollegen Christiane, Thomas, Georg, Ivo, Markus und Bernhard. Christoph Reichl hat in mühevoller Kleinarbeit letzte Fehler und Unklarheiten in der Arbeit aufgezeigt, und das, obwohl er aus Zeitmangel E-Mails für gewöhnlich zwischen zwei und vier Uhr in der Früh schreibt.

Ein besonderer Dank geht an Tino Linder-Silwester, Johannes Strecha und Georg Meyer von Hoerbiger für die Unterstützung und das Aufzeigen anderer Betrachtungsweisen. In endlosen Diskussionen haben wir nicht nur sehr mathematisch-physikalische Themen besprochen, sondern sind immer wieder zu ganz profanen Dingen des Lebens abgeschweift. Dies hat Motivation gegeben, weiterzumachen, auch wenn der eingeschlagene Weg manchmal als aussichtslos erschienen ist. Georg hat sich, als Experte auf diesem Gebiet, weiters die Mühe gemacht, meine Darstellung der Verbrennungsmodelle kritisch zu hinterfragen und Inkonsistenten und Fehler aufzuzeigen.

Weiters geholfen haben Rob Lade, sowohl mit seiner Gastfreundschaft in England, als auch mit Diskussionen und der Bereitstellung experimenteller Daten, welche in die Arbeit eingegangen sind, und Peter Moore, ein echter Experte auf dem Gebiet der industriellen Staubexplosionsunterdrückung. Thank you, guys!

Diese Arbeit greift zurück auf freie und quelltextoffene Software. Danke an die Entwickler von HDF5, OpenMP, GNU GSL, vim, tmux, i3 und Linux ganz im Allgemeinen.

Ohne die Unterstützung meiner Familie und Freunde wäre ich heute nicht hier, wo ich bin. Ich kann immer auf Hilfe und Rückhalt zählen, sei es durch Lebensweisheiten, gute Ratschläge oder materielle Unterstützung.

Besonderer Dank gilt Monika: Du hast mir nicht nur eine völlig neue Welt der Erlebnisse gezeigt, sondern gibst auch Kraft, Geborgenheit und Sicherheit. Ich hätte nicht gedacht, dass es einen Menschen gibt, der so gut zu mir passt wie du.

Contents

Abstract	iii
Kurzfassung	v
Danksagung	vii
List of Symbols	x
List of Figures	xiii
List of Tables	xv
1 Introduction	1
1.1 State of the Art in Industrial Applications	4
1.2 New Approach	7
1.3 Overview of the Thesis	9
2 Physical Model	10
2.1 Combustion Model	10
2.2 Flow Model	20
2.3 Non-dimensional Formulation	24
2.4 Stability of the Flame Front	27
3 Expansion for Small Mach Numbers	29
3.1 Governing Equations	29
3.2 Leading-order Formulation	31
3.3 Decomposition of the Velocity Field	34
3.4 Jump of the Vorticity	36
4 State of the Art in Industrial Applications	38
4.1 Symmetrical Solutions for an Infinitely Long Cylinder and Sphere	38
4.2 Commonly Used Models in Industry	41
5 Solution Algorithm	45
5.1 Full Problem Formulation	46
5.2 Partition of the Velocity	47
5.3 Solution Procedure	49
5.4 Time Discretisation	49
5.5 Spatial Discretisation	50
5.6 Panel Methods	53

Contents

5.7	Fourier-Bessel Transformations	56
6	Verification	64
6.1	Choice of Numerical Parameters	64
6.2	Comparison with the One-dimensional Model	68
6.3	Comparison with Channel Flow	71
7	Results & Discussion	73
7.1	Flame-flow Interaction	74
7.2	Comparison with Experiments	86
8	Conclusion	94
A	Rotational Symmetric Panel Velocity	97
B	Numerical Details	102
	Bibliography	108
	Lebenslauf	115

List of Symbols

Capital Letters

Symbol	Description
\mathbf{A}	influence matrix
\tilde{E}	activation energy in J
E	complete elliptic integral of the second kind
J_ν	Bessel function of the first kind of order ν
\tilde{K}_{St}	deflagration index in bar m/s
K	complete elliptic integral of the first kind
Ka	Karlovitz number
Le_{eff}	effective Lewis number
\tilde{L}_{ref}	reference length in m
M	Mach number
Ma	Markstein number
O	closed surface
P	leading-order pressure
\tilde{R}	specific gas constant in J/kg K
S_t	(turbulent) stabilisation number
\tilde{T}	temperature in K
U	complex velocity
V	volume
Ze	Zel'dovich number

Lowercase Letters

Symbol	Description
$a, \mathbf{a}, b, \mathbf{b}$	arbitrary scalar or vector quantity
a, b	Fourier coefficients
\tilde{c}	speed of sound in m/s; concentration in kg/m ³
c, d	Fourier-Bessel coefficients
\tilde{c}_v	specific heat at constant volume in J/kg K
e	specific internal energy
h	specific enthalpy
Δh_f	reaction enthalpy
k	wave number
l	length of a panel
\tilde{l}_{diff}	diffusion length scale in m
\tilde{l}_{Ma}	Markstein length in m

List of Symbols

$\tilde{l}_t^{\text{stab.}}$	(turbulent) stabilisation length in m
\mathbf{n}	normal vector
p	pressure
p'	second-order pressure
q	source strength
r^κ	main curvature radius
s	entropy
s_{eff}	effective burning velocity
s_L	laminar burning velocity
s_t	turbulent burning velocity
t	time
\mathbf{u}	velocity
u_r	relative normal velocity of the flame front w.r.t. the unburnt gas
u_s	absolute normal velocity of the flame front
\mathbf{x}	location vector
z	complex location

Greek letters

Symbol	Description
α	growth rate of an instability; angle
β	coefficient for the pressure-dependency of the burning velocity
Δ	initial distance between two moving mesh points
δ	thickness parameter of the flame zone
Δ_{fix}	distance between two non-moving mesh points
ε	squared reference Mach number divided by γ_u
ϵ	thickness parameter of the reaction zone
Γ	flame front
γ	ratio of specific heats
κ	curvature
λ	wave length
λ_{th}	thermal conductivity
ω	vorticity
φ	scalar potential of the velocity
ψ	vector potential of the velocity
ϱ	density
σ	expansion ratio

Superscripts

Symbol	Description
$(*)^{2D}$	two-dimensional
$(*)^{3D}$	three-dimensional
$(*)$	averaged quantity
$(*)^c$	at the centre
$\dot{(*)}$	derivation with respect to time

List of Symbols

$\hat{(*)}$	at the time the material element crossed the flame front
$(*)^{\text{int}}$	interpolated
$(*)^{-1}$	inverse of a matrix
$(*)^{(n)}$	time step n
$(*)^{\text{n}}$	normal component of a vector
$(*)^{\text{t}}$	tangential component of a vector
$\tilde{(*)}$	dimensionful quantity
$(*)^{\text{T}}$	transpose of a matrix

Subscripts

Symbol	Description
$(*)_0, (*)_1$	leading-order and second-order expansion term
$(*)_{\text{avg}}$	average
$(*)_{\text{b}}$	(at the flame front) in the burnt gas
$(*)_{\text{c}}$	critical value
$(*)_{\delta}$	reaction zone thickness
$(*)_{\text{e}}$	end
$(*)_{\eta}$	Kolmogorov scale
$(*)_{\text{f}}$	at/of the flame front
$(*)_{\text{i}}$	initial
$(*)_i, (*)_j$	indices
$(*)_{\text{o}}$	offset
$(*)_{\text{old}}$	old time step
$(*)_{\text{r}}$	component in r direction
$(*)_{\vartheta}$	component in ϑ direction
$(*)_{\text{tot}}$	total
$(*)_{\text{t}}$	turbulent
$(*)_{\text{u}}$	(at the flame front) in the unburnt gas
$(*)_{\text{v}}$	at/of the vessel wall
$(*)_{\text{x}}$	component in x direction
$(*)_{\text{y}}$	component in y direction
$(*)_{\text{z}}$	component in z direction

List of Figures

1.1	Fire triangle and dust explosion pentagon.	1
1.2	Closed vessel protected by a suppression device.	3
1.3	Three different approaches when modeling confined deflagration.	4
1.4	Typical pressure-time curves of gas and dust explosion in a sphere.	6
1.5	An infinitely thin flame front inside a closed vessel.	8
2.1	Possible simplifications of the structure of the flame front.	11
2.2	A wrinkled flame front moves towards the bottom.	13
2.3	Simplified structure of a plane flame front.	14
2.4	Structure of the flame front according to Matalon and Matkowsky.	15
2.5	Regimes of turbulent combustion.	16
2.6	The turbulent burning velocity.	17
2.7	Flame front velocity and jump of normal velocity at the flame front.	22
2.8	A control volume which encloses the flame front.	23
2.9	Illustration of the unconfined two-dimensional combustion.	27
3.1	Integration path to obtain an expression for the change of pressure.	33
3.2	Tangential material derivative of the velocity at the flame front.	36
4.1	One-dimensional approximation: an infinitely long cylinder or sphere.	38
5.1	Flowchart of the solution procedure.	50
5.2	Spatial discretisation of a rotational symmetric geometry.	51
5.3	Connected marker points $\mathbf{x}_{f,i}$ representing the flame front.	52
5.4	Stabilisation and re-seeding algorithm of the flame front tracking.	53
6.1	Influence of the spatial discretisation on the pressure.	64
6.2	Difference of the pressure and pressure rise for a different spatial discretisation.	65
6.3	Influence of the spatial discretisation on the flame front in a cylinder.	66
6.4	Influence of the spatial discretisation on the velocity in a cylinder.	67
6.5	Comparison of the full simulation and the 1D model for a cylinder.	69
6.6	Comparison of the full simulation and the 1D model for a sphere.	70
6.7	Unconfined combustion: the flame front in a periodic channel.	71
6.8	Verification of the flame front tracking algorithm.	72
7.1	Overview of the visualisation of the simulation results.	73
7.2	Influence of z_1 on the pressure in a cylinder.	75
7.3	Influence of z_1 on the shape of the flame front in a cylinder.	75
7.4	Influence of the aspect ratio on the shape flame front in a cylinder.	76
7.5	Influence of the aspect ratio on the pressure in a cylinder.	76

List of Figures

7.6	Influence of z_i on the pressure in a complex geometry.	77
7.7	Pressure-time and pressure rise-time curves of the full and 1D model.	78
7.8	Influence of Δh_f on the pressure in a complex geometry.	78
7.9	Influence of z_i on the shape of the flame front in a complex geometry.	79
7.10	Influence of Δh_f on the shape of the flame front in a complex geometry.	80
7.11	Influence of z_i on the flow field in a cylinder.	81
7.12	Overlay of flame front positions for three different cylindrical vessels.	82
7.13	Influence of the aspect ratio on the flow field in a cylinder.	83
7.14	Influence of z_i on the flow field in a complex geometry.	84
7.15	Influence of Δh_f on the flow field in a complex geometry.	85
7.16	Geometry of the vessel used for the simulations.	87
7.17	The influence of \tilde{K}_{St} on \tilde{s}_{eff}^0	88
7.18	Pressure-time curves of the simulation and experiment no. A16.	88
7.19	Pressure-time curves of the simulation and experiment no. A19.	89
7.20	Pressure-time curves of the simulation and experiment no. A21.	89
7.21	Pressure-time curves of the simulation and experiment no. D1.	90
7.22	Pressure-time curves of the simulation and experiment no. D2.	90
7.23	Pressure-time curves of the simulation and experiment no. D4.	91
7.24	Pressure-time curves of the simulation and experiment no. D5.	91
7.25	Pressure-time curves of the simulation and experiment no. C2.	92
7.26	Pressure-time curves of the simulation and experiment no. C3.	92
7.27	Pressure-time curves of the simulation and experiment no. C4.	93
7.28	Pressure-time curves of the simulation and experiment no. C6.	93
A.1	A rotational symmetric panel is a truncated cone.	98
B.1	The radius of curvature r_1^k at a flame front point.	102
B.2	Circumscribed sphere inside a truncated cone.	103

List of Tables

1.1	Casualties caused by dust explosions in the USA.	2
1.2	Casualties caused by dust explosions in the Federal Republic of Germany.	2
1.3	Classification of the hazard of suspended dust.	5
2.1	Overview of the different models for the laminar burning velocity.	12
7.1	List of experiments and simulation parameters.	86
B.1	Command line options for the flamier program.	107

1. Introduction

When dealing with fine-grained, suspended dust inside closed geometries, there is always the risk of an explosion. The earliest report in literature of a so-called ‘dust explosion’ dates back as early as 1785 [1]. On 14th December of that year, a flour warehouse was damaged by a rather small explosion of wheat flour in Turin, Italy. The dry weather resulted in a low moisture content of the organic powder, and a gas lamp ignited the suspended particles.

Back then, the hazard of suspended, explosible and small particles was not very well known. Nowadays, many different industries, like metal, wood, food, coal and mines, pharmaceutical and plastics industries are affected by the risk of a dust explosion. Therefore, men and women responsible for the safety of industrial plants have to be aware of the risk and possible mitigation strategies against dust explosions. The five factors leading to a dust explosion are given in Fig. 1.1b, which is valid for both detonations and deflagrations. Since many dust explosions are of the second type, this work deals only with dust deflagrations. A more physical reasoning for considering only deflagrations is given in Chapter 3.

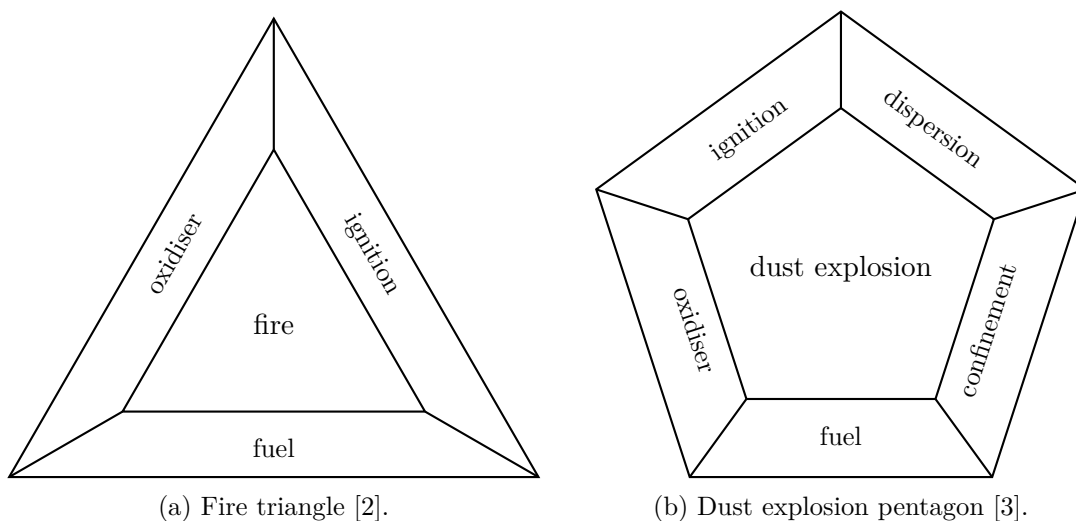


Figure 1.1.: (a) Fire triangle and (b) dust explosion pentagon. When one of the factors that are necessary to cause an explosion are not present, no ignition and fire can happen.

In the last century, dust explosions killed hundreds of people in many different industries. Tabs. 1.1 and 1.2 show the deaths caused by dust explosion events in the United States of America between 1900–1956 and in Western Germany between 1965–1980, respectively. Thus, over the last decades, there were a vast number of publications, technical reports

1. Introduction

and standards published, all of them trying to answer the question of how to recognise and evaluate the risk, and how to prevent loss and damage to people and material.

Table 1.1.: Casualties caused by dust explosions in the USA between 1900–1956, sorted by industry type [1, Tab. 1.3].

industry	number of explosions	fatalities	injured	material loss
wood and bark	162	38	160	\$11.4 mio
food and feed	577	409	1061	\$75.8 mio
metals	80	108	198	\$3.2 mio
plastics	61	44	121	\$3.7 mio
coal excl. mines	63	30	37	\$1.6 mio
paper	9	0	0	\$0.5 mio
others	171	47	193	\$4.3 mio
	1123	676	1770	\$100.4 mio

There are three different strategies to reduce the chance of an explosion or to lower its impact on workers and equipment: (I) preventing a dust-air mixture from becoming explosible, by e.g. using inert gas or lowering the concentration of dust, (II) removing possible sources of ignitions, like electrical spark discharge or hot surfaces, and (III) mitigating the impact of an explosion [4]. Here, we focus on the third approach by providing better models and numerical tools for the calculation of explosion events. The five necessary factors to cause a dust explosion [3] are forming the dust explosion pentagon, shown in Fig. 1.1b. For gas fires, only three preconditions are needed to cause an explosion [2]. Thus, this is also called the fire triangle, and shown in Fig. 1.1a.

Table 1.2.: Casualties caused by dust explosions in the Federal Republic of Germany between 1965–1980, sorted by industry type [1, Tab. 1.4].

industry	number of explosions	fatalities	injured
wood	113	12	124
food and feed	88	38	127
metals	47	18	91
plastics	46	18	98
coal and peat	33	7	39
paper	7	0	0
others	23	10	13
	357	103	492

Different approaches are possible to prevent a dust explosion from becoming a disaster. In principle, all technical equipment could be designed to withstand the explosion pressure, i.e. the maximum pressure which occurs after complete combustion of the explosible material. While this method is successfully used for smaller vessels, it is clear that it cannot be applied to all parts of an industrial plant due to cost, size and weight limitations.

The second strategy is to install vents which open when the pressure inside a vessel exceeds a critical value. This method is simple and reliable, as there are no moving parts involved. However, it cannot be applied in case of toxic materials and the venting itself can also be dangerous to people near the venting location.

1. Introduction

The third approach is to suppress an already starting explosion, as shown in Fig. 1.2. When an explosion is detected, the suppression device is activated. It shoots an extinguishing agent into the vessel, which quenches the explosion. While this method has proven to be very effective, it is much more involved and complex than the first two options.

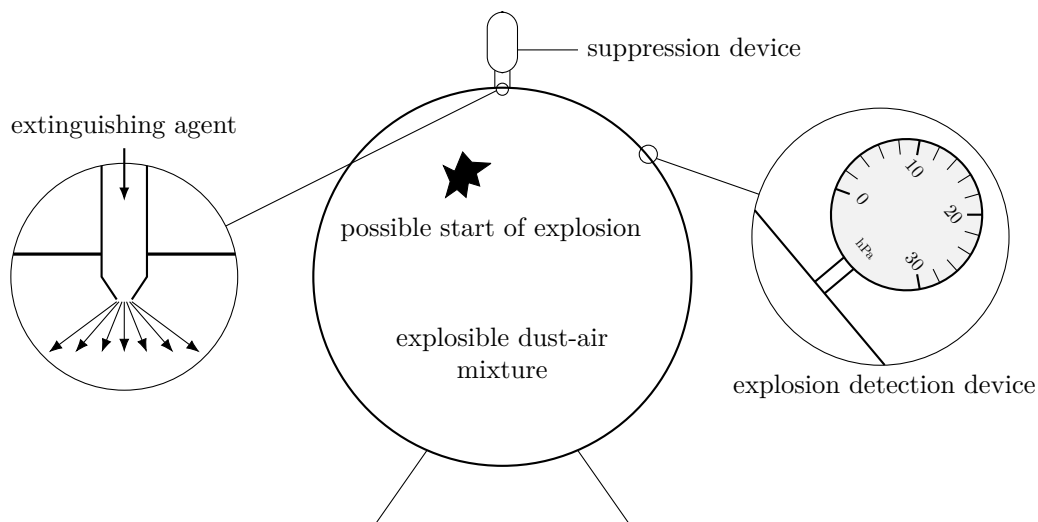


Figure 1.2.: Closed vessel containing a suspended, explosible dust-air mixture. It is protected by a suppression device on top (detail on the left), and an explosion detection system (right).

All countermeasures against gas and dust explosions rely on models to predict the key properties of such an event: the location and propagation of the flame front, the rate of pressure rise in the vessel and the maximum pressure. The level of detail, illustrated in Fig. 1.3, can range from very simple, zero- or one-dimensional approximations up to models with hundreds of chemical reactions combined with computational fluid dynamics (CFD).

When looking into literature, a gap between industrial application and scientific research is apparent: On one hand, models for gas combustion processes have become very detailed and complex [5, 6], as shown in Fig. 1.3 on the right side. They include models for chemical equilibria and kinetics, account for mass and heat transport and many different species. Additionally, the flame front has to be resolved numerically. Additionally, models with an infinitely thin flame front are also common in three-dimensional computational fluid dynamics simulations of laminar combustion. However, most numerical front tracking algorithms lead to a smeared interface.

On the other hand, one-dimensional approximations [1, 7, 8] are used in industry, providing fast and easy-to-understand models for the design of explosion countermeasures [9]. Those methods by themselves cannot account for non-spherical geometries. Instead, empirical shape parameters have to be used. Furthermore, they assume isentropic or isothermal conditions and neglect the thickness of the flame front, as outlined in Fig. 1.3 on the left.

The approach shown in the middle of Fig. 1.3 combines both model types. The flame front is assumed to be infinitely thin, but the flame-flow interaction and influence of the vessel walls are not neglected.

1. Introduction

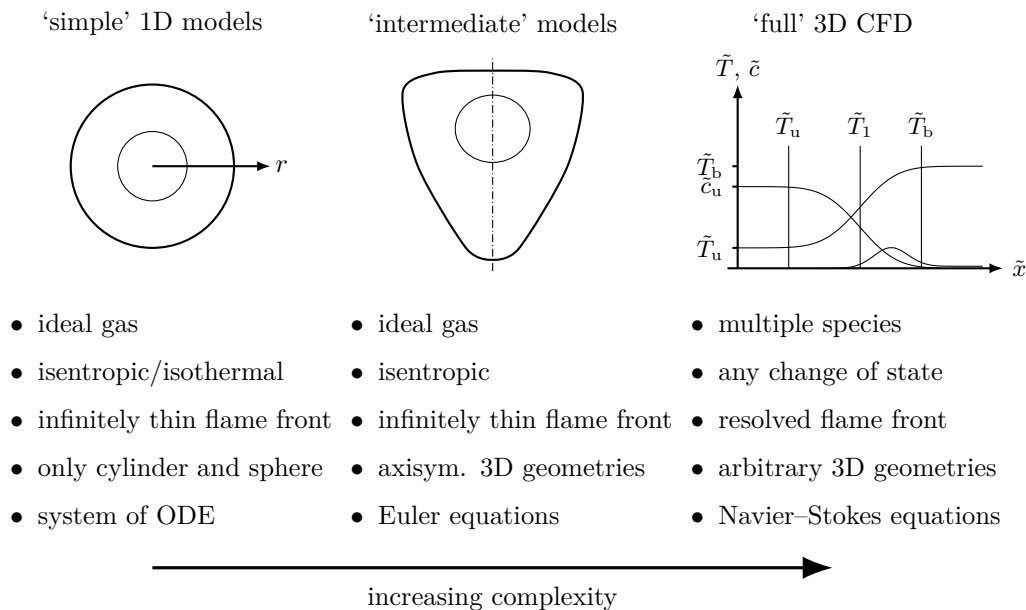


Figure 1.3.: Three different approaches when modeling confined deflagration.

1.1. State of the Art in Industrial Applications

The aim in all models currently used in the process industry is the correct prediction of the time-pressure curve [7, 4, 1, 8]. The main approach is to derive semi-analytical expressions for the rate of pressure rise for centric explosions inside a sphere [10, 11, 12, 13]. Most commonly used are so-called integral models. By applying the total mass and energy balance for unburnt and burnt gas, a non-linear, ordinary differential equation for the pressure is derived [8]. Many integral models make at least the following assumptions [1]: (I) the flame front is infinitely thin (except for the three-zone models [11]), (II) the burning velocity is small compared to the speed of sound, implying a spatially uniform pressure and (III) the explosible fluid is an ideal gas with material parameters that do not depend on pressure or temperature.

In contrast to theoretical modelling, the experimental investigation of dust explosions is very well established. Beginning in the 1960s at the US Bureau of Mines, there have been many different, standardised apparatus developed. One of the first was the so-called Hartmann bomb, a 1.2 L, cylindrical vessel. However, the cylindrical shape caused much heat losses to the surrounding, and distortion of the flame front from the spherical shape. Additionally, the possibility for upscaling the experimental results to larger, industrial-sized vessels was limited. In the 1980s, a 20 L sphere became the most used testing device to determine the properties of dispersed dusts. It was standardised later [14]. It is commonly seen as the apparatus with the smallest volume that provides results for reliable upscaling [15]. Thousands of different dusts have been tested and analysed experimentally, using standard test bombs [16]. Nowadays, standard dust explosion experiments are also done using a 1 m³ sphere [17].

For industrial applications, the deflagration index \tilde{K}_{St} plays an important role to quantify the hazard and strength of a dust explosion. It is defined as the product of the maximum

1. Introduction

Table 1.3.: Classification of the hazard of suspended dust by the deflagration index [18].

dust explosion class	\tilde{K}_{St} , bar m/s	characteristics	typical material [19]
St 0	0	no explosion	silica
St 1	1 to 200	weak explosion	charcoal, sulfur, sugar
St 2	200 to 300	strong explosion	cellulose, wood flour
St 3	> 300	very strong explosion	aluminium, magnesium

rate of pressure rise $(d\tilde{p}/d\tilde{t})_{\max}$ multiplied by the cubic root of the vessel volume $\tilde{V}_v^{1/3}$:

$$\tilde{K}_{St} = \left(\frac{d\tilde{p}}{d\tilde{t}} \right)_{\max} \tilde{V}_v^{1/3}. \quad (1.1)$$

The tilde denotes that a quantity is dimensionful. The most common unit of \tilde{K}_{St} is bar m/s. It allows to classify the strength of a dust explosion, see Tab. 1.3. In practice, the deflagration index is not directly determined from experimental data, but extracted from a fit of a one-dimensional approximation to the experiments. Many different models used in the industry suggest that \tilde{K}_{St} is a parameter to quantify a dust and the initial turbulence. It is independent of the geometry of the vessel [1].

Other important characteristic quantities for dust explosions are the lower explosion limit, the maximum pressure after complete, adiabatic combustion \tilde{p}_{\max} , the concentration of the dust particles and the burning velocity \tilde{s}_{eff} [20, 21].

Eq. (1.1) is also called the ‘cubic root law’, and for one-dimensional integral models, the maximum rate of pressure change occurs at the end of the explosion [22]. It is used for upscaling the experimental results, which are often obtained in rather small vessels, to vessel sizes relevant to the industry [4]. However, the ‘cubic root’ law is only valid under the assumptions made in the beginning of this section. Additionally, upscaling requires that both vessels are geometrically similar.

Errors in upscaling become significant for relative flame thicknesses of above 1% [23], which is defined as the actual flame thickness divided by the characteristic vessel length, e.g. the (equivalence) radius of the vessel.

In industrial applications, dust-air mixtures are commonly described as ideal gas with modified material parameters. This approach is chosen because modelling dust explosions in every detail is almost impossible: One would have to consider particle burning, multiphase flow and radiation [8], to name just a few examples showing the complexity of the physical phenomena. Such a level of detail is unfeasible in industrial applications. Additionally, the approach of treating the millions of differently sized, suspended particles and air as one fluid is working remarkably well, as comparison of model results with experimental data have shown [8].

Due to the different nature of gas and dust deflagrations, the flame thickness is larger in the latter case under the same conditions (pressure, temperature). For gases, the range is typically below one centimetre [24]. For dust explosions, the flame is often much thicker than 10 cm [23]. This results in a point of inflection in the pressure-time curve of confined dust combustion. The maximum rate of pressure rise is no longer at the end of the explosion, but occurs earlier, as seen in Fig. 1.4b. This makes the deflagration index

1. Introduction

unavailable using only experimental data. Thus, the results from a one-dimensional model that approximates the pressure-time curve in the early stages of the combustion process is needed. However, the numeric value of \tilde{K}_{St} depends on the choice of model [8], making comparisons between different approaches impossible.

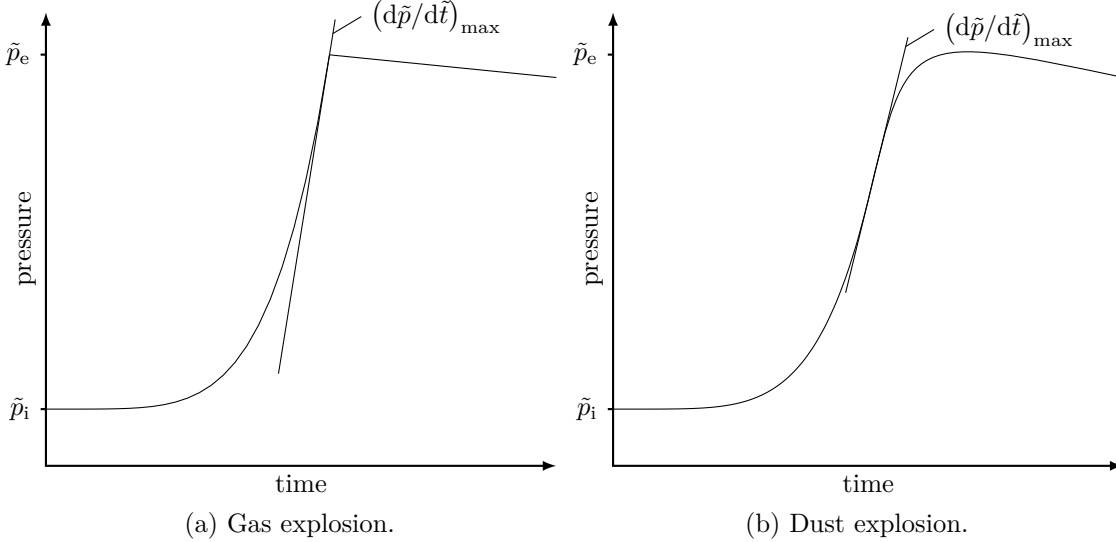


Figure 1.4.: Schematic diagram of typical pressure-time curves of a (a) gas explosion [25] and (b) dust explosion [1] in a sphere with centric ignition. In the case of a gas explosion, the rate of maximum pressure rise is near the end of the explosion, since the flame is usually very thin. For dust explosions, the reaction zone is much thicker and the maximum rate of pressure rise is much earlier.

The point of inflection in the pressure-time curve for dust explosions is caused by the finite and rather large flame thickness. Consider two spherical explosions: For one, the flame front shall be very thin. The rate of pressure rise is proportional to the surface area of the flame front. Since the flame front is thin, the influence of the vessel walls are negligible even when the flame front is very close to the wall. This results in a pressure-time history shown in Fig. 1.4a.

Now, assume that the flame front has a significant thickness. Then, parts of the flame already start to touch the vessel wall during earlier stages of the explosion. This results in a reduced combustion rate, and the maximum rate of pressure rise occurs at an earlier point of time during the explosion event, shown in Fig. 1.4b. Other factors which lead to a point of inflection in the pressure-time curve are an eccentric ignition, a non-spherical vessel shape and heat loss to the surroundings.

Another important difference between gas and dust deflagrations is the presence of turbulence [26, 27]. Dust particles have to remain suspended in the gas phase, to be ignitable. Thus, without turbulence, there would be no dust explosions. Contrary, premixed gas explosions can occur even in a quiescent fluid. Thus, laminar deflagration is only known for gas combustion.

With the increasing computational possibilities, numerous studies using three-dimensional CFD methods were published in recent years. Van Wingerden used an existing combustion simulation code, FLACS, and implemented a dust explosion model [28]. The burning

1. Introduction

velocity was assumed to increase linearly with the intensity of the turbulence, and it also depends on the temperature. However, no particles were modeled. Instead, the dust particles were approximated by a fluid phase.

In the early 2000s, there was a project funded by the European Union [29] to develop a CFD tool, called ‘Dust Explosion Simulation Code (DESC)’, to predict dust explosion behaviour in complex geometries [30]. However, the program is not publicly available.

Collecutt et al. simulated the explosion of an underground coal dust explosion event [31]. Additionally, they model an active explosion barrier consisting of a ring of water injectors. Instead of considering individual, micron-sized dust particles, the authors tracked parcels of particles, where each parcel consisted of many particles. The exchange of heat, momentum, energy and mass between parcels and the gas phase was considered as well, and a model was used to account for the energy transfer by radiation. Since their model was rather complex, the spatial discretisation was limited and computation times were high.

Bind et al. modeled gas and dust explosions inside a 20 L apparatus [32]. Their simulation was done with the commercial software Fluent 6.3.26. They modeled the dust particles as fluid phase. Thus, micro-scale particle effects were neglected.

Murillo and colleagues have investigated the behaviour of suspended particles and the influence of the ignition delay on the distribution of the particles [33, 34]. They modeled aluminium particles, using the commercial CFD tool Fluent. No explosion or chemical reactions were present in the simulations. Instead, the authors focused on characterising dust-air mixtures and validation with experimental data.

CFD simulations enable industrial researchers to study fundamental aspects of dust dispersion, flame-flow interaction and the influence of a non-spherical vessel geometry without relying on empirical shape parameters. Empirical shape parameters, often expressed as the surface ratio of the vessel compared to the surface of the equivalence sphere, are used in integral models to account for the non-spherical vessel shape.

However, the computational demand for fully three-dimensional simulations is very high. Thus, this approach often requires simplifications, like averaging over discrete volumes instead of resolving individual particles. Additionally, CFD simulations require meshing of the computational domain, and post-processing, which can be very time consuming for complex geometries. For commercial CFD codes, costs for licenses have to be considered.

1.2. New Approach

Here, we extend the one-dimensional integral models to account for flame-flow interaction and the influence of a non-spherical vessel shape. So, all assumptions made in those types of models are also applied here. It is out of scope for this thesis to derive new or improve currently used combustion models for gas or dust deflagrations.

The main new aspects of this work are the coupling of the flame with the flow and the influence of the geometry of the vessel compared to the one-dimensional models, which do not have to consider the momentum balance. Here, the local balance equations, the full, compressible Euler equations for low Mach number flow are solved. This allows to include the influence of the vessel walls from first principles. Thus, no empirical shape parameters

1. Introduction

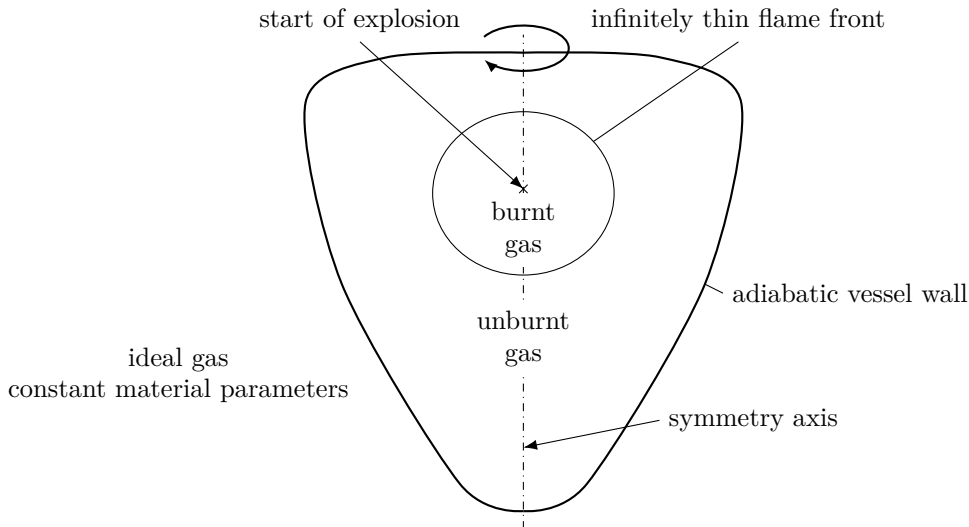


Figure 1.5.: An infinitely thin flame front inside a closed vessel. The geometry and explosion are assumed to be rotational symmetric about the dash-dotted axis.

are necessary. Furthermore, the numerics allow an easy and straightforward extension to any description of the burning velocity.

One assumption is that the flame front is infinitely thin, the so-called ‘flame sheet’ model. Here, the flame front separates fresh, unburnt gas from already combusted, hot burnt gas. Since this approach yields a hydrodynamically unstable flame front [35], an additional stabilisation mechanism has to be included. One-dimensional models do not need such a mechanism, because there, the symmetry constraints do not allow any instability to develop.

Furthermore, the vessel geometry is assumed to be symmetric about a rotation axis, see Fig. 1.5. This is reasonable since many vessels in industry can be approximated by such geometries. Additionally, gravity, viscosity and heat conduction are neglected, which leads to an isentropic model.

Laminar combustion is only known for premixed gases. In theory, it could also be possible for dusts in zero gravity environments. There, dust particles do not settle down. Under normal conditions, turbulence is needed to distribute the small particles into air, and to keep them suspended. Turbulence interacts with the flame front, and leads to a wrinkled flame front. Here, we assume an average flame front position [36] which moves with an effective burning velocity \tilde{s}_{eff} . It accounts for all influences of turbulence and increased combustion rate due to flame front wrinkling, chemical reactions and composition, thermodynamic state and so on. Thus, the stabilisation mechanism is assumed to be sufficiently strong to keep the flame front smooth. Details are given in Section 2.1.

Eckhoff [37] gives an overview over expected future trends in dust explosion research. In the conclusions, he states that ‘substantial progress is foreseen in *mathematical modelling of dust cloud generation and flame propagation processes in dust clouds*. It is anticipated that such models will gradually replace conventional empirical equations’ (emphasis by the original author). In this thesis, we develop a new, simple yet very helpful mathematical

1. Introduction

procedure to answer the question, how the flame interacts with the flow and boundaries, i.e. the walls of the vessel.

1.3. Overview of the Thesis

In Chapter 2, we present a full description of the model, i.e. all governing equations, boundary and jump conditions and kinematics of the flame front. There, we keep the formulation as general as possible without any restrictions regarding the geometry of the vessel. Also, we discuss the stability of the plane, infinitely thin flame front in unconfined combustion.

In Chapter 3, we assume low Mach number flow and expand all quantities with respect to a small reference Mach number. Thus, the resulting equations are simplified. This expansion leads to interesting results, e.g. that the pressure depends on time only in leading order. After applying Helmholtz decomposition on the velocity field, the equations governing the flow field reduce to two different types of Poisson's equations for the scalar and vector potential.

In Chapter 4, the one-dimensional, symmetric solutions for an infinitely long cylinder and a sphere are presented. They are used to verify the results of the full simulations. Additionally, three commonly used models in the process industry are described in more detail.

In Chapter 5, the numerical algorithm is explained. We give an overview of the temporal and spatial discretisation. The assumption of equal ratios of specific heats in unburnt and burnt gas is introduced. Also, the velocity field is partitioned, which leads to smaller and easier-to-solve sub-problems. In order for this procedure to work, the solution procedure consists of multiple steps. The spatial discretisation method is closely adapted to the structure of the governing equations. Next, the algorithm for the tracking of the flame front is explained. It is tracked with marker points which move with the front. Since this algorithm can become unstable, and the flame front itself is unstable, we present a re-seeding and stabilisation algorithm for the moving of the marker points as well. Then, the solution algorithm for the Poisson's equations are presented. Details are given to solve Laplace's and Poisson's equation, using boundary element methods, called panel methods, and Fourier-Bessel transformations. Additionally, the interpolation from a moving mesh to an equally spaced, fixed Cartesian mesh is explained.

In Chapter 6, the influence of the spatial discretisation on the solution is discussed. Then, the implementation is verified by comparing the solution obtained by the full implementation with the one-dimensional models. Additionally, the results of the linear stability analysis are reproduced, using a channel geometry under (almost) isobaric conditions.

In Chapter 7, results are presented for the flame-flow interaction and comparison with experiments are given. The shape of the flame front and the flow field is visualised for different vessel geometries, initial explosion locations and reaction enthalpies. The comparison with experimental data yields values for the burning velocity, which seems to increase linearly with the deflagration index.

In Chapter 8, the main findings and conclusions of this thesis are outlined. We discuss the new aspects of this work, and possible future improvements are given. Also, some limitations of the model and the numerical implementation are discussed.

2. Physical Model

This work aims to make a natural extension of one-dimensional global integral models to include the effect of flame-flow interaction and geometry influence. Thus, a combustion model and a flow model are needed. The first one leads to a relation for the burning velocity, whereas the second one yields the balance equations and jump relations.

2.1. Combustion Model

When modelling premixed combustion, there are many different phenomena that have to be considered: chemical reactions, including reaction rates and equilibria, flame-flow interaction, turbulence, species transport, heat and mass transfer in the form of molecular diffusion. Thus, performing a very detailed analysis can only be done for basic combustion processes under simple boundary and initial conditions.

For example, a detailed chemical reaction scheme for the combustion of methane, called GRI-Mech 3.0, includes more than 300 reactions and 50 different species [38]. When taking into account that methane is the simplest hydrocarbon, it is clear that more complex chemical reactions cannot be modelled in every detail. Thus, models for the combustion of higher hydrocarbons are not as detailed as GRI-Mech 3.0 [39, 40, 41].

Dust explosions are heterogeneous reactions, i.e. reactions involving liquid or solid reactants. Additionally, many phenomena have to be considered: diffusion of the oxidiser to the solid surface, external and internal heat transfer, pyrolysis and change of size of the particle [8]. One can imagine that finding a model that can describe a cloud of millions of differently sized, burning particles is out of reach even for today's supercomputers.

The 'flame sheet' approximation, shown in Fig. 2.1a, is the state of the art in modeling of flame propagations in the process industry. It reduces combustion and chemical reactions to the burning velocity \tilde{s}_{eff} and the reaction enthalpy $\Delta\tilde{h}_f$. The burning velocity is defined as the relative normal velocity of the infinitely thin flame front with respect to the velocity of the unburnt gas just ahead of the front. Thus, it is a measure of the local burning rate, and in general depends on many different things, including the chemical reaction scheme, the thermodynamic state and flow conditions. The assumption of an infinitely thin flame front leads to a problem of hydrodynamical nature: The combustion process reduces to the propagation of a surface where heat is instantaneously released.

Another possible approximation are the 'reaction sheet' models, shown in Fig. 2.1b. They resolve a finite-size, outer transport zone, where the concentration of the fuel and oxidiser is reduced, and the fluid is pre-heated. The actual combustion takes place in the infinitely thin reaction sheet. The third main approach is to resolve the reaction zone as well, see Fig. 2.1c. This requires a detailed description of the chemical reactions inside the usually very thin reaction zone.

2. Physical Model

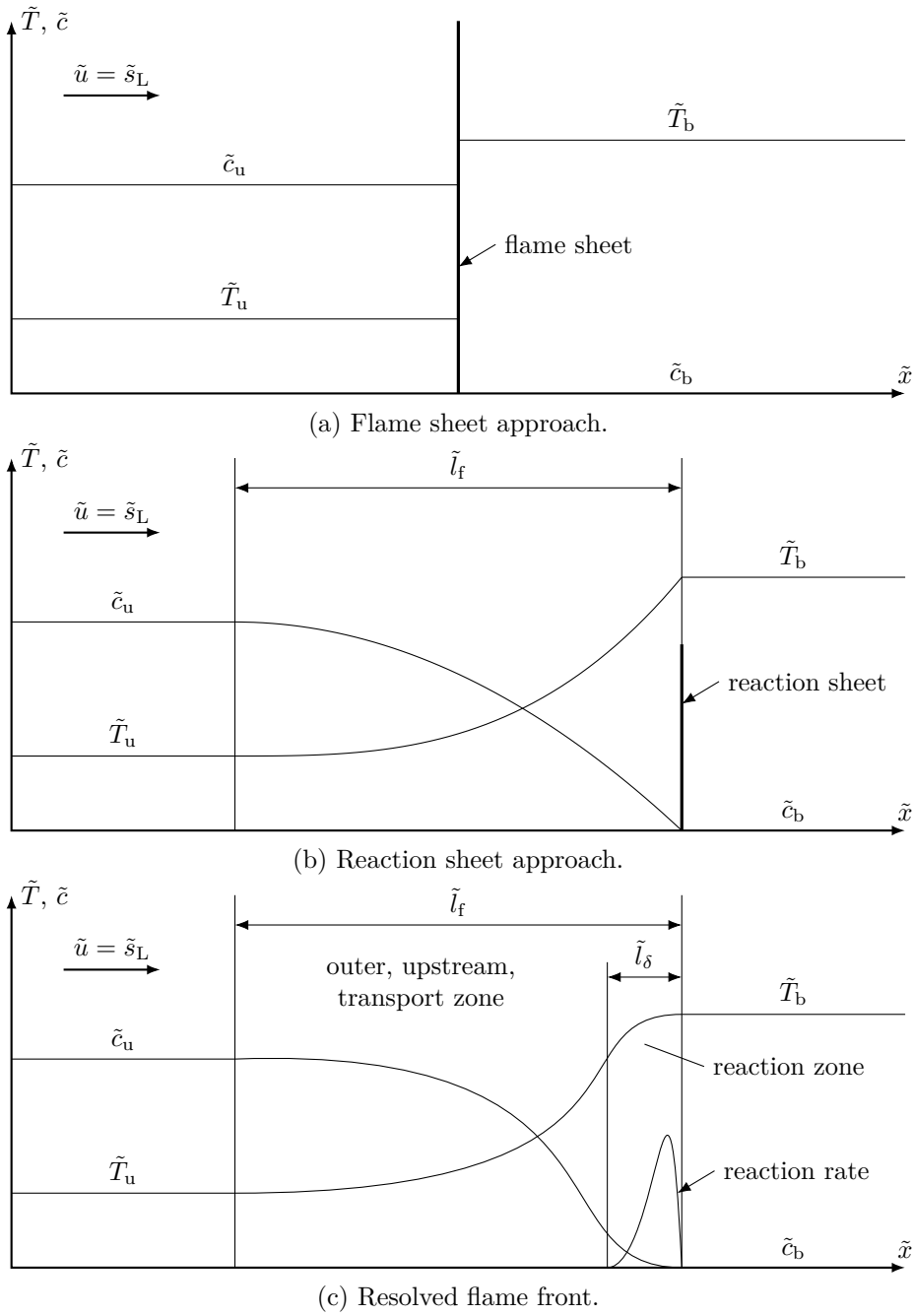


Figure 2.1.: Possible simplifications of the structure of the flame front in laminar, pre-mixed, plane, unconfined and steady combustion [5, Fig. 7.2.1]. (a) A flame sheet model does not resolve any flame structure. (b) A reaction sheet model assumes that the chemical reactions take place in an infinitely thin zone, and the fluid is pre-heated in a finite-sized pre-heat zone. (c) The resolved flame front has a transport zone and a thin reaction zone.

2. Physical Model

When dealing with turbulent combustion, an effective flame speed \tilde{s}_{eff} is assumed which includes all influences of turbulence: flow distortion, additional wrinkling and a higher burning rate. In general, the effective flame speed is higher than the laminar burning velocity, $\tilde{s}_{\text{eff}} > \tilde{s}_L$ [42]. The literature review at the beginning of this chapter focuses on three different topics: (I) models for laminar combustion, (II) influences of turbulence on combustion and (III) influence of the thermodynamic state on the burning velocity.

Models for the Laminar Burning Velocity

Many different approaches have been developed over the last 80 years to model the laminar burning velocity \tilde{s}_L for gas explosions. The simplest possible assumption, introduced by Darrieus [43] and Landau [44], is to assume that the burning velocity is constant. However, this leads to a very pronounced instability which eventually wrinkles the flame front. Such strong instabilities contradict observation from experiments [35], where stable, plane flame fronts have been reproduced. To remedy this problem, stabilisation mechanisms have been included into the model. Some approaches use ad-hoc assumptions [45, 46, 47], and some derive \tilde{s}_L from first principles [48, 49, 50, 51].

Table 2.1.: Overview of the different models for the laminar burning velocity, adapted from [51, Tab. 1]. Not all models can capture all different instability types, and provide stabilisation mechanisms. DL: Darrieus & Landau [43, 44]; M: Markstein [45]; KDKW: Karlovitz et al. [46]; E: Eckhaus [47]; S: Sivashinsky [48]; CW: Clavin & Williams [50]; MM: Matalon & Matkowsky [49]; CMK: Class, Matkowsky and Klimenko [52].

initials of authors	DL	M	KDKW	E	S	CW	MM	CMK
postulated (p)/derived (d)	p	p	p	p	d	d	d	d
flame speed relation								
stretch χ /curv. c /strain s	const	c	χ	c, s	—	χ	χ	—
ode/pde in time t , space \mathbf{x}	—	—	—	—	t	—	—	t, \mathbf{x}
jump conditions								
Darrieus–Landau	+	+	+	+	+	+	+	+
surface compression	—	—	—	—	—	—	+	+
Marangoni	—	—	—	—	—	—	—	+
instabilities								
	n.c. not captured; stabilisation impossible (–)/possible (+)							
Darrieus–Landau	—	+	+	+	+	+	+	+
cellular	n.c.	n.c.	n.c.	n.c.	—	+	+	+
pulsating	n.c.	n.c.	n.c.	n.c.	—	n.c.	n.c.	+

From a hydrodynamical point of view, all models presented here assume that the flame front is infinitely thin. Thus, for the flow, the flame is a sharp interface, where density, velocity and pressure experience a jump. However, some consider the structure of the flame front by means of asymptotic expansion. An overview over the models presented in this section is given in Tab. 2.1.

All flame sheet models experience different kinds of instabilities and most include stabilisation mechanisms. There are three different kind of instabilities observed: the Darrieus–Landau instability, cellular and pulsating flames. The first one is present in all models

2. Physical Model

and is due to the hydrodynamical instability when treating the flame as infinitely thin. Cellular flames contain separated, luminous regions, also called cells and can appear in the Bunsen burner flame. Pulsating flames occur when heat conduction is considered, and the activation energy exceeds a critical value [53].

In 1951, Markstein [45] postulated the existence of a phenomenological quantity and a dependency of \tilde{s}_L on the local curvature of the flame front:

$$\tilde{s}_L = \left(1 - \mu \tilde{L} \tilde{\kappa} + \dots\right) \tilde{s}_L^0.$$

\tilde{s}_L^0 is the burning velocity of the plane flame front, μ is an empirical dimensionless parameter, \tilde{L} is a characteristic length of the order of the flame thickness and $\tilde{\kappa}$ is the local curvature of the flame front. With his empirical extension, he introduced a low-pass filter mechanism: High-frequency perturbations are damped. This leads to a partially stable, wrinkled flame front, where cusps can form, pointing towards the burnt gas, as shown in Fig. 2.2. For stabilisation, μ must be positive. However, for some fuels, this does not hold, leading to amplified instabilities and cell formation occurs faster [6]. Later, the product $\mu \tilde{L}$ was called the Markstein length \tilde{l}_{Ma} . Since Markstein postulated the relation for the burning velocity, the determination of μ and \tilde{L} is not possible with his approach. Later, with the help of asymptotic analysis of the structure of the flame front, it was possible to derive the Markstein length for laminar flow with a simple reaction mechanism [35]:

$$\tilde{l}_{Ma} = \left(\frac{\sigma}{\sigma - 1} \int_1^\sigma \frac{\lambda_{th}(x)}{x} dx + \frac{(Le_{eff} - 1) Ze}{2(\sigma - 1)} \int_1^\sigma \frac{\lambda_{th}(x)}{x} \ln \frac{\sigma - 1}{x - 1} dx \right) \tilde{l}_{diff}. \quad (2.1)$$

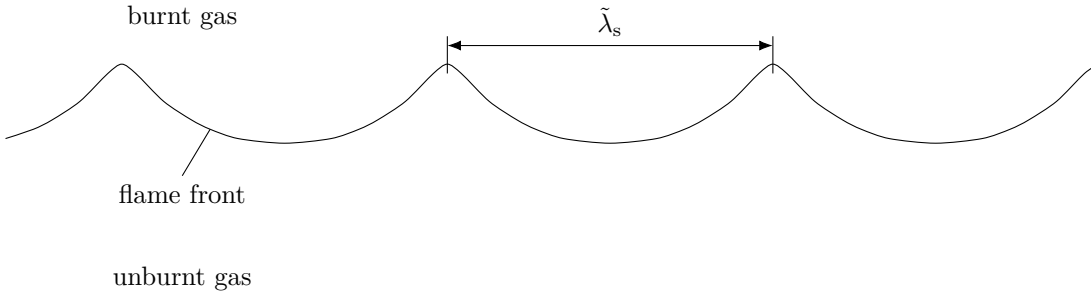


Figure 2.2.: A wrinkled flame front moves towards the bottom. The most unstable wavelength is $\tilde{\lambda}_s$, assuming that the Markstein model is used.

Ze is the Zel'dovich number, a parameter which relates activation energy to the temperature of the burnt gas, Le_{eff} is the effective Lewis number (ratio of thermal to mass diffusivity), a weighted average of the individual Lewis numbers of the fuel and oxidiser, σ is the expansion ratio, i.e. the density of the unburnt gas divided by the density of the burnt gas, λ_{th} is the thermal conductivity, which depends on the temperature, and \tilde{l}_{diff} is the diffusion length scale. Note, that Eq. (2.1) is not a universal expression; depending on the choice of reference state, and reaction mechanism, the Markstein length is different [54].

Karlovitz et al. [46], from the US Bureau of Mines, assumed that the laminar burning velocity was influenced by the velocity gradient of the flow, i.e. the flame stretch. They

2. Physical Model

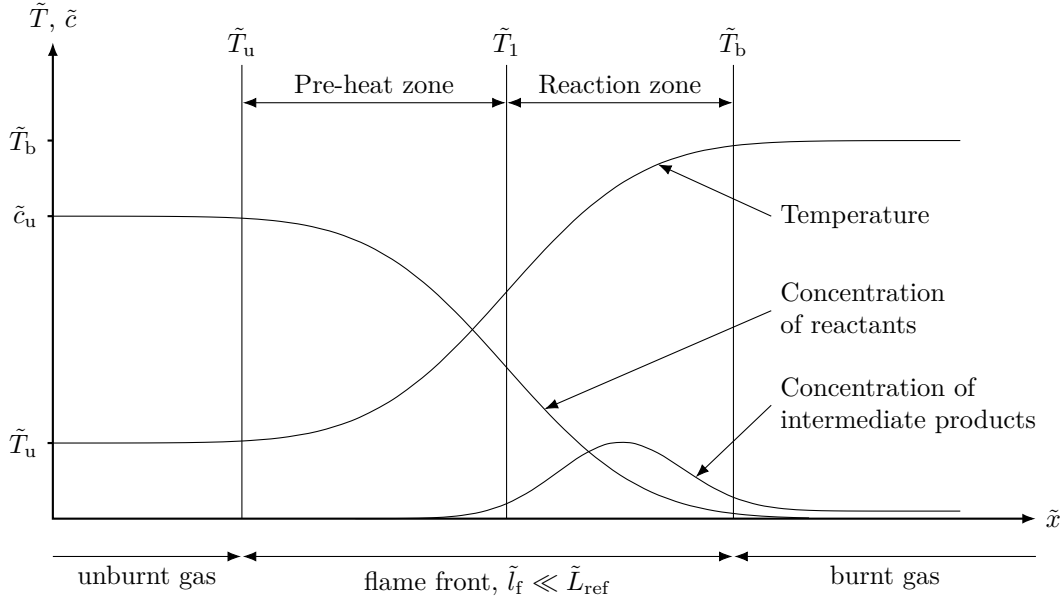


Figure 2.3.: Simplified structure of a plane flame front. In the pre-heat zone, the temperature of the gas rises due to heat conduction. Due to the strong dependence of the reaction rate on temperature, chemical reactions only take place inside the reaction zone [55], which is normally much thinner than the pre-heat zone.

write that ‘[f]lame propagation apparently is arrested by the strong velocity gradient of the flow which exists in the boundary layer’, when considering flames in pipes. Arguing that a strong velocity gradient also leads to a flame stretch, the combustion heat released is distributed over a larger volume of burnt gas, and this effect has to lead to a reduced burning velocity. Following their derivations, flame propagation in the vicinity of solid walls can be interrupted due to large velocity gradients.

Similarly, Eckhaus [47] proposed a burning velocity that depends on the local curvature and the acceleration of the flame front. He assumes that the flame front consists of two zones, a pre-heat zone and a reaction zone, as shown in Fig. 2.3. He assumed a simple second-order reaction of fuel and oxidiser forming the products. When considering flow quantities, the flame front can be seen as infinitely thin, implying $\tilde{l}_f \ll \tilde{L}_{ref}$. Again, complete closure of the problem is not possible, since the determination of empirical parameters which appear in the model remains unsolved. Later, Markstein adopted this idea and extended his original model [56].

All three proposed mechanisms are postulated, rather than derived and assume that there is a characteristic length in the order of the flame thickness. Also, not all parameters can be determined consistently within the scope of the models.

One of the first to apply the method of matched asymptotic expansions to account for the structure of the flame front was Sivashinsky [48]. He considered different zones: a very thin reaction zone, a preheat zone, a hydrodynamic structure zone and a dissipative zone. In the hydrodynamic zone, viscosity can be neglected up to leading order of the asymptotic expansion. Thus, the flow is that of an ideal and incompressible fluid. The dissipative zone is conceptually similar to the boundary layer of viscous flow. Here, dissipative effects like viscosity play an important role and have to be considered. The resulting relation for

2. Physical Model

the flame front velocity is an ordinary differential equation in time. With the assumption that one reactant is a weak trace, the reaction reduces to a monomolecular reaction, i.e. a first-order reaction. He considered his model to be valid only for stationary flames, because of stabilisation considerations.

Matalon and Matkowsky also considered the structure of the flame [49]. They assume that the front can be separated into two regions: a thin flame zone, where transport processes dominate, and a much thinner inner reactive zone, where the actual combustion takes place. The thickness of the first zone δ depends on the length scale of diffusion, which is normally small compared to the characteristic length of the problem, thus $\delta \ll 1$. The thickness of the second zone $\epsilon\delta$ is assumed to be very small compared to the first zone, as shown in Fig. 2.4. ϵ is assumed to be inversely proportional to the activation energy of the chemical reaction $\epsilon \propto 1/\bar{E}$. Normally, the reaction activation energy is high, thus $\epsilon \ll 1$. By applying the method of matched asymptotic expansions, they derive a flame speed relation which depends on the stretch of the flame front. Clavin and Williams [50] apply similar concepts, but only consider very small perturbations and nearly uniform flow. Thus, their flame speed relation is a linearisation of the model of Matalon and Matkowsky [52].

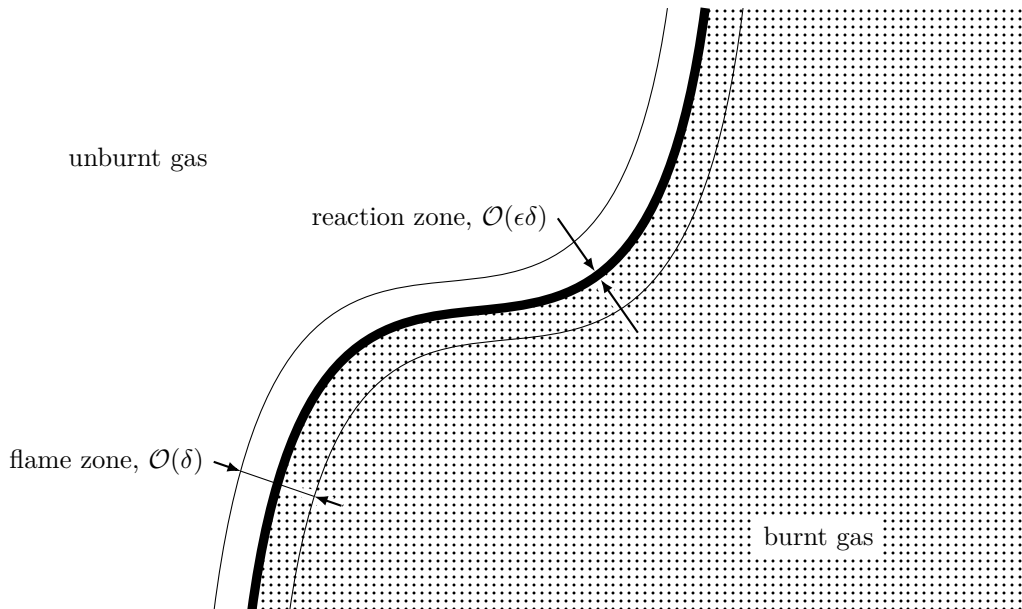


Figure 2.4.: Structure of the flame front according to Matalon and Matkowsky [49, Fig. 3].

In 2003, Class, Matkowsky and Klimenko presented a what they called ‘unified’ model of flames as gasdynamic discontinuities [52]. The advantage of their model is that it is valid for arbitrary Lewis numbers, in contrast to the models of Sivashinsky, valid only for Lewis numbers not near one ($Le \ll 1$ or $Le \gg 1$) and Matalon and Matkowsky/Clavin and Williams, which are valid for Lewis numbers near one ($Le \approx 1$). They derive a new flame speed relation, a partial differential equation in space and time, and new jump conditions for arbitrary Lewis numbers. Their model captures all three types of instabilities, and also provides stabilisation mechanisms and a high-wavenumber cutoff.

Combustion and Turbulence

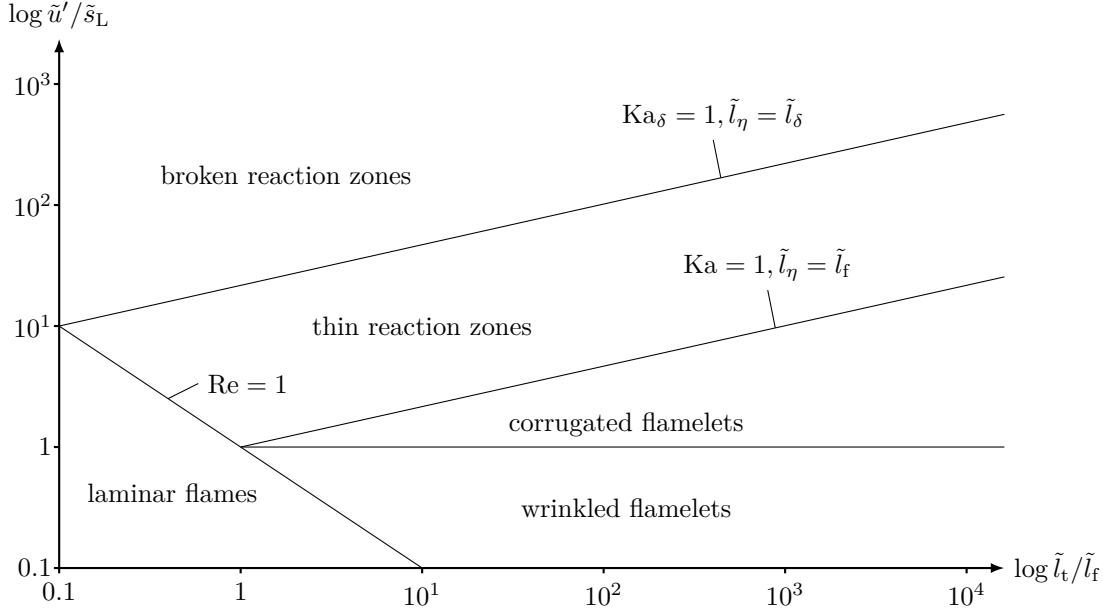


Figure 2.5.: Depending on the ratio of length scales and velocity scales for combustion and turbulence, different regimes are postulated by Peters [36, Fig. 2.8].

Turbulence is a very active field of research. Due to its mathematical complexity, averaging approaches are most commonly used to cope with the properties of turbulent flow [57]. Combustion and turbulence combines two very complex topics. Thus, only very general aspects of turbulent combustion are outlined in this section.

When considering the length scales for combustion and turbulence, many different regimes of combustion can be identified. Length and time scale for combustion are defined as [36, 5]:

$$\tilde{l}_f = \frac{\tilde{\nu}}{\tilde{s}_L}, \quad \tilde{t}_f = \frac{\tilde{\nu}}{\tilde{s}_L^2}. \quad (2.2)$$

$\tilde{\nu}$ is the kinematic viscosity. Assuming a Schmidt number $Sc = \tilde{\nu}/\tilde{D}$ of unity, the viscosity $\tilde{\nu}$ and diffusivity \tilde{D} are interchangeable in Eq. (2.2). With the turbulent integral length scale \tilde{l}_t and the turbulent intensity \tilde{u}' , we define a Reynolds number:

$$Re = \frac{\tilde{u}'\tilde{l}_t}{\tilde{s}_L\tilde{l}_f}. \quad (2.3)$$

The smallest scales in turbulent flow are the Kolmogorov time \tilde{t}_η , length \tilde{l}_η and velocity \tilde{u}_η scales. Those scales are defined as having a Reynolds number of unity [57], and are obtained by dimensional analysis. Thus, two turbulent Karlovitz numbers are introduced. The first one relates the flame scales and the turbulent scales and is defined as [36]:

$$Ka = \frac{\tilde{t}_f}{\tilde{t}_\eta} = \frac{\tilde{l}_f^2}{\tilde{l}_\eta^2} = \frac{\tilde{u}_\eta^2}{\tilde{s}_L^2}. \quad (2.4)$$

2. Physical Model

It compares the flame front time scales with the Kolmogorov time scales of the turbulent flow. Thus, it quantifies the impact of turbulent fluctuations on the outer, pre-heat and diffusion zones. With the help of the reaction zone thickness \tilde{l}_δ , a second Karlovitz number can be defined as the ratio of the reaction zone thickness divided by the Kolmogorov length scale. It is a measure of the impact of the turbulent eddies on the most inner, reaction zone and reads as [36]:

$$\text{Ka}_\delta = \frac{\tilde{l}_\delta^2}{l_\eta^2}. \quad (2.5)$$

Turbulence produces statistical fluctuations of the flow field. Depending on the ratio of the length scales for combustion and turbulence, many different combustion regimes have been identified [36, Fig. 2.8]. Assume that $\text{Re} > 1$: For $\text{Ka} < 1$, the reaction and diffusion processes inside the flame front are much faster than the turbulent time scales. Thus, in this limit, the flame structure is not influenced by the turbulent fluctuations and the entire combustion process is embedded in the much bigger turbulent eddies [36].

When the laminar burning velocity is bigger than the turbulent intensity, a wrinkled flame front develops and the hydrodynamic instabilities dominate. When the turbulence gets more intense, corrugated flamelets are observed up until $\text{Ka} = 1$.

When the flame time is larger than the turbulent time scale, $\text{Ka} > 1$, the outer regions of the flame, i.e. diffusion and pre-heat zones, are influenced by the turbulent fluctuations and thin reaction zones develop.

When the typical size of the turbulent eddies is in the order or smaller than the reaction zone thickness, the most inner, reaction zone is heavily influenced by turbulence. This implies that $\text{Ka}_\delta > 1$, and the influence of the turbulent fluctuations on the chemical reactions becomes important. Thus, the presence of turbulence leads to quenching and re-ignition. This regime is dominated by broken reaction zones.

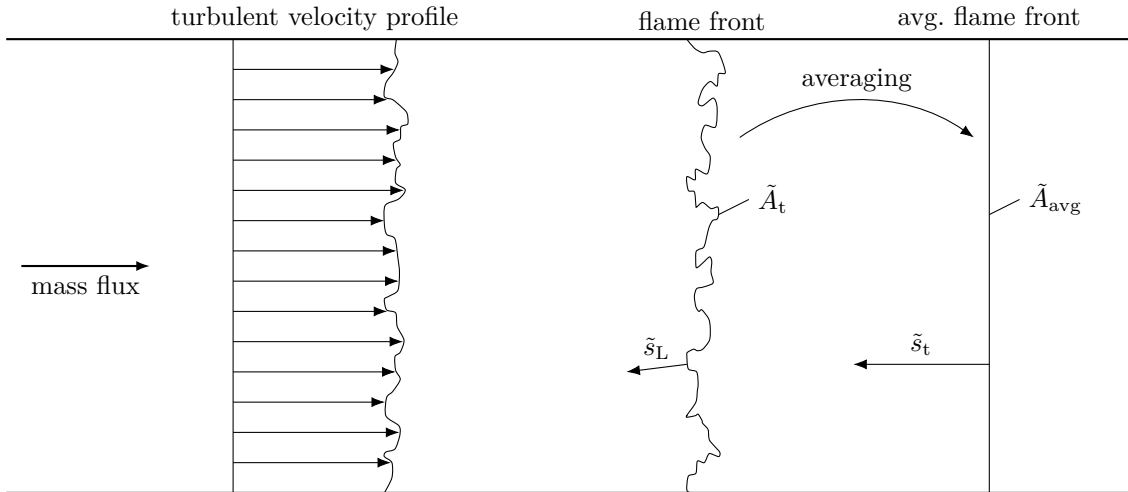


Figure 2.6.: The turbulent burning velocity is defined as the relative velocity of an averaged flame front. Here, a stationary averaged flame is shown. The unburnt gas comes from the left with a turbulent velocity profile [36, Fig. 2.21].

2. Physical Model

To simplify the analysis of premixed, turbulent combustion, an average flame front can be defined, as shown in Fig. 2.6. Note, that for $Ka_\delta > 1$, this approach cannot be justified anymore. The average flame front has a uniform speed, which is chosen such that the mass flux of burning fluid remains the same [36]:

$$\tilde{s}_L \tilde{A}_t \tilde{\varrho}_u = \tilde{s}_t \tilde{A}_{\text{avg}} \tilde{\varrho}_u. \quad (2.6)$$

Since the turbulent flame front is wrinkled, $\tilde{A}_t > \tilde{A}_{\text{avg}}$, the turbulent burning velocity is bigger than the laminar burning velocity $\tilde{s}_t > \tilde{s}_L$.

Dependency of the Flame Speed on the Thermodynamic State

All models presented so far assume unconfined combustion. When modelling combustion inside a closed geometry, however, the pressure rises considerably. When also considering the influence of the vessel walls, this renders the problem of confined combustion more difficult than the open-channel, almost constant pressure combustion. An additional relation to obtain the change of pressure is required. Furthermore, the strong dependency of the burning velocity on the thermodynamic state has to be considered [5, 58, 59]. In the following, empirical relationships which include dependencies on both pressure \tilde{p} and temperature of the unburnt gas \tilde{T}_u are reproduced from literature.

It is common practise to fit relations which express the dependency of the burning velocity on the thermodynamic state to experimental data. One commonly used relation for the dependency of the burning velocity on temperature and pressure is [60, 61, 62, 7]:

$$\tilde{s}_{\text{eff}} = \left(\frac{\tilde{T}_u}{\tilde{T}_{\text{ref}}} \right)^\alpha f(\tilde{p}/\tilde{p}_{\text{ref}}) \tilde{s}_{\text{eff}}^0.$$

α is often found to be 2, and f is an arbitrary function which accounts for the dependency of the burning velocity on the pressure.

Babkin and Kozachenko [60] suggested a laminar burning velocity for methane-air mixtures with 9.5 % methane:

$$\alpha = 2, \quad f(\tilde{p}/\tilde{p}_{\text{ref}}) = 3.18 - 1.53 \log_{10} \frac{\tilde{p}}{\tilde{p}_{\text{ref}}}$$

Reference quantities are $T_{\text{ref}} = 100^\circ\text{C}$ and $\tilde{p}_{\text{ref}} = 1 \text{ atm}$. It is valid for a pressure range from 1 atm to 23 atm. For higher pressures, between 23 atm to 70 atm, they suggest:

$$\alpha = 1.47, \quad f(\tilde{p}/\tilde{p}_{\text{ref}}) = 9.06 \left(\frac{\tilde{p}}{\tilde{p}_{\text{ref}}} \right)^{-0.646+0.0509(\tilde{T}/\tilde{T}_{\text{ref}})}.$$

Here, f additionally depends on the temperature of the unburnt gas. For different methane concentrations, they get different expressions.

Iijima and Takeno [61] proposed a dependency on pressure, temperature and equivalence ratio:

2. Physical Model

$$f(\tilde{p}/\tilde{p}_{\text{ref}}) = 1 + \beta \ln \frac{\tilde{p}}{\tilde{p}_{\text{ref}}}.$$

Their reference values are $\tilde{T}_{\text{ref}} = 291$ K and $\tilde{p}_{\text{ref}} = 1$ atm. α , β and \tilde{s}_{eff}^0 depend on the type of fuel and the equivalence ratio, i.e. the ratio of fuel to oxidizer concentration divided by the ratio of fuel to oxidizer concentration at stoichiometric conditions.

Metghalchi and Keck [62] assumed a similar expression:

$$f(\tilde{p}/\tilde{p}_{\text{ref}}) = \left(\frac{\tilde{p}}{\tilde{p}_{\text{ref}}} \right)^\beta.$$

The reference state is $\tilde{T}_{\text{ref}} = 298$ K and $\tilde{p}_{\text{ref}} = 1$ atm. Again, α and β are parameters fitted to experimental data, and depend on the equivalence ratio.

Nagy and Verakis [7] used an empirical relation, where the coefficients are fitted to experimental data, including dust explosion experiments:

$$\alpha = 2, \quad f(\tilde{p}/\tilde{p}_{\text{ref}}) = \left(\frac{\tilde{p}}{\tilde{p}_{\text{ref}}} \right)^\beta. \quad (2.7)$$

The parameter β is usually between 0.1 and 0.5.

Choice of Model

Here, we consider the combustion of a premixed, homogeneous fluid inside a closed geometry. Additionally, the flow is assumed to be turbulent, with isentropic and frozen turbulence. This is reasonable since the early stages of an explosion are most important to industrial applications, where the change of turbulence is assumed to be negligible. The effective flame speed depends on the thermodynamic state and local curvature:

$$\tilde{s}_{\text{eff}} = \left(1 - \tilde{\kappa} \tilde{l}_t^{\text{stab.}} \right) \left(\frac{\tilde{T}_u}{\tilde{T}_{\text{ref}}} \right)^2 \left(\frac{\tilde{p}_{\text{ref}}}{\tilde{p}} \right)^\beta \tilde{s}_{\text{eff}}^0. \quad (2.8)$$

\tilde{s}_{eff}^0 is the flame speed of an unperturbed, plane flame front at reference conditions (\tilde{T}_{ref} , \tilde{p}_{ref}). The dependency on temperature of the unburnt gas \tilde{T}_u and pressure \tilde{p} are modelled according to Nagy and Verakis [7].

The parameter $\tilde{l}_t^{\text{stab.}}$ is the turbulent analogon to the laminar Markstein length. In this model, it acts as a stabilisation parameter, to prevent the infinitely thin flame front from wrinkling. It can be interpreted as a turbulent length scale. However, in this work, its value is not determined from asymptotic analysis or experimental data, but chosen such that the flame front remains sufficiently smooth in the simulations.

As outlined before, this stabilisation is necessary because the approximation of the flame front as an infinitely thin sheet neglects mechanisms and features of real combustion processes. The motivation behind this dependency comes from asymptotic analysis, where the Markstein length can be derived for laminar flow, cf. Eq. (2.1). For turbulent combustion, Peters developed a G equation model which is a level-set method for the tracking of

2. Physical Model

the flame front. In his approach, he shows that the averaged turbulent flame front has a burning velocity which depends on the local curvature of the front [36]:

$$\frac{\partial \bar{G}}{\partial t} + \tilde{\mathbf{u}} \cdot \nabla \bar{G} = \tilde{s}_t^0 |\nabla \bar{G}| - \tilde{D}_t \tilde{\kappa} |\nabla \bar{G}|.$$

A bar denotes the average of a quantity, \bar{G} is the averaged level-set function, where the flame front is at $\bar{G}(\tilde{\mathbf{x}}, \tilde{t}) = G_0$, $\tilde{\kappa}$ is the curvature of the averaged flame front and \tilde{D}_t is the turbulent diffusivity.

This work aims at improving already existing, simple one-dimensional models used in the industry. Thus, a very simple model for the flame speed is used. The most straightforward approach is to assume a constant flame speed. However, it has to include some sort of stabilisation mechanism, since the infinitely thin flame front is hydrodynamically unstable. One-dimensional models do not need such a mechanism, since here, the symmetry constraints do not allow for any instability to develop. Eq. (2.8) should be seen as a model for an effective flame speed of a sufficiently smooth flame front. Thus, only the average position of the flame front is known.

2.2. Flow Model

For the flow model, we make the following assumptions: Unburnt and burnt gases are ideal gases. The material parameters are different for the unburnt and burnt fluids, but do not depend on the thermodynamic state. Gravity, heat conduction and friction are neglected and the vessel wall is adiabatic [63]. A similar approach to model confined combustion has been taken by Markstein [56], Matalon [64] and Matalon and Metzener [65]. Rastigejev and Matalon [66, 67] simulated unconfined combustion using the same approximations as here.

The fluid flow in the unburnt and burnt gas is described by the Euler equations. They express the principles of conservation of mass, momentum and energy with non-linear, partial differential equations. For the flow, the flame front is treated as a gasdynamic discontinuity where the physical quantities experience a jump. Thus, additional relations connecting the physical variables before and after the discontinuity are needed, called jump conditions. Additionally, the specification of the kinematics of the flame front, and the boundary and initial conditions complete the formulation of the flow model.

Here, we use the divergence form of the balance equation, also called conservative form. The equation for the conservation of mass relates density changes with the divergence of the flow field [68]:

$$\frac{\partial \tilde{\rho}}{\partial \tilde{t}} + \tilde{\nabla} \cdot (\tilde{\rho} \tilde{\mathbf{u}}) = \tilde{0}. \quad (2.9)$$

The momentum balance connects pressure and flow field:

$$\frac{\partial (\tilde{\rho} \tilde{\mathbf{u}})}{\partial \tilde{t}} + \tilde{\nabla} \cdot (\tilde{\rho} \tilde{\mathbf{u}} \tilde{\mathbf{u}}) = -\tilde{\nabla} \tilde{p}. \quad (2.10)$$

2. Physical Model

The energy balance states that the change of total energy is equal to the work done by pressure forces:

$$\frac{\partial (\tilde{\varrho} (\tilde{e} + \tilde{u}^2/2))}{\partial \tilde{t}} + \tilde{\nabla} \cdot (\tilde{\varrho} (\tilde{e} + \tilde{u}^2/2) \tilde{\mathbf{u}}) = -\tilde{\nabla} \cdot (\tilde{p}\tilde{\mathbf{u}}). \quad (2.11)$$

$\tilde{\varrho}$ is the density, \tilde{t} is the time, $\tilde{\nabla}$ is the Nabla operator, $\tilde{\mathbf{u}}$ is the velocity field, \tilde{p} is the pressure, $\tilde{\mathbf{u}} \cdot \tilde{\mathbf{u}} = \tilde{u}^2$ and \tilde{e} is the specific internal energy, i.e. the internal energy per unit of mass.

A tilde denotes that the quantity has a dimension. The dot between two vector fields denotes the inner product $\mathbf{a} \cdot \mathbf{b} = a_i b_i$, where the subscript ‘ i ’ stands for the three directions in space (Einstein notation). No dot between the product of two vector fields denotes the outer product $\mathbf{a}\mathbf{b} = a_i b_j$.

The ideal gas equation connects pressure, density and temperature:

$$\tilde{p} = \tilde{\varrho} \tilde{R} \tilde{T}, \quad (2.12)$$

where \tilde{R} is the specific gas constant and \tilde{T} is the temperature. The reaction enthalpy $\Delta \tilde{h}_f$ is part of the internal energy of the unburnt gas \tilde{e}_u :

$$\tilde{e}_u = \tilde{c}_{v,u} \tilde{T} + \Delta \tilde{h}_f = \frac{1}{\gamma_u - 1} \frac{\tilde{p}_u}{\tilde{\varrho}_u} + \Delta \tilde{h}_f. \quad (2.13)$$

γ is the ratio of specific heats and \tilde{c}_v is the specific heat at constant volume. \tilde{R} , \tilde{c}_v and γ are in general different in unburnt and burnt gas, denoted by the subscripts ‘ u ’ and ‘ b ’, respectively. Eq. (2.12) and $\tilde{R} = \tilde{c}_v/(\gamma-1)$ have been used for Eq. (2.13). The temperature does not appear in the problem formulation. The internal energy of the burnt gas reads as:

$$\tilde{e}_b = \frac{1}{\gamma_b - 1} \frac{\tilde{p}_b}{\tilde{\varrho}_b}. \quad (2.14)$$

Initially, at $\tilde{t} = \tilde{0}$, the gas is at rest and has a uniform initial temperature and pressure, denoted with the subscript ‘ i ’:

$$\tilde{\mathbf{u}}(\tilde{\mathbf{x}}, \tilde{0}) = \mathbf{0}, \quad \tilde{p}(\tilde{\mathbf{x}}, \tilde{0}) = \tilde{p}_i, \quad \tilde{\varrho}(\tilde{\mathbf{x}}, \tilde{0}) = \tilde{\varrho}_i.$$

At the vessel wall the normal velocity must vanish:

$$\tilde{\mathbf{u}}(\tilde{\mathbf{x}}_v, \tilde{t}) \cdot \mathbf{n}_v = \tilde{0}.$$

$\tilde{\mathbf{x}}_v$ is the location of the vessel wall and \mathbf{n}_v is the unit normal vector of the vessel wall which points outside of the vessel. The gas itself is divided into two phases, unburnt and burnt gas, by the flame front, as shown in Fig. 2.7. The effective flame speed \tilde{s}_{eff} is defined as the relative normal velocity of the smooth flame front with respect to the unburnt gas at the flame front $\tilde{\mathbf{u}}_u$:

2. Physical Model

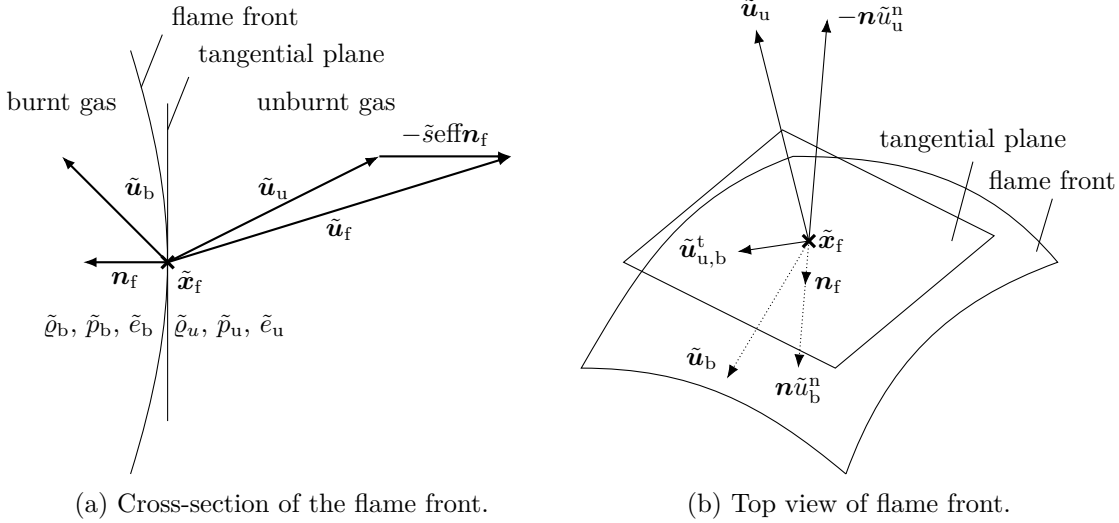


Figure 2.7.: (a) The flame front velocity $\tilde{\mathbf{u}}_f$ has a relative velocity $(-\tilde{s}_{\text{eff}})$ in normal direction \mathbf{n}_f with respect to the velocity of the unburnt gas $\tilde{\mathbf{u}}_u$. (b) The tangential velocity $\tilde{\mathbf{u}}^t$ is continuous across the flame front [69, Fig. 2].

$$\tilde{s}_{\text{eff}} = (\tilde{\mathbf{u}}_f - \tilde{\mathbf{u}}_u) \cdot (-\mathbf{n}_f). \quad (2.15)$$

\mathbf{n}_f is a unit vector normal to the flame front pointing into the burnt gas. The flame front velocity $\tilde{\mathbf{u}}_f$ is the sum of the velocity of the unburnt gas just ahead of the flame front and the burning velocity in normal direction, as shown in Fig. 2.7a:

$$\tilde{\mathbf{u}}_f = \frac{d\tilde{\mathbf{x}}_f}{dt} = \tilde{\mathbf{u}}_u - \tilde{s}_{\text{eff}} \mathbf{n}_f, \quad (2.16)$$

Since velocity, density and pressure are discontinuous at the flame front, jump conditions are required to obtain a physically meaningful solution in the unburnt and burnt gas. Those conditions connect mass, momentum and energy fluxes on both sides of the flame front. To derive the jump conditions, we need the conservation equations in integrated formulation.

Let us assume a control volume $\tilde{V}(\tilde{t})$ which moves with a velocity $\tilde{\mathbf{u}}$. $\partial\tilde{V}$ denotes the surface of the control volume. Then, Reynold's transport theorem states that the total change of an arbitrary quantity \tilde{b} in \tilde{V} is [70]:

$$\frac{d}{dt} \iiint_{\tilde{V}} \tilde{\rho} \tilde{b} d\tilde{V} = \iiint_{\tilde{V}} \frac{\partial(\tilde{\rho} \tilde{b})}{\partial \tilde{t}} d\tilde{V} + \iint_{\partial\tilde{V}} \tilde{\rho} \tilde{b} (\tilde{\mathbf{u}} \cdot \mathbf{n}) d\tilde{O}, \quad (2.17)$$

Here, Gauß' Theorem was used. It states that the integral over the divergence of a vector field $\tilde{\mathbf{b}}$ over a closed volume \tilde{V} is equal to the integral over the vector field over the surface $\partial\tilde{V}$ of the volume, if the vector field is continuously differentiable:

$$\iiint_{\tilde{V}} \tilde{\nabla} \cdot \tilde{\mathbf{b}} d\tilde{V} = \iint_{\partial\tilde{V}} \tilde{\mathbf{b}} \cdot \mathbf{n} d\tilde{O}.$$

2. Physical Model

Applying Reynold's transport theorem and Gauß' theorem to the balance equations, using a control volume which moves with the flame front velocity $\tilde{\mathbf{u}}_f$, yields the balance equations in integral formulation. The conservation of mass, Eq. (2.9), yields:

$$\frac{d}{dt} \iiint_{\tilde{V}} \tilde{\rho} d\tilde{V} + \iint_{\partial\tilde{V}} \tilde{\rho} (\tilde{\mathbf{u}} - \tilde{\mathbf{u}}_f) \cdot \mathbf{n} d\tilde{O} = 0, \quad (2.18)$$

The momentum balance, Eq. (2.10), reads as:

$$\frac{d}{dt} \iiint_{\tilde{V}} \tilde{\rho} \tilde{\mathbf{u}} d\tilde{V} + \iint_{\partial\tilde{V}} \tilde{\rho} \tilde{\mathbf{u}} (\tilde{\mathbf{u}} - \tilde{\mathbf{u}}_f) \cdot \mathbf{n} d\tilde{O} = - \iint_{\partial\tilde{V}} \tilde{p} \mathbf{n} d\tilde{O}, \quad (2.19)$$

The energy balance, Eq. (2.11), is:

$$\frac{d}{dt} \iiint_{\tilde{V}} \tilde{\rho} (\tilde{e} + \tilde{u}^2/2) d\tilde{V} + \iint_{\partial\tilde{V}} \tilde{\rho} (\tilde{e} + \tilde{u}^2/2) (\tilde{\mathbf{u}} - \tilde{\mathbf{u}}_f) \cdot \mathbf{n} d\tilde{O} = - \iint_{\partial\tilde{V}} \tilde{p} \tilde{\mathbf{u}} \cdot \mathbf{n} d\tilde{O}. \quad (2.20)$$

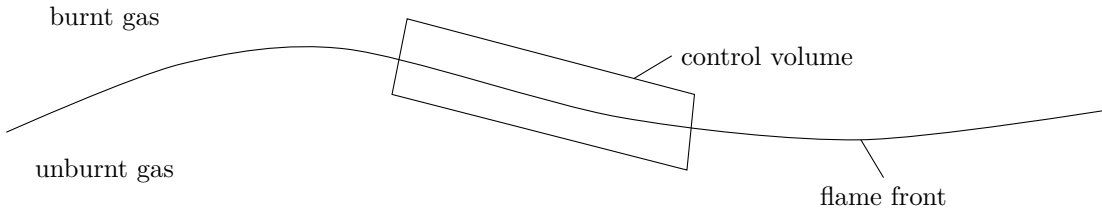


Figure 2.8.: A control volume which encloses the flame front. It is moving with the velocity of the flame front.

The jump conditions are obtained by choosing a volume which encloses parts of the flame front, as shown in Fig. 2.8. When the control volume becomes infinitely thin, i.e. it approaches the flame front, all volume integrals vanish in Eqs. (2.18), (2.19) and (2.20), since they are much smaller than the surface integrals. Thus, the jump of the mass flux reads as, cf. Eq. (2.18):

$$\tilde{\rho}_u (\tilde{\mathbf{u}}_u - \tilde{\mathbf{u}}_f) \cdot \mathbf{n}_f = \tilde{\rho}_b (\tilde{\mathbf{u}}_b - \tilde{\mathbf{u}}_f) \cdot \mathbf{n}_f. \quad (2.21)$$

The jump of momentum flux and pressure is obtained from Eq. (2.19):

$$(\tilde{\rho}_u \tilde{\mathbf{u}}_u (\tilde{\mathbf{u}}_u - \tilde{\mathbf{u}}_f) + \tilde{p}_u \mathbf{I}) \cdot \mathbf{n}_f = (\tilde{\rho}_b \tilde{\mathbf{u}}_b (\tilde{\mathbf{u}}_b - \tilde{\mathbf{u}}_f) + \tilde{p}_b \mathbf{I}) \cdot \mathbf{n}_f, \quad (2.22)$$

and the jump of the energy flux and work done by pressure is obtained from Eq. (2.20):

$$(\tilde{\rho}_u (\tilde{\mathbf{u}}_u - \tilde{\mathbf{u}}_f) (\tilde{e}_u + \tilde{u}_u^2/2) + \tilde{p}_u \tilde{\mathbf{u}}_u) \cdot \mathbf{n}_f = (\tilde{\rho}_b (\tilde{\mathbf{u}}_b - \tilde{\mathbf{u}}_f) (\tilde{e}_b + \tilde{u}_b^2/2) + \tilde{p}_b \tilde{\mathbf{u}}_b) \cdot \mathbf{n}_f. \quad (2.23)$$

2. Physical Model

With the help of Eq. (2.15), the jump conditions are simplified. The superscript ‘n’ denotes the component of a vector normal to the flame front. The mass balance across the flame front reads as:

$$\tilde{\varrho}_u \tilde{s}_{\text{eff}} = \tilde{\varrho}_b (\tilde{u}_f^n - \tilde{u}_b^n). \quad (2.24)$$

For the momentum flux and jump of pressure, we get:

$$\tilde{\varrho}_u \tilde{s}_{\text{eff}} \tilde{\mathbf{u}}_u + \tilde{p}_u \mathbf{n}_f = \tilde{\varrho}_u \tilde{s}_{\text{eff}} \tilde{\mathbf{u}}_b + \tilde{p}_b \mathbf{n}_f, \quad (2.25)$$

and for the energy flux:

$$\tilde{\varrho}_u \tilde{s}_{\text{eff}} \left(\tilde{e}_u + \tilde{u}_u^2/2 \right) + \tilde{p}_u \tilde{u}_u^n = \tilde{\varrho}_u \tilde{s}_{\text{eff}} \left(\tilde{e}_b + \tilde{u}_b^2/2 \right) + \tilde{p}_b \tilde{u}_b^n. \quad (2.26)$$

Eq. (2.25) can be split into a normal part:

$$\tilde{\varrho}_u \tilde{s}_{\text{eff}} \tilde{u}_u^n + \tilde{p}_u = \tilde{\varrho}_u \tilde{s}_{\text{eff}} \tilde{u}_b^n + \tilde{p}_b, \quad (2.27a)$$

and a tangential part:

$$\tilde{\mathbf{u}}_u^t = \tilde{\mathbf{u}}_b^t. \quad (2.27b)$$

The superscript ‘t’ denotes the component of a vector at the flame front in tangential direction.

2.3. Non-dimensional Formulation

A non-dimensional formulation is obtained by scaling all physical quantities with characteristic values. To get the non-dimensional density ϱ and pressure p , the initial density $\tilde{\varrho}_i$ and the initial pressure \tilde{p}_i are used:

$$\tilde{\varrho} = \tilde{\varrho}_i \varrho, \quad \tilde{p} = \tilde{p}_i p. \quad (2.28)$$

The velocity is scaled with \tilde{s}_{eff}^0 , and the characteristic length scale is the reference length of the vessel \tilde{L}_{ref} :

$$\tilde{\mathbf{u}} = \tilde{s}_{\text{eff}}^0 \mathbf{u}, \quad \tilde{\mathbf{x}} = \tilde{L}_{\text{ref}} \mathbf{x}. \quad (2.29)$$

In this problem, the time scale is chosen as the ratio of the characteristic length divided by the characteristic velocity, $\tilde{L}_{\text{ref}}/\tilde{s}_{\text{eff}}^0$. The specific internal energy and reaction enthalpy are scaled with the initial pressure divided by the initial density $\tilde{p}_i/\tilde{\varrho}_i$:

$$\tilde{t} = (\tilde{L}_{\text{ref}}/\tilde{s}_{\text{eff}}^0) t, \quad \tilde{e} = (\tilde{p}_i/\tilde{\varrho}_i) e, \quad \Delta \tilde{h}_f = (\tilde{p}_i/\tilde{\varrho}_i) \Delta h_f. \quad (2.30)$$

2. Physical Model

The non-dimensional formulation of the problem is obtained by inserting the scaled quantities, Eqs. (2.28) to (2.30), into all governing equations. When using this scaling approach, five non-dimensional numbers can be identified. For the definition of one of those numbers, the speed of sound \tilde{c}_i at reference conditions is needed:

$$\tilde{c}_i^2 := \left(\frac{\partial \tilde{p}}{\partial \tilde{\varrho}} \right)_{s=\text{const},i} = \frac{\gamma_u \tilde{p}_i}{\tilde{\varrho}_i}.$$

\tilde{c}_i is used to define a reference Mach number M_{ref} :

$$M_{\text{ref}} = \frac{\tilde{s}_{\text{eff}}^0}{\tilde{c}_i}.$$

The first non-dimensional number is proportional to the squared reference Mach number and it appears in the non-dimensional momentum and energy balances:

$$\varepsilon = \frac{M_{\text{ref}}^2}{\gamma_u}. \quad (2.31)$$

The second non-dimensional number is the (turbulent) stabilisation number S_t , defined as the ratio of the (turbulent) stabilisation length $\tilde{l}_t^{\text{stab.}}$ divided by the characteristic length \tilde{L}_{ref} . It appears in the non-dimensional burning velocity:

$$S_t = \frac{\tilde{l}_t^{\text{stab.}}}{\tilde{L}_{\text{ref}}}. \quad (2.32)$$

The third non-dimensional quantity is the non-dimensional reaction enthalpy Δh_f . It influences the ratio of initial pressure and end pressure and it appears in the jump condition for the internal energy. The fourth and fifth non-dimensional numbers are the ratio of specific heats of unburnt, γ_u , and burnt gas, γ_b .

The scaling is not unique. For example, one could have chosen $\Delta \tilde{h}_f$ as a characteristic enthalpy, and used it for scaling the internal energy. Then, the non-dimensional numbers which appear would be different.

The non-dimensional mass balance is obtained by scaling Eq. (2.9):

$$\frac{\partial \varrho}{\partial t} + \nabla \cdot (\varrho \mathbf{u}) = 0. \quad (2.33)$$

Scaling Eq. (2.10) yields the non-dimensional momentum balance:

$$\varepsilon \left(\frac{\partial (\varrho \mathbf{u})}{\partial t} + \nabla \cdot (\varrho \mathbf{u} \mathbf{u}) \right) = -\nabla p. \quad (2.34)$$

The non-dimensional energy balance reads as, cf. Eq. (2.11):

$$\frac{\partial (\varrho (e + \varepsilon u^2/2))}{\partial t} + \nabla \cdot (\varrho \mathbf{u} (e + \varepsilon u^2/2)) = -\nabla \cdot (p \mathbf{u}). \quad (2.35)$$

2. Physical Model

For the caloric equation of state, scaling Eq. (2.13) yields the internal energy of the unburnt gas:

$$e_u = \frac{1}{\gamma_u - 1} \frac{p_u}{\varrho_u} + \Delta h_f. \quad (2.36)$$

For the burnt gas, the non-dimensional caloric equation of state is obtained by scaling Eq. (2.14):

$$e_b = \frac{1}{\gamma_b - 1} \frac{p_b}{\varrho_b}. \quad (2.37)$$

The scaled initial and boundary conditions simplify to:

$$\varrho(\mathbf{x}, 0) = p(\mathbf{x}, 0) = 1, \quad \mathbf{u}(\mathbf{x}, 0) = \mathbf{0}, \quad u^n(\mathbf{x}_v, t) = 0.$$

Scaling Eq. (2.8) yields:

$$s_{\text{eff}} = (1 - \kappa S_t) (p_u / \varrho_u)^2 / p^\beta. \quad (2.38)$$

Thus, the velocity of the flame front \mathbf{u}_f is:

$$\mathbf{u}_f = \frac{d\mathbf{x}_f}{dt} = \mathbf{u}_u - s_{\text{eff}} \mathbf{n}_f. \quad (2.39)$$

Inserting the scaling quantities into Eqs. (2.24), (2.26) (2.27a) and (2.27b) yields the jump conditions in non-dimensional form. For the jump of the mass flux, we get:

$$\varrho_u s_{\text{eff}} = \varrho_b (u_f^n - u_b^n). \quad (2.40)$$

The jump of normal momentum and pressure reads as:

$$\varepsilon s_{\text{eff}} \varrho_u u_u^n + p_u = \varepsilon s_{\text{eff}} \varrho_b u_b^n + p_b. \quad (2.41a)$$

The tangential component of the jump of momentum flux is:

$$\mathbf{u}_u^t = \mathbf{u}_b^t. \quad (2.41b)$$

For the jump of energy flux and work done by pressure, we obtain:

$$\varrho_u s_{\text{eff}} \left(e_u + \varepsilon u_u^2 / 2 \right) + p_u u_u^n = \varrho_b s_{\text{eff}} \left(e_b + \varepsilon u_b^2 / 2 \right) + p_b u_b^n. \quad (2.42)$$

2. Physical Model

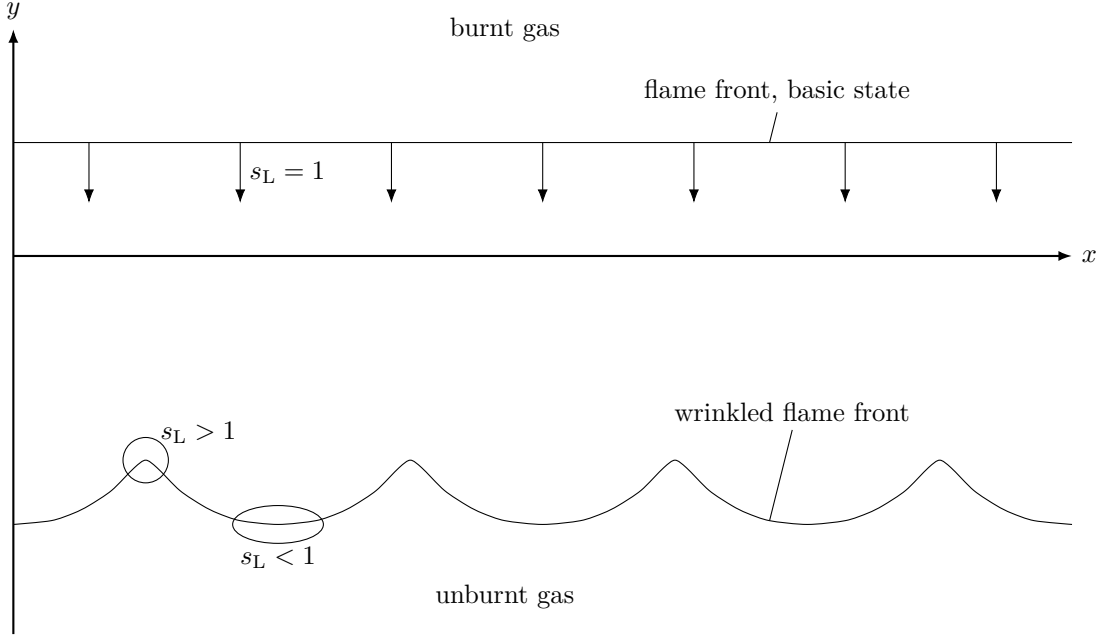


Figure 2.9.: Schematic drawing of the base state of the unconfined, two-dimensional combustion (top) and a wrinkled flame front (bottom), moving into quiescent, unburnt gas. The Markstein mechanism works as follows [45]: Regions where the flame front points towards the burnt gas, $\kappa < 0$, have an amplified burning velocity (marked with a circle), and vice versa (marked with an ellipse).

2.4. Stability of the Flame Front

When treating the flame front as a gasdynamic discontinuity, intrinsic instabilities are observed [35]. The stability analysis presented here is valid for unconfined combustion, i.e. the velocity field is (almost) divergence-free. For stability, the viscosity plays a secondary role [66]. Also, a laminar combustion is assumed.

The mass balance, Eq. (2.33), reduces to the condition of zero divergence of the flow field:

$$\nabla \cdot \mathbf{u} = 0. \quad (2.43)$$

The base flow is a parallel velocity profile with a plane flame front, as shown in Fig. 2.9 on the top. The undisturbed flame front, located at $y = -t$, moves into quiescent gas with a velocity of $v = -1$ (base state). Thus, the velocity in x direction vanishes, $u = 0$, and in y direction, it is a piece-wise constant function:

$$v = \begin{cases} 0 & y < -t, \\ \sigma - 1 & y > -t. \end{cases} \quad (2.44)$$

The density is a piece-wise constant function, and $\sigma = \rho_u/\rho_b$ is the density ratio of the unburnt and burnt gas. Here, it is constant [66, 51]:

2. Physical Model

$$\varrho = \begin{cases} 1 & \text{in the unburnt gas,} \\ \sigma^{-1} & \text{in the burnt gas.} \end{cases} \quad (2.45)$$

Since temperature and pressure in the unburnt gas are constant, the laminar burning velocity reads as:

$$s_L = 1 - \kappa \text{Ma}. \quad (2.46)$$

Here, the Markstein number $\text{Ma} = \tilde{l}_{\text{Ma}}/\tilde{l}_{\text{ref}}$ is used, since we are dealing with laminar combustion. For the pressure, the following is obtained:

$$p = \begin{cases} 1 & y < -t, \\ 1 - \varepsilon(\sigma - 1) & y > -t. \end{cases} \quad (2.47)$$

The jump of pressure is usually very low, since $\varepsilon \ll 1$ for slow combustion. Since the laminar burning velocity s_L depends on the curvature, high frequency instabilities are damped. In the analysis by Markstein, the linearised Euler equations combined with the linearised interface conditions, Eqs. (2.44), (2.45) and (2.47), were solved in the limit of $\varepsilon \rightarrow 0$. This analysis yields a relation for the growth rate α of a disturbance with the wave number k [56, 66]:

$$(\sigma + 1)\alpha^2 + 2(1 + \text{Ma}k)\sigma k\alpha - (\sigma^{-1} - 1 - 2\text{Ma}\sigma k)\sigma k^2 = 0. \quad (2.48)$$

When the growth rate is positive, the corresponding perturbation mode is unstable. The critical wave number k_c is obtained by setting $\alpha = 0$:

$$k_c = \frac{1}{2} \frac{\sigma - 1}{\sigma} \frac{1}{\text{Ma}}. \quad (2.49)$$

All perturbations with $k > k_c$ have a negative growth rate, i.e. they are damped. Vice versa, distortions with a wave number $k < k_c$ have a positive growth rate, which means that they are unstable. Thus, the Markstein model exhibits a high wave number cut-off. For $\text{Ma} \rightarrow 0$, the critical wavenumber becomes infinitely large, $k_c \rightarrow \infty$. This implies that s_L is constant, corresponding to the Darreius-Landau model, and perturbations of all wave numbers are unstable.

This concept is also valid for the stability of the averaged, infinitely thin, turbulent flame front, when the burning velocity depends on the local curvature of the (averaged) front. Thus, the result of this stability analysis, Eq. (2.49), is used to verify the flame front tracking algorithm in Chapter 6.

3. Expansion for Small Mach Numbers

Typical flame speeds for gas combustion are below 1 m/s [71, 24, 72]. For dust, they are a little higher, between 1 m/s to 5 m/s for organic dust, and between 10 m/s to 20 m/s for aluminium dust [73]. Note, that for dust explosions, turbulence plays an important role [8], thus, the burning velocities are higher [74]. Since the speed of sound in air at normal conditions is about 300 m/s, an expansion of the governing equations under the assumption of small squared reference Mach numbers, i.e. $\varepsilon \ll 1$, is justified. Expanding an arbitrary quantity b yields:

$$b(\mathbf{x}, t) = b_0(\mathbf{x}, t) + \varepsilon b_1(\mathbf{x}, t) + \dots \quad (3.1)$$

b_0 is the leading-order quantity, and ϱ_1 is the second-order quantity. All other higher order terms do not appear in the formulation.

We show that only the leading-order quantities – with the exception of the pressure – are necessary to obtain a closed problem formulation. Amongst others, the small Mach number approximation has been applied by Markstein [56], Buckmaster [75], Matalon [64] and Law [5]. It allows a simplification of the governing equations. However, with this approach, the transition from slow deflagrations to detonations cannot be described, since it is a supersonic process involving shock waves [76].

3.1. Governing Equations

Expansion of the governing equations is done by expanding all quantities with respect to ε , cf. Eq. (3.1). Then, terms with equal powers of ε are collected. For the leading order equations, this can also be done by formally setting $\varepsilon = 0$. Thus, the leading-order conservation of mass is obtained from Eq. (2.33):

$$\frac{\partial \varrho_0}{\partial t} + \nabla \cdot (\varrho_0 \mathbf{u}_0) = 0. \quad (3.2)$$

Expanding Eq. (2.34) yields:

$$\nabla p_0 = \mathbf{0}. \quad (3.3)$$

The energy balance of leading-order, expanding Eq. (2.35), reads as:

$$\frac{\partial(\varrho_0 e_0)}{\partial t} + \nabla \cdot (\varrho_0 \mathbf{u}_0 e_0) = -\nabla \cdot (p_0 \mathbf{u}_0). \quad (3.4)$$

3. Expansion for Small Mach Numbers

In Eqs. (3.2), (3.3) and (3.4), the velocity appears only in divergence form $\nabla \cdot \mathbf{u}$. This implies that the flow field has to be calculated by the second-order momentum balance:

$$\frac{\partial(\varrho_0 \mathbf{u}_0)}{\partial t} + \nabla \cdot (\varrho_0 \mathbf{u}_0 \mathbf{u}_0) = -\nabla p_1. \quad (3.5)$$

Dividing Eq. (3.5) by the density, taking the curl and applying basic vector calculus identities yields a transport equation for the vorticity $\boldsymbol{\omega}_0 = \nabla \times \mathbf{u}_0$:

$$\frac{\partial(\varrho_0 \boldsymbol{\omega}_0)}{\partial t} + \nabla \cdot (\varrho_0 \mathbf{u}_0 \boldsymbol{\omega}_0) = \varrho_0 (\boldsymbol{\omega}_0 \cdot \nabla \mathbf{u}_0 - \boldsymbol{\omega}_0 \nabla \cdot \mathbf{u}_0) + \frac{1}{\varrho_0} \nabla \varrho_0 \times \nabla p_1. \quad (3.6)$$

For the caloric equation of state of the unburnt gas, Eq. (2.36), we get:

$$e_{u,0} = \frac{1}{\gamma_u - 1} \frac{p_{u,0}}{\varrho_{u,0}} + \Delta h_f. \quad (3.7)$$

For the burnt gas, the leading-order internal energy is obtained from Eq. (2.36):

$$e_{b,0} = \frac{1}{\gamma_b - 1} \frac{p_{b,0}}{\varrho_{b,0}}. \quad (3.8)$$

Expanding the initial and boundary conditions yields:

$$\varrho_0(\mathbf{x}, 0) = p_0(\mathbf{x}, 0) = 1, \quad \mathbf{u}_0(\mathbf{x}, 0) = \mathbf{0}, \quad u_0^n(\mathbf{x}_v, t) = 0.$$

Expanding the jump condition for mass, Eq. (2.40) yields:

$$\varrho_{u,0} s_{\text{eff}} = \varrho_{b,0} (u_{f,0}^n - u_{b,0}^n). \quad (3.9)$$

For the jump of normal momentum and pressure, we expand Eq. (2.41a):

$$p_{u,0} = p_{b,0}, \quad (3.10a)$$

and for the tangential part, Eq. (2.41b) expands to:

$$\mathbf{u}_{u,0}^t = \mathbf{u}_{b,0}^t. \quad (3.10b)$$

For the jump of energy flux and work done by the pressure, expansion of Eq. (2.42) yields:

$$\varrho_{u,0} s_{\text{eff}} e_{u,0} + p_{u,0} u_{u,0}^n = \varrho_{u,0} s_{\text{eff}} e_{b,0} + p_{b,0} u_{b,0}^n. \quad (3.11)$$

3.2. Leading-order Formulation

Eq. (3.3) shows that there is no leading-order pressure gradient in the unburnt and burnt gas, and Eq. (3.10a) implies that there is no pressure jump across the flame front. Thus, the leading-order pressure is time-dependent only. Using $p_0 = P$ and $p_1 = p'$ yields:

$$p(\mathbf{x}, t) \sim P(t) + \varepsilon p'(\mathbf{x}, t), \quad (3.12)$$

with a time-dependent only leading-order pressure $P(t)$ which is used in thermodynamic calculations and a second-order pressure correction $p'(\mathbf{x}, t)$ which depends on time and location. A similar conclusion has been drawn by Emmons in 1958. In his analytical treatment of the combustion process in an unconfined geometry, the author says that ‘for many purposes the process [combustion] may be considered one of constant pressure’. Furthermore, he states that it ‘is not permissible, however, to assume that the whole flow process [...] is a constant pressure process’ [77, pp. 601–602]. When doing a small Mach number expansion, the pressure is time-dependent only up to leading order. However, the small pressure fluctuations cannot be neglected. Thus, the second-order pressure has to be included in the problem description.

In the following, all other quantities are of leading-order, and we drop the subscript ‘0’:

$$\varrho_0 \rightarrow \varrho, \quad \mathbf{u}_0 \rightarrow \mathbf{u}, \quad \boldsymbol{\omega}_0 \rightarrow \boldsymbol{\omega}, \quad e_0 \rightarrow e.$$

With the material derivative, i.e. the change of a quantity along a streamline,

$$\frac{D(*)}{Dt} = \frac{\partial(*)}{\partial t} + \mathbf{u} \cdot \nabla(*),$$

the divergence of the velocity field is obtained from Eq. (3.2):

$$\nabla \cdot \mathbf{u} = -\frac{1}{\varrho} \frac{D\varrho}{Dt}, \quad (3.13)$$

and the second-order momentum balance, Eq. (3.5), is equal to:

$$\nabla p' = -\frac{1}{\varrho} \frac{D\mathbf{u}}{Dt}. \quad (3.14)$$

Using the definition of the enthalpy $h = e + p/\varrho$ and the material derivative, Eq. (3.4) reads as:

$$\varrho \frac{Dh}{Dt} = \frac{dP}{dt}, \quad (3.15)$$

which reduces to the isentropic change of state equation, valid everywhere in the flow field except at the flame front:

$$\frac{1}{\varrho} \frac{D\varrho}{Dt} = \frac{1}{\gamma} \frac{1}{P} \frac{dP}{dt}. \quad (3.16)$$

3. Expansion for Small Mach Numbers

This implies that the entropy remains constant for each material element, except when crossing the flame front. A material element is an infinitely small fluid volume which moves with the flow. Eq. (3.16) is not valid at the flame front. The entropy s is:

$$s = \ln \frac{P}{\rho^\gamma}, \quad \text{or} \quad \exp s = \frac{P}{\rho^\gamma}. \quad (3.17)$$

In the unburnt gas, $s_u \equiv 0$ and in the burnt gas, the entropy increases, $s_b > 0$. The divergence of the velocity field in the unburnt and burnt gas is time-dependent only, as seen when putting Eq. (3.16) into Eq. (3.13):

$$\nabla \cdot \mathbf{u} = -\frac{1}{\rho} \frac{D\rho}{Dt} = -\frac{1}{\gamma} \frac{1}{P} \frac{dP}{dt}. \quad (3.18)$$

Since the initial density $\rho_i = 1$ and the entropy are uniform, the flow is isentropic and the leading-order pressure P is time-dependent only, the density in the unburnt gas remains uniform:

$$\rho_u(t) = P^{1/\gamma_u}. \quad (3.19)$$

Combining Eqs. (3.6) and (3.14) yields:

$$\frac{D\boldsymbol{\omega}}{Dt} = \boldsymbol{\omega} \cdot \nabla \mathbf{u} - \boldsymbol{\omega} \nabla \cdot \mathbf{u} + \frac{1}{\rho} \frac{D\mathbf{u}}{Dt} \times \nabla \rho. \quad (3.20)$$

Combining Eqs. (3.9), (3.11) and (3.19) and using the fact that P depends only on time yields the density ratio:

$$\sigma = \frac{\rho_u}{\rho_b} = \frac{\gamma_b - 1}{\gamma_b} \left(\frac{\gamma_u}{\gamma_u - 1} + \Delta h_f P^{(1-\gamma_u)/\gamma_u} \right). \quad (3.21)$$

Since the right-hand side of Eq. (3.21) is a function of time only, the density in the burnt gas just behind the flame front is also uniform. For the jump of normal velocity, we use Eqs. (3.9) and (3.21) and get:

$$u_u^n - u_b^n = (\sigma - 1) s_{\text{eff}} = \frac{\gamma_b - 1}{\gamma_b} \left(\frac{\gamma_b - \gamma_u}{(\gamma_u - 1)(\gamma_b - 1)} + \Delta h_f P^{(1-\gamma_u)/\gamma_u} \right) s_{\text{eff}}, \quad (3.22)$$

and the entropy s_b at the flame front reads as:

$$\exp s_b = \sigma^{1/\gamma_b}. \quad (3.23)$$

The effective burning velocity s_{eff} can be zero when the curvature is large enough, $\kappa = 1/S_t$. However, it can never be below zero, since this would imply a ‘reverse’ combustion, i.e. burnt gas is transformed to unburnt gas, which would contradict the 2nd law of thermodynamics. The special case $s_{\text{eff}} = 0$ means that locally there is no combustion and the flame front is just passively transported with the flow. Using the isentropic relations for an ideal

3. Expansion for Small Mach Numbers

gas, the dependence of s_{eff} on the temperature can be expressed with the leading-order pressure:

$$s_{\text{eff}} = (1 - \kappa S_t) P^{2(\gamma_u - 1)/\gamma_u - \beta}. \quad (3.24)$$

For confined combustion, the lowest density, corresponding to the highest entropy and highest temperature, is at the location of the initial explosion. Considering the first material element which combusts (at the initial pressure $P_1 = 1$), the ratio of the density and the entropy have a maximum for all non-trivial cases, i.e. $\Delta h_f > 0$:

$$\max \sigma = \frac{\gamma_b - 1}{\gamma_b} \left(\frac{\gamma_u}{\gamma_u - 1} + \Delta h_f \right). \quad (3.25)$$

Thus, the density of the burnt gas has a minimum and the temperature has a maximum at the initial explosion location. The rise in temperature due to burning and the adiabatic compression after combustion are non-linear effects. Thus, there is a substantial temperature gradient, also called Flamm-Mache gradient [25, 55, 8], in the burnt gas, especially in later stages of the process. This can lead to very high temperatures at the location of the initial explosion and re-illumination, as observed in experiments [55].

Pressure Rise

Integration of the divergence of the velocity over the volume of the vessel V_v yields an equation for the rise of the pressure. With Eq. (3.18), we get:

$$\iiint_{V_v} \nabla \cdot \mathbf{u} \, dV = \iiint_{\text{unburnt}} \nabla \cdot \mathbf{u} \, dV + \iiint_{\text{burnt}} \nabla \cdot \mathbf{u} \, dV = - \left(\frac{V_u}{\gamma_u} + \frac{V_b}{\gamma_b} \right) \frac{1}{P} \frac{dP}{dt}. \quad (3.26)$$

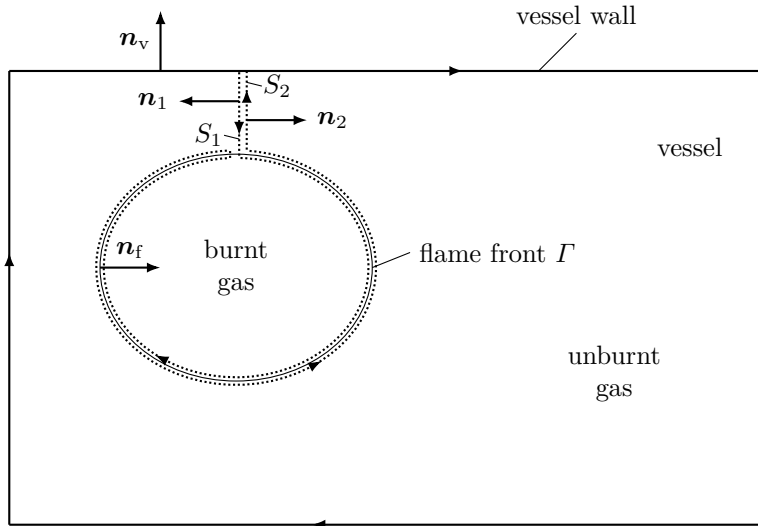


Figure 3.1.: Integration path to obtain an expression for the change of pressure.

3. Expansion for Small Mach Numbers

Since the velocity \mathbf{u} is not continuously differentiable at the flame front, we have to exclude the flame front from the integration path which is shown in Fig. 3.1. Using Gauß' theorem, we write:

$$\begin{aligned} \iiint_{V_v} \nabla \cdot \mathbf{u} \, dV = & \oint_{\text{vessel wall}} \mathbf{u} \cdot \mathbf{n}_v \, dO + \iint_{S_1} \mathbf{u} \cdot \mathbf{n}_1 \, dO \\ & + \oint_{I_b} \mathbf{u} \cdot \mathbf{n}_f \, dO - \oint_{I_u} \mathbf{u} \cdot \mathbf{n}_f \, dO + \iint_{S_2} \mathbf{u} \cdot \mathbf{n}_2 \, dO. \end{aligned} \quad (3.27)$$

I is the flame front surface and S_1 and S_2 are curves from the vessel wall to the flame front which coincide.

The first integral on the right-hand side is zero due to the boundary condition at the vessel wall, and the second and last term cancel each other out due to $\mathbf{n}_1 = -\mathbf{n}_2$ and $S_1 = S_2$. Thus, we get:

$$\iiint_{V_v} \nabla \cdot \mathbf{u} \, dV = \oint_{\text{f.f.}} (u_b^n - u_u^n) \, dO, \quad (3.28)$$

where f.f. stands for flame front. Combining Eqs. (3.26) and (3.28) yields an ordinary, non-linear differential equation for the pressure:

$$\left(\frac{V_u}{\gamma_u} + \frac{V_b}{\gamma_b} \right) \frac{1}{P} \frac{dP}{dt} = \oint_{\text{f.f.}} (u_u^n - u_b^n) \, dO = (\sigma - 1) \oint_{\text{f.f.}} s_{\text{eff}} \, dO > 0. \quad (3.29)$$

Since $\sigma > 1$ and $s_{\text{eff}} > 0$, the pressure rise is always positive.

3.3. Decomposition of the Velocity Field

We decompose the velocity field in an irrotational $\nabla\varphi$ and a divergence-free part $\nabla \times \boldsymbol{\psi}$. This allows us to find the solution to two easier sub-problems [78]:

$$\mathbf{u} = \nabla\varphi + \nabla \times \boldsymbol{\psi}. \quad (3.30)$$

Taking the divergence of Eq. (3.30), we get:

$$\nabla \cdot \mathbf{u} = \nabla \cdot \nabla\varphi + \underbrace{\nabla \cdot \nabla \times \boldsymbol{\psi}}_{=0} = \nabla^2\varphi, \quad (3.31)$$

and using Eq. (3.18), we get:

$$\nabla^2\varphi = -\frac{1}{\gamma} \frac{1}{P} \frac{dP}{dt}. \quad (3.32)$$

Taking the curl of Eq. (3.30), we get:

3. Expansion for Small Mach Numbers

$$\nabla \times \mathbf{u} = \boldsymbol{\omega} = \underbrace{\nabla \times \nabla \varphi}_{=0} + \nabla \times \nabla \times \boldsymbol{\psi} = -\nabla^2 \boldsymbol{\psi} + \nabla (\nabla \cdot \boldsymbol{\psi}). \quad (3.33)$$

Without loss of generality, we set $\nabla \cdot \boldsymbol{\psi} = 0$ and get:

$$\nabla^2 \boldsymbol{\psi} = -\boldsymbol{\omega}, \quad (3.34)$$

where the vorticity $\boldsymbol{\omega}$ is obtained by solving Eq. (3.20). The density gradient can be expressed with the gradient of the entropy, Eq. (3.17):

$$\frac{1}{\rho} \nabla \rho = -\frac{1}{\gamma} \nabla s. \quad (3.35)$$

Putting Eqs. (3.18) and (3.35) into Eq. (3.20) yields:

$$\frac{D\boldsymbol{\omega}}{Dt} = \boldsymbol{\omega} \cdot \nabla \mathbf{u} + \frac{1}{\gamma} \frac{1}{P} \frac{dP}{dt} \boldsymbol{\omega} + \frac{1}{\gamma} \nabla s \times \frac{D\mathbf{u}}{Dt}. \quad (3.36)$$

Initially, the unburnt gas is at rest, implying a vanishing vorticity. Since friction is neglected and the fluid is barotropic, i.e. the density is only a function of the pressure, the velocity in the unburnt gas is irrotational for all times [79]. In the burnt gas, we cannot conclude that there is no vorticity a priori, since in general, the flame front produces vorticity [80, 81, 82]. Additionally, the gradient of the pressure correction, i.e. the material derivative of the velocity, and the gradient of the entropy function are not necessarily parallel. This results in a non-zero source term on the right side of Eq. (3.36). Thus, the vorticity transport equation has to be solved only in the burnt gas and $\gamma = \gamma_b$ in Eq. (3.36).

We only consider two-dimensional or three-dimensional, rotational symmetric geometries. Thus, the vorticity has just one component in the z or ϑ direction, respectively. In two dimensions, $\boldsymbol{\omega} = \omega^{2D} \mathbf{e}_z$. Additionally, the first term on the right-hand side of Eq. (3.36) is equal to zero, since \mathbf{e}_z and $\nabla \mathbf{u}$ are perpendicular and the cross product has only a non-zero component in z direction:

$$\frac{D\omega^{2D}}{Dt} = \frac{1}{\gamma_b} \frac{1}{P} \frac{dP}{dt} \omega^{2D} + \frac{1}{\gamma_b} \left(\nabla s \times \frac{D\mathbf{u}}{Dt} \right) \cdot \mathbf{e}_z. \quad (3.37)$$

For three-dimensional, rotational symmetric geometries, $\boldsymbol{\omega} = \omega^{3D} \mathbf{e}_\vartheta$ and the velocity gradient in direction of the vorticity is u_r/r [68, Eq. (W) of Table A.7-2, p. 835], where u_r is the velocity component in radial direction. The cross product has only a component in ϑ direction:

$$\frac{D\omega^{3D}}{Dt} = \left(\frac{u_r}{r} + \frac{1}{\gamma_b} \frac{1}{P} \frac{dP}{dt} \right) \omega^{3D} + \frac{1}{\gamma_b} \left(\nabla s \times \frac{D\mathbf{u}}{Dt} \right) \cdot \mathbf{e}_\vartheta. \quad (3.38)$$

3.4. Jump of the Vorticity

With the decomposition of the velocity, we decoupled the divergence and the curl of the velocity field. Therefore, we need an additional jump condition for the vorticity. Matalon et. al. [82] considered the vorticity distribution inside the flame zone, and also got an expression for the jump of vorticity. However, they assume unconfined combustion with zero-divergence flow. Hayes [83] derived an expression for the jump of the tangential vorticity for a gasdynamic discontinuity in unsteady, compressible flow. It states that the vorticity tangential to the discontinuity experiences a jump:

$$[\boldsymbol{\omega}] = \mathbf{n} \times \left(\nabla^t (\rho u_r) [1/\rho] - \frac{1}{\rho u_r} \left(\frac{D^t \mathbf{u}^t}{Dt} + u_s \frac{D^t \mathbf{n}}{Dt} \right) [\rho] \right). \quad (3.39)$$

$[(*)] = (*)_b - (*)_u$ denotes the jump of a quantity, $\nabla^t(*)$ denotes the gradient in tangential direction along the flame front and $D^t(*)/Dt$ denotes the tangential part of the material derivative of a point on the flame front which moves with the tangential velocity of the flow. u_r and u_s are the relative and absolute normal velocity of the discontinuity, respectively. Here, $u_r = s_{\text{eff}}$ and $u_s = u_u^n + s_{\text{eff}}$.

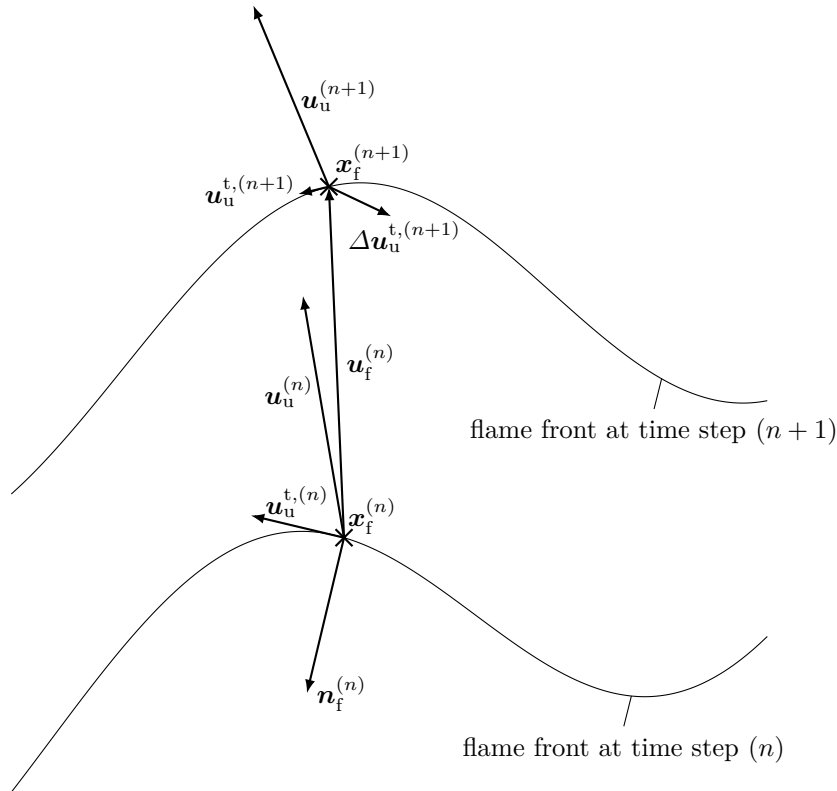


Figure 3.2.: Difference of the tangential velocity of the unburnt gas at the flame front between two time steps. Here, $\Delta t = 1$. For realistic values of the time step, $\Delta t \ll 1$, the position of the flame front on the top would be much closer to the one on the bottom.

$D^t \mathbf{u}_u^t / Dt$ is the change of the tangential velocity \mathbf{u}_u^t when moving with the flame front velocity \mathbf{u}_f in tangential direction, as shown in Fig. 3.2:

3. Expansion for Small Mach Numbers

$$\frac{D^t \mathbf{u}_u^t}{Dt} = \left(\lim_{\Delta t \rightarrow 0} \frac{(\Delta \mathbf{u}_u^t) \cdot \mathbf{e}^t}{\Delta t} \right) \mathbf{e}^t,$$

and the same is defined for the normal vector \mathbf{n}_f .

Using Eq. (2.38) and since the density in the unburnt gas is uniform, the tangential gradient of the mass flux through the flame front reads as:

$$\nabla^t (\varrho s_{\text{eff}}) = -\varrho_u S_t \nabla^t \kappa. \quad (3.40)$$

The vorticity ahead of the discontinuity vanishes, since the flow in the unburnt gas is irrotational, thus $[\boldsymbol{\omega}] = \boldsymbol{\omega}_b$. The vorticity for two-dimensional or three-dimensional, rotational symmetric flow has only a part in the z or ϑ direction, respectively. For the vorticity at the flame front in the burnt gas, we get from Eq. (3.39):

$$\omega_b = - \left(\varrho_u S_t \nabla^t \kappa [1/\varrho] + \frac{1}{\varrho_u s_{\text{eff}}} \left(\frac{D^t \mathbf{u}^t}{Dt} + (u_u^n + s_{\text{eff}}) \frac{D^t \mathbf{n}_f}{Dt} \right) \cdot \mathbf{e}^t [\varrho] \right). \quad (3.41)$$

Using Eqs. (3.19) and (3.21), we get $[1/\varrho]$:

$$[1/\varrho] = \frac{1}{\varrho_b} - \frac{1}{\varrho_u} = (\sigma - 1) P^{-1/\gamma_u}, \quad (3.42)$$

and $[\varrho]$ is obtained with Eq. (3.21):

$$[\varrho] = \varrho_b - \varrho_u = \frac{1 - \sigma}{\sigma} P^{1/\gamma_u}. \quad (3.43)$$

4. State of the Art in Industrial Applications

Here, we present one-dimensional approximations of an explosion inside a sphere with centric ignition. Those kind of models are most commonly used in the process industry. In general, this approach cannot account for the flame-flow interaction because the momentum balance is not included in the derivations.

In the first section, the model presented in Chapter 3 is reduced to one-dimensional geometries. The resulting system of ordinary differential equations are solved within seconds, compared to simulations of the ‘full’ model which take a couple of hours on modern computers. Thus, explosions inside spheres and infinitely long cylinders can be simulated. In the next section, three different approaches used in the process industry are presented.

4.1. Symmetrical Solutions for an Infinitely Long Cylinder and Sphere

To obtain results for an infinitely long cylinder and a sphere with centric ignition, the model presented in Chapter 3 is reduced to a one-dimensional, symmetrical description. This implies that all vectors, when expressed in polar or spherical coordinates, only have a radial component, e.g. for the velocity, $\mathbf{u} = u\mathbf{e}_r$, where \mathbf{e}_r is the unit vector in radial direction, as shown in Fig. 4.1. Thus, we only consider radial components which are always normal to the flame front. The flame front remains a sphere or cylinder and the vorticity vanishes, $\boldsymbol{\omega} = \mathbf{0}$.

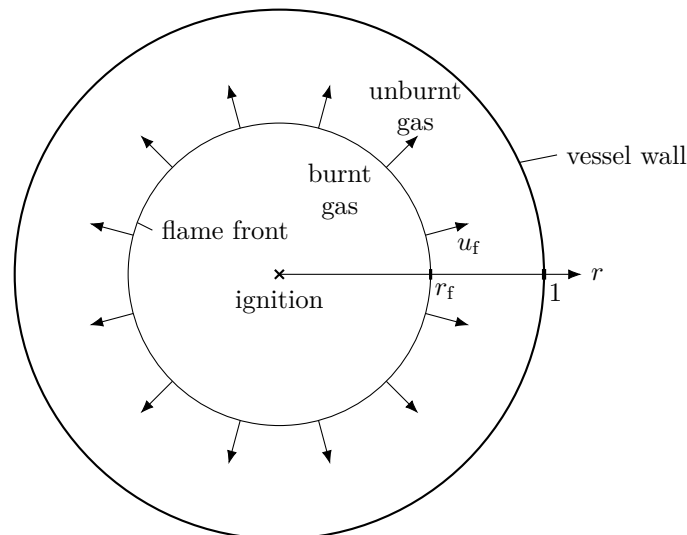


Figure 4.1.: One-dimensional approximation: an infinitely long cylinder or sphere.

4. State of the Art in Industrial Applications

In this section, we derive a system of ordinary differential equations for the leading-order pressure P and the radius of the flame front r_f , which is governed by Eq. (2.39):

$$\frac{dr_f}{dt} = u_u(r_f, t) + s_{\text{eff}}. \quad (4.1)$$

The difference of the velocity of unburnt and burnt gas at the flame front is, cf. Eq. (3.22):

$$u_u(r_f, t) - u_b(r_f, t) = \frac{\gamma_b - 1}{\gamma_b} \left(\frac{\gamma_b - \gamma_u}{(\gamma_u - 1)(\gamma_b - 1)} + \Delta h_f P^{(1-\gamma_u)/\gamma_u} \right) s_{\text{eff}}. \quad (4.2)$$

As shown in the next two subsections, the velocity of the unburnt gas always points away from the flame front towards the vessel wall, whereas the velocity of the burnt gas always points towards the origin. Solutions of this one-dimensional models are shown in Chapter 6, where they are compared to the results from the full model.

Infinitely Long Cylinder

The divergence of the velocity in a polar coordinate system, with no components or dependencies in azimuthal direction [68, Eq. (A) of Table A.7-2, p. 834], reads as:

$$\nabla \cdot \mathbf{u} = \frac{1}{r} \frac{\partial(ru)}{\partial r} = -\frac{1}{\gamma} \frac{1}{P} \frac{dP}{dt}, \quad (4.3)$$

with the general solution

$$u(r, t) = -\frac{r}{2} \frac{1}{\gamma} \frac{1}{P} \frac{dP}{dt} + \frac{f(t)}{r}. \quad (4.4)$$

$f(t)$ is a function dependent on time only and has to be chosen such that all boundary conditions are fulfilled. In the unburnt gas, the velocity must vanish at the vessel wall, $u_u(1, t) = 0$. Thus, we get:

$$u_u(r, t) = \frac{r}{2} \frac{1}{\gamma_u} \frac{1}{P} \frac{dP}{dt} (r^{-2} - 1) > 0. \quad (4.5)$$

In the burnt gas, $f_b(t) = 0$ since $u_b(0, t)$ must be finite. Thus, the velocity of the burnt gas reads as:

$$u_b(r, t) = -\frac{r}{2} \frac{1}{\gamma_b} \frac{1}{P} \frac{dP}{dt} < 0. \quad (4.6)$$

Inserting Eqs. (4.5) and (4.6) into Eq. (4.2) yields the change of pressure:

$$\frac{1}{P} \frac{dP}{dt} = \frac{2(\gamma_b - 1)}{r_f} \frac{\frac{\gamma_b - \gamma_u}{(\gamma_u - 1)(\gamma_b - 1)} + \Delta h_f P^{(1-\gamma_u)/\gamma_u}}{1 + (r_f^{-2} - 1)\gamma_b/\gamma_u} s_{\text{eff}}. \quad (4.7)$$

4. State of the Art in Industrial Applications

Inserting Eq. (4.5), evaluated at the flame front $r = r_f$, into Eq. (4.1) gives the flame speed:

$$\frac{dr_f}{dt} = \frac{r_f}{2} \frac{1}{\gamma_u} \frac{1}{P} \frac{dP}{dt} \left(r_f^{-2} - 1 \right) + s_{\text{eff}}. \quad (4.8)$$

For an infinitely long cylinder, the curvature is $\kappa = 1/(2r)$. Thus, we get a non-linear ordinary differential equation for the pressure:

$$\frac{1}{P} \frac{dP}{dt} = \frac{2(\gamma_b - 1)}{r_f} \frac{\frac{\gamma_b - \gamma_u}{(\gamma_u - 1)(\gamma_b - 1)} + \Delta h_f P^{(1-\gamma_u)/\gamma_u}}{1 + (r_f^{-2} - 1) \gamma_b/\gamma_u} \left(1 - \frac{S_t}{2r_f} \right) P^{2(\gamma_u - 1)/\gamma_u - \beta}, \quad (4.9)$$

and the flame front radius:

$$\frac{dr_f}{dt} = \frac{r_f}{2} \frac{1}{\gamma_u} \frac{1}{P} \frac{dP}{dt} \left(r_f^{-2} - 1 \right) + \left(1 - \frac{S_t}{2r_f} \right) P^{2(\gamma_u - 1)/\gamma_u - \beta}, \quad (4.10)$$

subject to the initial conditions $P(0) = 1$ and $r_f(0) = r_{f,i} > S_t/2$.

Sphere

The divergence of the velocity in spherical coordinates, with no components or dependencies on the azimuth or the inclination, reads as [68, Eq. (A) of Table A.7-3, p. 836]:

$$\nabla \cdot \mathbf{u} = \frac{1}{r^2} \frac{\partial (r^2 u)}{\partial r} = -\frac{1}{\gamma} \frac{1}{P} \frac{dP}{dt}, \quad (4.11)$$

with the general solution

$$u(r, t) = -\frac{r}{3} \frac{1}{\gamma} \frac{1}{P} \frac{dP}{dt} + \frac{f(t)}{r^2}. \quad (4.12)$$

Adaption to the boundary conditions yields for $u_u(r, t)$:

$$u_u(r, t) = \frac{r}{3} \frac{1}{\gamma_u} \frac{1}{P} \frac{dP}{dt} \left(r^{-3} - 1 \right) > 0, \quad (4.13)$$

and $u_b(r, t)$:

$$u_b(r, t) = -\frac{r}{3} \frac{1}{\gamma_b} \frac{1}{P} \frac{dP}{dt} < 0. \quad (4.14)$$

Evaluating the difference of u_u and u_b at the flame front yields an equation for the pressure rise:

$$\frac{1}{P} \frac{dP}{dt} = \frac{3(\gamma_b - 1)}{r_f} \frac{\frac{\gamma_b - \gamma_u}{(\gamma_u - 1)(\gamma_b - 1)} + \Delta h_f P^{(1-\gamma_u)/\gamma_u}}{1 + (r_f^{-3} - 1) \gamma_b/\gamma_u} s_{\text{eff}}. \quad (4.15)$$

4. State of the Art in Industrial Applications

Inserting Eq. (4.13), evaluated at the flame front $r = r_f$ into Eq. (4.1) gives the flame speed:

$$\frac{dr_f}{dt} = \frac{r_f}{3} \frac{1}{\gamma_u} \frac{1}{P} \frac{dP}{dt} \left(r_f^{-3} - 1 \right) + s_{\text{eff}}. \quad (4.16)$$

The curvature of a sphere is the inverse of its radius, $\kappa = 1/r$. Thus, the ordinary differential equation for the pressure reads as:

$$\frac{1}{P} \frac{dP}{dt} = \frac{3(\gamma_b - 1)}{r_f} \frac{\frac{\gamma_b - \gamma_u}{(\gamma_u - 1)(\gamma_b - 1)} + \Delta h_f P^{(1 - \gamma_u)/\gamma_u}}{1 + (r_f^{-3} - 1) \gamma_b / \gamma_u} \left(1 - \frac{S_t}{r_f} \right) P^{2(\gamma_u - 1)/\gamma_u - \beta}, \quad (4.17)$$

and for the flame front radius, we get:

$$\frac{dr_f}{dt} = \frac{r_f}{3} \frac{1}{\gamma_u} \frac{1}{P} \frac{dP}{dt} \left(r_f^{-3} - 1 \right) + \left(1 - \frac{S_t}{r_f} \right) P^{2(\gamma_u - 1)/\gamma_u - \beta}, \quad (4.18)$$

subject to the initial conditions $P(0) = 1$ and $r_f(0) = r_{f,i} > S_t$.

4.2. Commonly Used Models in Industry

Most commonly used in industry are the so-called global integral models. They are derived using the global mass and energy balances, and can only be solved for spheres with centric ignition. The flow field itself is not considered, since the local momentum balance is not used. Three different areas of physics have to be addressed [8]: (I) spatial structure of the problem, (II) thermodynamics and (III) combustion progress.

The spatial structure is often a two- or three-zone model, where the flame front thickness is completely neglected (two zones), or it is resolved using simplified assumptions (three zones). For the thermodynamics, isothermal and isentropic models are most commonly used. The combustion progress is often modelled with the fractional pressure rise relation. It equates the fraction of burnt mass to the fraction of pressure rise [25, 55]:

$$\frac{\tilde{m}_b}{\tilde{m}_{\text{tot}}} = \frac{\tilde{P} - \tilde{P}_1}{\tilde{P}_{\text{max}} - \tilde{P}_1}. \quad (4.19)$$

\tilde{m}_b is the mass of the burnt gas, \tilde{m}_{tot} is the total mass, i.e. the mass of unburnt and burnt gas. For the industry models, Eq. (4.19) replaces the differential equation for the flame front radius, Eqs. (4.10) and (4.18), from the previous section.

This assumption is only valid for ideal gases with constant specific heats and equal number of moles in unburnt and burnt gas, and perfect mixture, i.e. no temperature gradients in burnt and unburnt gas [8]. It was first derived by Lewis and von Elbe [55]. The assumption of a vanishing temperature gradient in the burnt gas does not hold for confined combustion [84, 25, 55]. It is an approximation which introduces errors in the order of 10% [8]. Thus, the relation is criticised because of oversimplifications [85] and it leads to systematic errors [86]. Despite this limitations, it is often used in the industrial design process of dust explosion suppression devices.

4. State of the Art in Industrial Applications

All of the relations presented here are only valid for spherical vessels. A straightforward extension to arbitrary, non-spherical geometries is not easily possible [87]. Shape parameters which quantify the deviation from a spherical vessel are used. In the following, three different modelling approaches are presented here: the simple model introduced by Nagy and colleagues from the U.S. Bureau of Mines [10, 7], a more complex model by Nomura and Tanaka [87] and the more advanced modelling by Bradley and Mitcheson [11].

Isothermal and Isentropic Model by Nagy, Conn and Verakis

One of the first to derive a mathematical model to describe dust explosions as premixed combustion of an ideal gas in closed geometries were Nagy, Conn and Verakis [10, 7]. They assume a centric ignition inside a closed vessel and implicitly an infinitely thin flame front. The authors differentiate between isothermal and isentropic conditions. Thus, they obtain two different descriptions for the rate of pressure change. By assuming that the unburnt and burnt fluid is an ideal gas, they take an averaging approach to better account for the properties of dust particles. This is done by adapting the ratio of specific heat. The burning velocity depends on the pressure and temperature according to Eq. (2.7). The influence of the geometry of the vessel is taken into account by shape factors. To account for turbulence, an empirical parameter is introduced which increases the burning rate. By taking experimental data, they conclude that the influence of turbulence leads to a five times larger burning velocity.

In their isothermal model, they assume that the temperatures of the unburnt and burnt gas remain the same throughout the explosion. For the ordinary differential equation for the rate of pressure rise, they get [1]:

$$\frac{d\tilde{P}}{d\tilde{t}} = \frac{3\tilde{s}_{\text{eff}}^0}{\tilde{r}_v\tilde{P}_i} (\tilde{P}_e - \tilde{P}_i)^{1/3} \tilde{P}_e^{2/3} (\tilde{P} - \tilde{P}_i)^{2/3} \tilde{P}^{1/3}. \quad (4.20)$$

The effective burning velocity is assumed to be independent of the pressure, thus $\beta = 0$. When using this model, the deflagration index reads as:

$$\tilde{K}_{\text{St}} = (36\pi)^{1/3} \frac{\tilde{P}_e}{\tilde{P}_i} (\tilde{P}_e - \tilde{P}_i) \tilde{s}_{\text{eff}}^0. \quad (4.21)$$

The choice of the effective burning velocity enables experimenters to adapt the pressure-time curve obtained from Eq. (4.20) to experimental data.

For isentropic conditions, the compression results in an increase in temperature of the unburnt and burnt gas, and the pressure equation reads as:

$$\frac{d\tilde{P}}{d\tilde{t}} = \frac{3\gamma\tilde{s}_{\text{eff}}^0\tilde{P}_{\text{ref}}^\beta}{\tilde{r}_v\tilde{P}_i^{2-1/\gamma}} (\tilde{P}_e^{1/\gamma} - \tilde{P}_i^{1/\gamma})^{1/3} (\tilde{P}^{1/\gamma} - \tilde{P}_i^{1/\gamma})^{2/3} \left(\frac{\tilde{P}_e}{\tilde{P}}\right)^{2/3\gamma} \tilde{P}^{3-2/\gamma-\beta}. \quad (4.22)$$

Nagy et al. conclude that by including the dependency of the burning velocity on the pressure, Eq. (4.22) produces better results when compared to experimental data than Eq. (4.20). When using the adiabatic approach and setting $\beta = 0$, the deflagration index reads as:

4. State of the Art in Industrial Applications

$$\tilde{K}_{\text{St}} = (36\pi)^{1/3} \left(\frac{\tilde{P}_e}{\tilde{P}_i} \right)^{2-1/\gamma} \left(\tilde{P}_e^{1/\gamma} - \tilde{P}_i^{1/\gamma} \right) \tilde{P}_e^{1-1/\gamma} \tilde{s}_{\text{eff}}^0. \quad (4.23)$$

The approach of Nagy and his colleagues was a very practical one: First, they had much experimental data to validate their model and find good material parameters. Next, in their derivations, they introduce a number of ad-hoc assumptions and simplifications, based on estimation of scales or constraints of validity. As mentioned, only spherical explosion events can be described by their model.

Particle Shells Model by Nomura and Tanaka

Nomura and Tanaka [87] did a detailed analysis of dust explosion propagation inside spherical and non-spherical vessels. They assume that single-sized particles are distributed uniformly on surfaces with radii $(n-1)\tilde{L}$, $n = 2, 3, \dots$ (shells of particles) from the centre of the vessel. The average distance between neighbouring particles \tilde{L} can be estimated with:

$$\tilde{L} = \left(\frac{\tilde{\rho}_s}{\tilde{c}_d} \right)^{1/3} \tilde{d}_p.$$

\tilde{c}_d is the dust concentration, $\tilde{\rho}_s$ is the particle density and \tilde{d}_p is the particle size. When the dust cloud is ignited in the centre of the vessel, the explosion is assumed to be the successive burning of neighbouring particles.

The burning velocity is defined as the velocity of the flame which travels from one shell of particles to the next. Thus, they get:

$$\tilde{s}_{\text{eff}} = \frac{\tilde{L}}{\Delta\tilde{t}_n}.$$

$\Delta\tilde{t}_n$ is the time interval for the propagation of the flame from the $(n-1)^{\text{th}}$ to the $(n)^{\text{th}}$ particle shell. For $n \rightarrow \infty$, this time reaches a constant value. Thus, \tilde{s}_{eff} is constant.

They consider heat transfer between the solid and gas phase, the change of moles in unburnt and burnt gas and derive an expression for the rate of pressure rise in a closed vessel:

$$\frac{d\tilde{P}}{d\tilde{t}} = \gamma_u \tilde{P}^{1-1/\gamma_u} \left(P_e^{1/\gamma_u} - P_i^{1/\gamma_u} \right) \frac{d\tilde{M}(t)/d\tilde{t}}{\tilde{M}_i}. \quad (4.24)$$

$\tilde{M}(t)$ is the total mass of burnt particles and can be approximated by:

$$\tilde{M}(t) = \frac{8\tilde{m}_i}{\Delta\tilde{t}^3} \tilde{t}^3.$$

\tilde{m}_i is the initial mass of all particles, and $\Delta\tilde{t} = \Delta\tilde{t}_{n \rightarrow \infty}$ is the constant limit time interval that the flame front takes to travel from one particle shell to the next. According to Eckhoff, this corresponds to a slightly adapted fractional pressure rise relation [1]:

4. State of the Art in Industrial Applications

$$\frac{\tilde{m}_b}{\tilde{m}_{\text{tot}}} = \frac{\tilde{P}^{1/\gamma} - \tilde{P}_i^{1/\gamma}}{\tilde{P}_e^{1/\gamma} - \tilde{P}_i^{1/\gamma}}.$$

For the deflagration index, they obtain:

$$\tilde{K}_{\text{St}} = \frac{\gamma_u \tilde{d}_p \tilde{P}_e}{\Delta \tilde{t}} \left(\frac{36\pi \tilde{Q}_s}{\tilde{c}_{\text{eff}}} \right)^{1/3} \left(1 - \left(\frac{\tilde{P}_i}{\tilde{P}_e} \right)^{1/\gamma_u} \right). \quad (4.25)$$

\tilde{c}_{eff} is the effective dust concentration, i.e. the actual dust concentration for fuel-lean combustion, and the stoichiometric dust concentration for fuel-rich combustion.

Nomura and Tanaka also consider flame propagation in a cylindrical vessel. However, they assume that the flame remains spherical until it touches the wall, and then the shape of the flame front is taken to be a cut-off sphere which fits into the cylinder. As shown in Chapter 7, this can only be a crude approximation to the actual shape of the flame front.

Advanced Modelling by Bradley and Mitcheson

Bradley and Mitcheson did a detailed analysis of the spherical combustion of gases [11]. In their computer model, they consider eleven different chemical species and account for temperature-dependent material parameters using data from NIST-JANAF databases. Their algorithm consists of an iterative solving procedure (cf. Fig. 3 in their paper). The flame front is modelled as having a varying thickness over time which has to be calculated in each time step.

They divide the combustion process into much smaller subprocesses. Thus, a small mass element $d\tilde{m}_u$ burns at constant pressure. The reactants do not transform immediately, but instead have to pass through the reaction zone. There, it is pre-heated, and eventually reaches its ideal equilibrium temperature. The combustion of each small mass element leads to small pressure increment. They also calculate trajectories of particles. With their results, they conclude that flow reversal happens at the flame front, and that the highest speeds occur at the beginning near the flame front in the unburnt gas. This model is called ‘computer model’ by the authors, since it can only be simulated with advanced numerical tools¹.

One of their results was that the burning velocity is not constant, but has to depend on the current thermodynamic state. Otherwise, deviations from experiments become too large. They also conclude that the pressure can be approximated by a simple power law of the time, $d\tilde{P}/d\tilde{t} \propto \tilde{t}^{3.5}$. Again, the extension to arbitrary shapes of the boundary was not done.

¹In Section 8.5.3 of his book [8], Ogle presents an adiabatic model which he states was developed by Bradley and Mitcheson. However, this model was formulated by other authors, which becomes clear when reading the original paper [11]. Fig. 8.6 from Ogle [8, page 436] does not correspond to the model presented in the corresponding section. Instead, this figure shows results from the more complex computer model with a finite and variable flame thickness, i.e. the advanced model by Bradley and Mitcheson, presented in this section here.

5. Solution Algorithm

The numerical algorithm presented in this chapter is closely adapted to the structure of the expanded governing equations from Chapter 3. We need methods to keep track of a moving discontinuity, solve Poisson's equations and the vorticity transport equation, and account for the jump of entropy and vorticity at the flame front.

Some of these tasks are easily done on a Lagrangian mesh, i.e. a mesh where the mesh points move with the flow, and others on a fixed, Eulerian mesh. For example, the entropy is constant for each material element, except when crossing the flame front. Thus, the entropy is most conveniently described on a Lagrangian mesh. When a point of this mesh jumps over the flame front, the corresponding value of the entropy is increased. On the other hand, a Poisson's equation is solved most conveniently on a regular, Cartesian grid using Fourier transformations. Thus, two types of meshes are used.

In Section 5.1, the assumption that the ratio of specific heats is the same in the unburnt and burnt gas, i.e. $\gamma_u = \gamma_b \equiv \gamma$, is introduced. While it seems to be a limitation, others have used it in their analysis as well [7, 8] with good agreement to experimental data. All governing, expanded equations relevant to the numerical algorithm are presented.

In Section 5.2, the velocity field is split into four different parts. This allows to take advantage of features of the governing equation. As an example, the fact that the divergence of the velocity field is time-dependent only is used to simplify the algorithm.

In Section 5.3, the solution procedure is given. Since the velocity field consists of different parts, a well thought-out design of the sequence of numerical calculations is necessary.

In Section 5.4, the temporal discretisation of the vorticity transport equation and pressure change is given. Since the vorticity is evaluated on moving mesh points, the material derivative corresponds to the change of a quantity defined on moving mesh points.

In Section 5.5, details about the spatial discretisation are given. Four different discretisation schemes are explained, and the calculation of the entropy gradient on a distorted grid using central finite differences is outlined. Also, the simple tracking algorithm of the flame front is described, which is tracked with marker points.

In Section 5.6, panel methods are explained. They are normally used for calculation of the flow around an airfoil. However, here they serve two purposes: (I) They enable us to combine the tracking of the flame front and the fulfilment of the jump condition for the normal velocity at the front. (II) The boundary condition at the vessel wall, a vanishing normal velocity, is satisfied using panel methods.

In Section 5.7, mathematical details on Fourier-Bessel transformations are given. We apply this concept to find a solution to a general Poisson's equation, and thus, find the vector potential. In the function space of Fourier functions, differential equations are solved with simple algebraic operations on the Fourier coefficients. Thus, taking the curl of the vector potential is also done in the Fourier space.

5.1. Full Problem Formulation

The two physical quantities that determine the velocity field are the scalar potential, cf. Eq. (3.32):

$$\nabla^2 \varphi = \nabla \cdot \mathbf{u}, \quad (5.1)$$

and the vector potential, cf. Eq. (3.34):

$$\nabla^2 \boldsymbol{\psi} = -\boldsymbol{\omega}. \quad (5.2)$$

Then, the velocity field is given by:

$$\mathbf{u} = \nabla \varphi + \nabla \times \boldsymbol{\psi}. \quad (5.3)$$

The divergence of the velocity is given by Eq. (3.13):

$$\nabla \cdot \mathbf{u} = -\frac{1}{\gamma} \frac{1}{P} \frac{dP}{dt}, \quad (5.4)$$

and the pressure change is obtained from Eq. (3.29):

$$\frac{1}{\gamma} \frac{1}{P} \frac{dP}{dt} = \frac{\sigma - 1}{V_v} \iint_{\text{f.f.}} s_{\text{eff}} dO. \quad (5.5)$$

The vorticity is governed by Eq. (3.37):

$$\frac{D\omega^{2D}}{Dt} = \frac{1}{\gamma} \frac{1}{P} \frac{dP}{dt} \omega^{2D} + \frac{1}{\gamma} \left(\nabla s \times \frac{D\mathbf{u}}{Dt} \right) \cdot \mathbf{e}_z, \quad (5.6)$$

or Eq. (3.38):

$$\frac{D\omega^{3D}}{Dt} = \left(\frac{u_r}{r} + \frac{1}{\gamma} \frac{1}{P} \frac{dP}{dt} \right) \omega^{3D} + \frac{1}{\gamma} \left(\nabla s \times \frac{D\mathbf{u}}{Dt} \right) \cdot \mathbf{e}_\vartheta. \quad (5.7)$$

Jump Conditions

The density ratio σ is obtained by setting $\gamma_u = \gamma_b$ in Eq. (3.21):

$$\sigma = 1 + \frac{\gamma - 1}{\gamma} \Delta h_f P^{(1-\gamma)/\gamma}, \quad (5.8)$$

and the jump of normal velocity is obtained from Eq. (3.22):

$$u_u^n - u_b^n = (\sigma - 1) s_{\text{eff}} = \frac{\gamma - 1}{\gamma} \Delta h_f P^{(1-\gamma)/\gamma} s_{\text{eff}}. \quad (5.9)$$

5. Solution Algorithm

The entropy of a material element in the burnt gas reads as, Eq. (3.23):

$$\exp s_b = \hat{\sigma}^{1/\gamma}, \quad (5.10)$$

where $\hat{\sigma}$ denotes the ratio of densities at the time when the material element crossed the flame front. Additionally, it is constant for a material element:

$$\frac{D \exp s_b}{Dt} = 0. \quad (5.11)$$

The burning velocity depends on the thermodynamic pressure, cf. Eq. (3.24):

$$s_{\text{eff}} = (1 - \kappa S_t) P^{2(\gamma-1)/\gamma-\beta}. \quad (5.12)$$

Eq. (3.41) yields the vorticity of the burnt gas just behind the flame front:

$$\omega_b = - \left(\varrho_u S_t \nabla^t \kappa [1/\varrho] + \frac{1}{\varrho_u s_{\text{eff}}} \left(\frac{D^t \mathbf{u}^t}{Dt} + (u_u^n + s_{\text{eff}}) \frac{D^t \mathbf{n}_f}{Dt} \right) \cdot \mathbf{e}^t[\varrho] \right). \quad (5.13)$$

5.2. Partition of the Velocity

Consider Eq. (5.1), which is valid everywhere except at the flame front, and Eq. (5.9), which relates the normal velocity of the unburnt and burnt gas at the flame front. The flame front itself is modeled as a discontinuity sheet where heat is instantaneously released. This implies a singular source of divergence or, putting it differently, a volumetric source term. The solution of Eq. (5.1) can be expanded to include the effect of the jump of normal velocity and the boundary condition at the vessel wall,

$$\varphi = \varphi_p + \varphi_d + \varphi_v. \quad (5.14)$$

These three scalar potentials correspond to three parts of the velocity field which are called $\mathbf{u}_p = \nabla \varphi_p$, $\mathbf{u}_d = \nabla \varphi_d$ and $\mathbf{u}_v = \nabla \varphi_v$, respectively.

φ_p is one particulate solution to Eq. (5.1). Looking from a physical point of view, it is induced by the negative divergence of the flow field:

$$\varphi_p = -\frac{1}{\gamma} \frac{1}{P} \frac{dP}{dt} \frac{\mathbf{x} \cdot \mathbf{x}}{6}. \quad (5.15)$$

Since it is explicitly given, it does not require any computational mesh. The corresponding velocity field reads as:

$$\mathbf{u}_p = -\frac{1}{\gamma} \frac{1}{P} \frac{dP}{dt} \frac{\mathbf{x}}{3}. \quad (5.16)$$

φ_d and φ_v are solutions to Laplace's equation with different boundary conditions:

5. Solution Algorithm

$$\nabla^2 \varphi_d = 0, \quad \nabla^2 \varphi_v = 0. \quad (5.17)$$

φ_d is obtained by solving a boundary value problem at the flame front. It is necessary to fulfil the jump condition for the normal velocity at the flame front, Eq. (5.9):

$$\varphi_d = \frac{\sigma - 1}{4\pi} \iint_{\text{f.f.}} \frac{s_{\text{eff}}}{\|\mathbf{x} - \mathbf{x}_f\|} dO. \quad (5.18)$$

Thus, $\mathbf{u}_d = \nabla \varphi_d$ fulfils the jump condition at the flame front, Eq. (5.9):

$$\mathbf{u}_d = \frac{\sigma - 1}{4\pi} \iint_{\text{f.f.}} \frac{(\mathbf{x} - \mathbf{x}_f) s_{\text{eff}}}{\|\mathbf{x} - \mathbf{x}_f\|^{3/2}} dO. \quad (5.19)$$

φ_v is determined such that $\nabla \varphi_v$ has a vanishing normal component at the vessel wall. It is determined by solving a boundary value problem at the vessel wall.

In general, the vorticity $\boldsymbol{\omega}$ yields a non-zero vector potential $\boldsymbol{\psi}$, cf. Eq. (5.2), and a non-zero velocity in unburnt and burnt gas. This is the fourth part of the velocity field $\mathbf{u}_\omega = \nabla \times \boldsymbol{\psi}$. Note, that \mathbf{u}_ω still has to be irrotational in the unburnt gas, although it is the direct result of the non-zero vorticity in the burnt gas. Finding \mathbf{u}_ω requires a grid in the whole computational domain. Since it is obtained by a spectral method, a regular, fixed Cartesian grid is used.

At the vessel wall, $\mathbf{x} = \mathbf{x}_v$, the normal part of the velocity must vanish, $\mathbf{u}(\mathbf{x}_v, t) \cdot \mathbf{n}_v = 0$. To simplify the algorithm, neither \mathbf{u}_p , \mathbf{u}_d , \mathbf{u}_ω nor the sum of those three parts fulfil this boundary condition. Instead, boundary conditions which are more appropriate to the solution method are applied. Thus, $\mathbf{u}_v = \nabla \varphi_v$ is chosen such that the wall normal velocity is:

$$\mathbf{u}_v \cdot \mathbf{n}_v = -(\mathbf{u}_p + \mathbf{u}_d + \mathbf{u}_\omega) \cdot \mathbf{n}_v = u_v^{\text{n,ind.}}. \quad (5.20)$$

This corresponds to a second boundary value problem, defined at the vessel wall (v.w.), where q_v has to be found such that Eq. (5.20) is fulfilled:

$$\varphi_v = \frac{1}{4\pi} \iint_{\text{v.w.}} \frac{q_v}{\|\mathbf{x} - \mathbf{x}_v\|} dO. \quad (5.21)$$

The resulting velocity $\mathbf{u}_v = \nabla \varphi_v$ reads as:

$$\mathbf{u}_v = \frac{1}{4\pi} \iint_{\text{v.w.}} \frac{(\mathbf{x} - \mathbf{x}_v) q_v}{\|\mathbf{x} - \mathbf{x}_v\|^{3/2}} dO. \quad (5.22)$$

To summarise, the total velocity consists of four different parts:

$$\mathbf{u} = \mathbf{u}_p + \mathbf{u}_d + \mathbf{u}_\omega + \mathbf{u}_v. \quad (5.23)$$

Thus, the velocity fulfils all boundary and jump conditions.

5.3. Solution Procedure

Since the equations for the different parts of the velocity are coupled in a non-linear way, we use an explicit time discretisation scheme. Assume that we have all relevant quantities, the velocity field \mathbf{u}_{old} , pressure P_{old} , pressure change $(dP/dt)_{\text{old}}$, vorticity $\boldsymbol{\omega}_{\text{old}}$ and the entropy in the burnt gas $s_{\text{b,old}}$, given at the previous time step, denoted by the subscript ‘old’.

The flowchart of the time-discrete algorithm is given in Fig. 5.1. First, the gradient of the entropy ∇s and the material derivative of the velocity $D\mathbf{u}/Dt$ is calculated, using the entropy, pressure and velocity from the previous time step. Then, the vorticity transport equation is solved, which yields the new vorticity field $\boldsymbol{\omega}$. With the new vorticity, we find a new vector potential $\boldsymbol{\psi}$, and a new vector potential velocity $\mathbf{u}_{\boldsymbol{\omega}}$.

For the velocity part due to heat release at the flame front \mathbf{u}_{d} , we need the pressure from the previous time step and the location of the flame front. This enables us to solve Eq. (5.18). Old pressure and old pressure rise are used to obtain the velocity part \mathbf{u}_{p} induced by the spatially uniform divergence from Eq. (5.16).

Now, we have three parts of the velocity. To get \mathbf{u}_{v} , we calculate the induced normal velocity at the vessel wall and solve a Laplace’ equation with appropriate boundary conditions, cf. Eq. (5.21).

With the total velocity field, we move the flame front to its new position, and calculate the new pressure, pressure rise and update the entropy, where necessary.

5.4. Time Discretisation

The material derivative of the velocity and vorticity, cf. Eqs. (5.6), are discretised with a first-order scheme. Since the material derivative is evaluated on a Lagrangian mesh, it reads for an arbitrary quantity b as:

$$\left(\frac{Db}{Dt}\right)^{(n+1)} \approx \frac{b^{(n+1)} - b^{(n)}}{\Delta t}. \quad (5.24)$$

The pressure equation, Eq. (5.5), is discretised with a first-order explicit Euler scheme. The right-hand side is evaluated at the previous time step and the discretised equation reads as:

$$\frac{1}{\gamma} \frac{1}{P^{(n)}} \frac{P^{(n+1)} - P^{(n)}}{\Delta t} = \frac{\sigma^{(n)} - 1}{V_{\text{v}}} \iint_{\text{f.f.}^{(n)}} s_{\text{eff}}^{(n)} dO. \quad (5.25)$$

Thus, the new pressure is:

$$P^{(n+1)} = \left(1 + \frac{(\sigma^{(n)} - 1) \gamma \Delta t}{V_{\text{v}}} \iint_{\text{f.f.}^{(n)}} s_{\text{eff}}^{(n)} dO \right) P^{(n)}. \quad (5.26)$$

5. Solution Algorithm

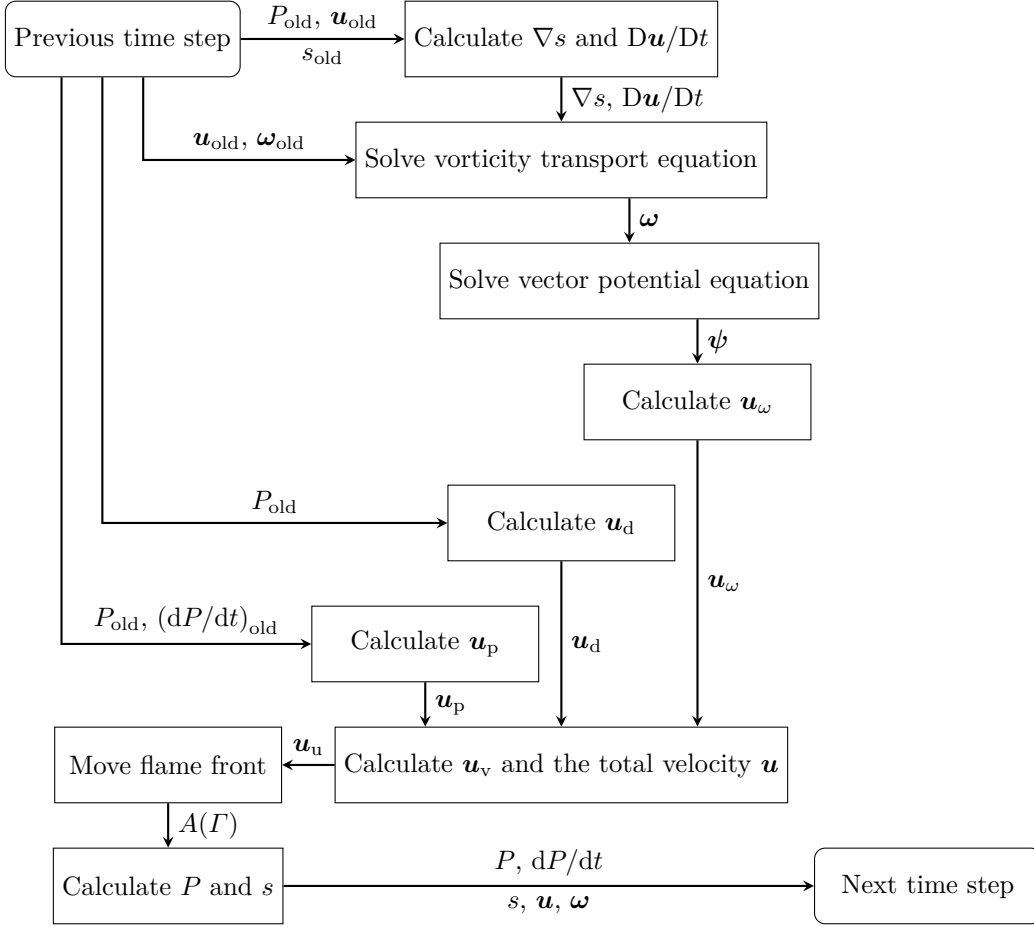


Figure 5.1.: Flowchart of the solution procedure.

The vorticity transport equation is discretised with a first-order semi-implicit Euler scheme on Lagrangian mesh points. The change of pressure, the velocity, the gradient of the entropy and the material derivative of the velocity are evaluated at the previous time step. The time-discrete two-dimensional vorticity equation is obtained from Eq. (5.6) and reads as:

$$\frac{\omega^{2D,(n+1)} - \omega^{2D,(n)}}{\Delta t} = \left(\frac{1}{\gamma} \frac{1}{P} \frac{dP}{dt} \right)^{(n)} \omega^{2D,(n+1)} + \frac{1}{\gamma} \left(\nabla s \times \frac{D\mathbf{u}}{Dt} \right)^{(n)} \cdot \mathbf{e}_z. \quad (5.27)$$

For three-dimensional, axisymmetric geometries, Eq. (5.7) yields:

$$\frac{\omega^{3D,(n+1)} - \omega^{3D,(n)}}{\Delta t} = \left(\frac{u_r}{r} + \frac{1}{\gamma} \frac{1}{P} \frac{dP}{dt} \right)^{(n)} \omega^{3D,(n+1)} + \frac{1}{\gamma} \left(\nabla s \times \frac{D\mathbf{u}}{Dt} \right)^{(n)} \cdot \mathbf{e}_\vartheta. \quad (5.28)$$

5.5. Spatial Discretisation

We use four different spatial discretisation schemes: two with non-moving meshes, for the vessel wall and the Cartesian background mesh, and two meshes which move with the flow

5. Solution Algorithm

and with the flame front, respectively. An illustration is given in Fig. 5.2.

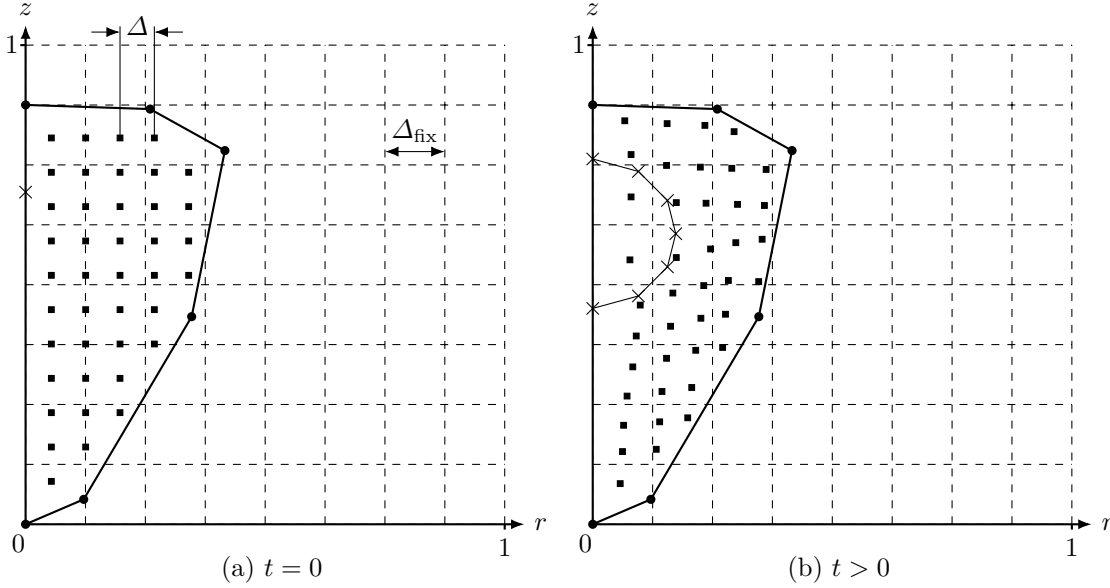


Figure 5.2.: Spatial discretisation of a rotational symmetric geometry: The flame front (×) and vessel wall (●) are discretised by marker points. Additionally, a moving mesh (■), with an initial distance between two neighbouring points of Δ , and a fixed, regular Cartesian grid (- -), with a distance of Δ_{fix} are used.

The initial flame front location, marked by a cross in Fig. 5.2a, and its initial radius are given. Marker points are placed equally spaced along the initial flame front. Additionally, Lagrangian mesh points denoted by squares in Fig. 5.2a are distributed equally spaced inside the vessel. They move with the flow, as shown in Fig. 5.2b. The initial distance between two neighbouring mesh points is Δ . The background mesh, a regular Cartesian grid, fixed in space and has a distance of Δ_{fix} between two grid points. It is shown with dashed lines in Fig. 5.2

For each time step, we have to move the Lagrangian mesh points to their new position. If a point crosses the flame front, its entropy and vorticity are updated according to the jump conditions, Eqs. (5.10) and (5.13), respectively. Then, the gradient of the entropy in the burnt gas is obtained by a central finite difference scheme on an arbitrary distorted grid. Details on the gradient calculation are given in Appendix B.

The flame front is represented by N_f connected marker points $\mathbf{x}_{f,i}$ as shown in Fig. 5.3. The points move with the front, and form a polygon. The vessel wall is represented by N_v connected vessel wall points $\mathbf{x}_{v,i}$. The connection line between two neighbouring flame front or vessel wall points is called a panel. Along the arc length of each panel, a singular volumetric source density distribution q is prescribed. For the flame front panels, the strength $q_{f,i}$ is equal to the jump of normal velocity, cf. Eq. (5.9). The source strength of the vessel wall panels is determined by the jump condition of a vanishing normal velocity. The flame front points move with the flow. Thus, the new position of each marker point at time step $(n+1)$ is:

$$\mathbf{x}_{f,i}^{(n+1)} = \mathbf{x}_{f,i}^{(n)} + \Delta t \mathbf{u}_{f,i}^{(n)}. \quad (5.29)$$

5. Solution Algorithm

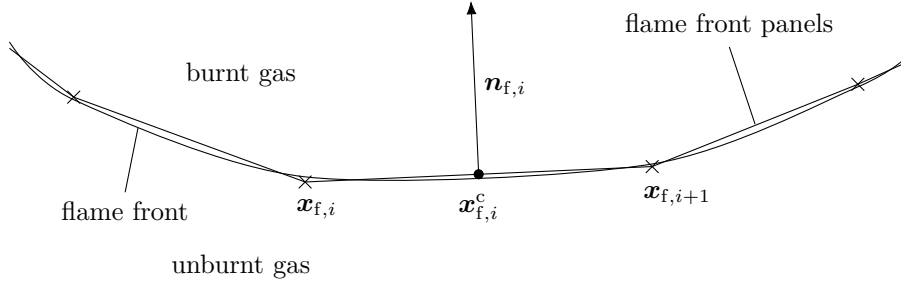


Figure 5.3.: Connected marker points $\mathbf{x}_{f,i}$ represent the flame front. The line between two adjacent points is called ‘panel’.

$\mathbf{u}_{f,i}$ is the sum of the unburnt velocity and the normal vector times the burning velocity:

$$\mathbf{u}_{f,i}^{(n)} = \mathbf{u}_{u,i}^{(n)} + s_{\text{eff},i}^{(n)} \mathbf{n}_i^{(n)}. \quad (5.30)$$

The velocity of the unburnt gas is evaluated in the middle between two marker points \mathbf{x}_f^c . Thus, it has to be interpolated using linear interpolation. Also, the normal vector is not directly available at the flame front points but found by a linear interpolation scheme:

$$\mathbf{u}_{u,i}^{\text{int}} = \frac{l_i \mathbf{u}_{u,i-1}^c + l_{i-1} \mathbf{u}_{u,i}^c}{l_i + l_{i-1}}, \quad \mathbf{n}_i^{\text{int}} = \frac{l_i \mathbf{n}_{i-1} + l_{i-1} \mathbf{n}_i}{l_i + l_{i-1}}. \quad (5.31)$$

$\mathbf{u}_{u,i}^{\text{int}}$ and $\mathbf{n}_i^{\text{int}}$ are the interpolated velocity of the unburnt gas and normal vector, respectively, at the i^{th} flame front point $\mathbf{x}_{f,i}$, l_i is the length of the i^{th} panel, $\mathbf{u}_{u,i}^c$ is the velocity of the unburnt gas evaluated in the middle between two adjacent panel points $\mathbf{x}_{f,i}^c$ and \mathbf{n}_i is the normal vector of the i^{th} panel.

The effective flame speed is calculated using the pressure of the previous time step:

$$s_{\text{eff},i}^{(n)} = \left(1 - \kappa_i^{(n)} S_t\right) \left(P^{(n)}\right)^{2(\gamma-1)/\gamma-\beta}. \quad (5.32)$$

Details on the calculation of the curvature are given in Appendix B.

Stabilisation of the Front Moving Algorithm

When choosing a sufficiently small stabilisation number, the flame front is partially unstable. This leads to a wrinkling of the flame front. In order to avoid an unphysical front tracking, we iteratively reseed the marker points during each time step, as shown in Fig. 5.4. Osher and Sethian give some details about the inherent instability of the marker particles approach when dealing with discontinuities with curvature-dependent speeds [88]. An unphysical front tracking includes self-intersection and panels which are too close together.

Two parameters have an influence on the reseeding algorithm: the average panel length l_{avg} and the minimum angle α_{min} two adjacent panels have to enclose. During each time step, all panels are checked for (I) length and (II) angle. If a panel is too short, it is

5. Solution Algorithm

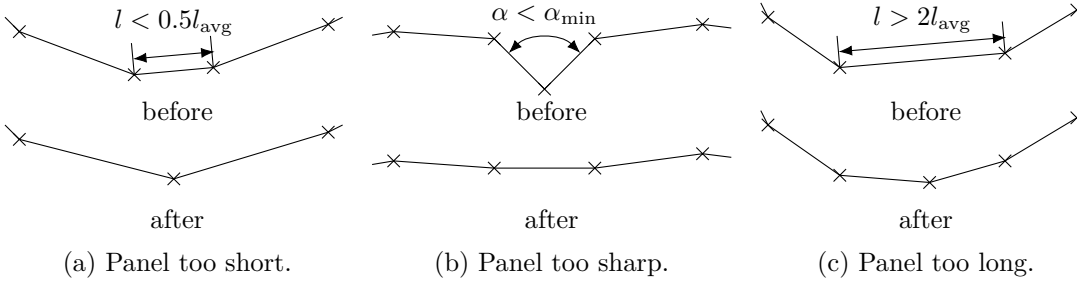


Figure 5.4.: The stabilisation and re-seeding algorithm of the flame front tracking ensures that the flame front does not self-intersect. (a) Too short panels are cut out. (b) If the angle between two adjacent panels is too small, the middle flame front marker point is removed. (c) Too long panels are split by introducing new marker points [69, Fig. 4].

removed as shown in Fig. 5.4a. When the angle between two adjacent panels is too small, as shown in Fig. 5.4b, the centre point is removed. When a panel becomes too long, as shown in Fig. 5.4c, new marker points are introduced. Special care has to be taken when there are more than one consecutive too short panels.

Note, that this stabilisation algorithm is used only for the unconfined channel combustion, to verify the front tracking algorithm. For confined combustion, stability of the flame front has to be ensured by choosing a sufficiently large turbulent stabilisation number. Otherwise, a cusp would lead to a singularity in the vorticity distribution, and the numerical algorithm would become unstable. Also, unstable modes need time to develop and a coarser discretisation of the flame front numerically damps instabilities. Thus, a smaller time step and a larger number of flame front panels also requires a larger stabilisation number (up to the limit of total stability).

5.6. Panel Methods

Panel methods are mainly used in aerodynamics to calculate the flow around airfoils under the assumption of irrotational and inviscid flow [89]. The basic idea is to superimpose fundamental solutions of Laplace's equation – in case of low Mach number flow – to fulfil all boundary conditions. The boundary geometry is approximated by straight lines, called ‘panels’. Along each panel, a singular source is prescribed. The strength of the sources of all panels is determined by solving a linear system of equations [90, 91].

Here, we adapt the panel methods as follows: The flame front and vessel wall are discretised by panels. By prescribing a singular source distribution at a panel, the normal velocity experiences a jump when crossing the panel, whereas the tangential velocity does not change. We use this feature to fulfil the jump condition of the normal velocity at the flame front. The sum of the velocities of all flame front panels \mathbf{u}_d is the solution to the boundary value problem at the flame front, Eq. (5.18).

For the vessel wall panels, we have to fulfil the boundary condition of a vanishing normal velocity at the boundaries. Thus, the source strength distribution for those panels are solution to a linear system of equations. In principle, this corresponds to a panel method

5. Solution Algorithm

for internal flow. The sum of the velocities induced by all vessel wall panels \mathbf{u}_v is the solution to Eq. (5.21).

In the first two parts, the fundamental solution of the velocity induced by a single panel for two-dimensional and rotational symmetric panels is derived. Then, the application of the panel method to find a solution to Eqs. (5.19) and (5.22) is outlined.

Two-dimensional Panels

One fundamental solution φ to Laplace's equation, corresponding to a point source with a strength q at \mathbf{x}_s in two dimensions, is:

$$\varphi = \frac{q}{2\pi} \ln \|\mathbf{x} - \mathbf{x}_s\|. \quad (5.33)$$

The velocity is simply the gradient of the potential φ :

$$\mathbf{u} = \nabla\varphi = \frac{q}{2\pi} \frac{\mathbf{x} - \mathbf{x}_s}{\|\mathbf{x} - \mathbf{x}_s\|}. \quad (5.34)$$

When dealing with two-dimensional potential flow, it is convenient to switch to a complex notation. Thus, we have the complex location $z = x + iy$, where x and y are the Cartesian coordinates (x, y) and $i = \sqrt{-1}$ is the imaginary unit. Similarly, we define a complex velocity $U = u - iv$, where the velocity in Cartesian coordinates is $\mathbf{u} = (u, v)$.

When integrating the velocity per unit length along a panel which connects the two complex points z_1 and z_2 , we get the complex velocity induced by a single panel with a source strength q :

$$U = \frac{q}{2\pi} \frac{\|z_1 - z_2\|}{z_1 - z_2} \ln \frac{z - z_2}{z - z_1}. \quad (5.35)$$

\ln is the complex-valued logarithm. When $z = z_1$ or $z = z_2$, i.e. at the panel edges, the velocity is singular. It is clear that the velocity in Cartesian coordinates is:

$$u = \Re(U), \quad v = -\Im(U). \quad (5.36)$$

\Re and \Im are the real and imaginary part of a complex number, respectively.

Three-dimensional, Rotational Symmetric Panels

In three dimensions, one fundamental solution φ to Laplace's equation with a point source, located at \mathbf{x}_s , is:

$$\varphi = \frac{q}{4\pi} \frac{1}{\|\mathbf{x} - \mathbf{x}_s\|}. \quad (5.37)$$

The resulting velocity is the gradient of φ :

5. Solution Algorithm

$$\mathbf{u} = \frac{q}{4\pi} \frac{\mathbf{x} - \mathbf{x}_s}{\|\mathbf{x} - \mathbf{x}_s\|^3}. \quad (5.38)$$

To obtain the velocity of a single panel, we have to integrate the velocity per unit area over the surface of a panel. In the case of rotational symmetric geometries, a panel is represented by a truncated cone, see Fig. A.1 in Appendix A. For the velocity in radial direction u_r , we obtain:

$$u_r = \frac{q}{\pi} \int_0^1 \frac{(r_p(s) - r) d(s)}{m(s) \sqrt{1 + m(s)}} ((m(s) - e(s)) E(m'(s)) + K(m'(s))) ds. \quad (5.39)$$

K and E are the complete elliptic integrals of the first and second kind, respectively [92]. m , d and e are parameters which depend on the geometry of the panel and the location of the point \mathbf{x} . For details, see Appendix A. The velocity u_z in the z direction reads as:

$$u_z = \frac{q}{\pi} \int_0^1 (z_p(s) - z) d(s) \frac{E(m'(s))}{\sqrt{1 + m(s)}} ds. \quad (5.40)$$

Application to the Flame Front and Vessel Wall

Along each panel i of the flame front and vessel wall, a constant source strength density q_i is prescribed. For the flame front panels, $q_{f,i}$ has to be chosen such that the jump conditions for the normal velocity is fulfilled. For the vessel wall panels, $q_{v,i}$ is determined by a linear system of equations, to fulfil the boundary condition at the vessel wall, i.e. the normal velocity must be zero.

For the flame front panels, $q_{f,i}$ is equal to the jump of the normal velocity, Eq. (5.9):

$$q_{f,i} = u_{u,i}^n - u_{b,i}^n = (\sigma - 1) s_{\text{eff},i}. \quad (5.41)$$

s_{eff} depends on the local curvature and the pressure. The velocity induced by N_f flame front panels reads as:

$$\mathbf{u}_d = \sum_{i=1}^{N_f} q_{f,i} \mathbf{u}_{f,i}^s = (\sigma - 1) \sum_{i=1}^{N_f} s_{\text{eff},i} \mathbf{u}_{f,i}^s. \quad (5.42)$$

$\mathbf{u}_{f,i}^s$ is the velocity induced by the i^{th} flame front panel with a source strength density $q_{f,i}^s = 1$.

The velocity \mathbf{u}_v is the sum of all velocities induced by the source strength densities of the N_v vessel wall panels. Thus, Eq. (5.22) yields:

$$\mathbf{u}_v = \sum_{i=1}^{N_v} q_{v,i} \mathbf{u}_{v,i}^s. \quad (5.43)$$

5. Solution Algorithm

$\mathbf{u}_{v,i}^s$ is the velocity induced by the i^{th} vessel wall panel with a source strength density $q_{v,i} = 1$. We know the value of the normal velocity at the vessel wall from Eq. (5.20). This yields N_v linear equations for the unknown source strengths $q_{v,i}$:

$$\sum_{i=1}^{N_v} q_{v,i} \mathbf{u}_{v,i}^s \cdot \mathbf{n}_{v,j} = u_{v,j}^{\text{n,ind.}} \quad (5.44)$$

$\mathbf{n}_{v,j}$ is the normal vector of the j^{th} panel, pointing outside of the vessel. The $(N_v \times N_v)$ matrix $\mathbf{A} = A_{ij} = \mathbf{u}_{v,i}^s \cdot \mathbf{n}_{v,j}$ describes the normal velocity induced by the source strength density $q_{v,i}$ of panel i at the centre of panel j . It is also called the influence matrix and is well-known from classical panel methods used in aerodynamics [91]. Thus, the source strength of the vessel wall panels q_v is the solution to the following system of equations:

$$A_{ij} q_{v,j} = u_{v,i}^{\text{n,ind.}}. \quad (5.45)$$

5.7. Fourier-Bessel Transformations

This section explains the concepts which are used to find the velocity induced by the vorticity and vector potential. Expanding a function in the Fourier-Bessel function spaces allows us to transform a function f from the Euclidean space to the Fourier-Bessel function space. The Fourier-Bessel transform is a superposition of sine, cosine and Bessel functions that approximate f in the L^2 (two-dimensional geometries) and L^{2*} (axisymmetric geometries) space. In the Fourier-Bessel function space, differential and integral equations can be solved by performing simple algebraic operations on the Fourier-Bessel coefficients.

Normally, the discrete Fourier transformation is performed on a regular, equally spaced Cartesian grid. Here, we want to find the Fourier-Bessel coefficients for $\boldsymbol{\omega}$. However, the vorticity is defined on a moving, non-regular grid, where the transformation to the Fourier-Bessel function space is not readily possible. Thus, an interpolation scheme is needed to find values of $\boldsymbol{\omega}$ on a regular, non-moving Cartesian grid. This interpolation is combined with the transformation of $\boldsymbol{\omega}$ into the Fourier-Bessel function space. Then, the solution to Poisson's equation can easily be found and yields the vector potential $\boldsymbol{\psi}$. With this, the velocity part due to vorticity \mathbf{u}_ω can be obtained by taking the curl of $\boldsymbol{\psi}$. Finally, \mathbf{u}_ω is transformed back into the Euclidean space.

Two-dimensional Fourier Transformation

We consider the function system:

$$\{\cos(2\pi(kx + ly)), \sin(2\pi(kx + ly)), k = 0, \dots, \infty, l = 0, \dots, \infty\}. \quad (5.46)$$

It forms a complete orthogonal function system on the function space:

$$L^2 = \left\{ f : [0, 1]^2 \rightarrow \mathbb{R} \mid \iint f^2 dx dy < \infty \right\}. \quad (5.47)$$

5. Solution Algorithm

Let $f(x, y) : L^2([0, 1]^2 \rightarrow \mathbb{R})$ be a periodic function with period one in x and y direction. Then, it can be expanded into a Fourier series with N and M modes:

$$f(x, y) \approx \sum_{k=0}^N \sum_{l=0}^M (a_{kl} \cos(2\pi(kx + ly)) + b_{kl} \sin(2\pi(kx + ly))), \quad (5.48)$$

with

$$\lim_{N, M \rightarrow \infty} \left\| f - \sum_{k=0}^N \sum_{l=0}^M (a_{kl} \cos(2\pi(kx + ly)) + b_{kl} \sin(2\pi(kx + ly))) \right\|_2 = 0. \quad (5.49)$$

a_{kl} and b_{kl} are the Fourier coefficients and can be obtained by integration. Note, that $b_{00} \equiv 0$, since the corresponding sine function is zero.

Solving Poisson's Equation in Two Dimensions

We need to find solutions to the vector Poisson's equation in z direction, Eq.(5.2). The Laplace operator in z direction applied to the vector potential $\boldsymbol{\psi}$ in Cartesian coordinates reads as:

$$\left[\nabla^2 \boldsymbol{\psi} \right]_z = \frac{\partial^2 \psi}{\partial x^2} + \frac{\partial^2 \psi}{\partial y^2} = -\omega(x, y). \quad (5.50)$$

The vector potential $\boldsymbol{\psi} = \psi \mathbf{e}_z$ and the vorticity $\boldsymbol{\omega} = \omega \mathbf{e}_z$ only have a component in z direction. Expanding ψ yields:

$$\psi = \sum_{k=0}^{\infty} \sum_{l=0}^{\infty} (a_{\psi,kl} \cos(2\pi(kx + ly)) + b_{\psi,kl} \sin(2\pi(kx + ly))). \quad (5.51)$$

Expanding ω yields:

$$\omega = \sum_{k=0}^{\infty} \sum_{l=0}^{\infty} (a_{\omega,kl} \cos(2\pi(kx + ly)) + b_{\omega,kl} \sin(2\pi(kx + ly))). \quad (5.52)$$

By inserting the expanded vorticity and vector potential, Eqs. (5.51) and (5.52), into Eq. (5.50) and comparing the coefficients, we get for $a_{\psi,kl}$:

$$a_{\psi,kl} = \begin{cases} 0 & k = 0 \text{ and } l = 0, \\ -a_{\omega,kl}/(4\pi^2(k^2 + l^2)) & \text{else,} \end{cases} \quad (5.53)$$

and $b_{\psi,kl}$:

$$b_{\psi,kl} = \begin{cases} 0 & k = 0 \text{ and } l = 0, \\ -b_{\omega,kl}/(4\pi^2(k^2 + l^2)) & \text{else.} \end{cases} \quad (5.54)$$

5. Solution Algorithm

The Curl Operator in Two Dimensions

Expanding the velocity $u_{\omega,x}$ in x direction into a Fourier series yields:

$$u_{\omega,x} = \sum_{k=0}^{\infty} \sum_{l=0}^{\infty} (a_{x,kl} \cos(2\pi(kx + ly)) + b_{x,kl} \sin(2\pi(kx + ly))). \quad (5.55)$$

The expanded velocity $u_{\omega,y}$ in y direction reads as:

$$u_{\omega,y} = \sum_{k=0}^{\infty} \sum_{l=0}^{\infty} (a_{y,kl} \cos(2\pi(kx + ly)) + b_{y,kl} \sin(2\pi(kx + ly))). \quad (5.56)$$

To get the velocity field $\mathbf{u}_{\omega} = (u_{\omega,x}, u_{\omega,y})$, we take the curl of the vector potential, cf. Eq. (5.3). For $u_{\omega,x}$, we get:

$$u_{\omega,x} = \frac{\partial \psi}{\partial y}. \quad (5.57)$$

$u_{\omega,y}$ reads as:

$$u_{\omega,y} = -\frac{\partial \psi}{\partial x}. \quad (5.58)$$

Inserting the expanded quantities, Eqs. (5.51) and (5.55), into Eq. (5.57) and comparing the coefficients yields $a_{x,kl}$:

$$a_{x,kl} = 2\pi l b_{\psi,kl} = -\frac{1}{2\pi} \frac{l}{k^2 + l^2} b_{\omega,kl}, \quad (5.59)$$

and $b_{x,kl}$:

$$b_{x,kl} = -2\pi l a_{\psi,kl} = \frac{1}{2\pi} \frac{l}{k^2 + l^2} a_{\omega,kl}, \quad (5.60)$$

Putting Eqs. (5.59) and (5.60) into Eq. (5.55), $u_{\omega,x}$ reads as:

$$u_{\omega,x} = \frac{1}{2\pi} \sum_{k=0}^{\infty} \sum_{l=0}^{\infty} \frac{l}{k^2 + l^2} (a_{\omega,kl} \sin(2\pi(kx + ly)) - b_{\omega,kl} \cos(2\pi(kx + ly))). \quad (5.61)$$

Inserting the expanded quantities, Eqs. (5.51) and (5.56), into Eq. (5.58), comparing the coefficients and using Eqs. (5.53) and (5.54) yields $a_{x,kl}$:

$$a_{y,kl} = -2\pi k b_{\psi,kl} = \frac{1}{2\pi} \frac{k}{k^2 + l^2} b_{\omega,kl}, \quad (5.62)$$

and $b_{y,kl}$:

$$b_{y,kl} = 2\pi k a_{\psi,kl} = -\frac{1}{2\pi} \frac{k}{k^2 + l^2} a_{\omega,kl}. \quad (5.63)$$

5. Solution Algorithm

Putting Eqs. (5.62) and (5.63) into Eq. (5.56), $u_{\omega,y}$ reads as:

$$u_{\omega,y} = \frac{1}{2\pi} \sum_{k=0}^{\infty} \sum_{l=0}^{\infty} \frac{k}{k^2 + l^2} (b_{\omega,kl} \cos(2\pi(kx + ly)) - a_{\omega,kl} \sin(2\pi(kx + ly))). \quad (5.64)$$

Axisymmetric Fourier-Bessel Transformation

We consider the function system in cylindrical coordinates (r, z) :

$$\{J_1(\lambda_k r) \cos(2\pi lz), J_1(\lambda_k r) \sin(2\pi lz), k = 1, \dots, \infty, l = 0, \dots, \infty\}. \quad (5.65)$$

It forms a complete, orthogonal function system on the function space:

$$L^{2*} = \left\{ f : [0, 1]^2 \rightarrow \mathbb{R} \mid \iint r f^2 dr dz < \infty \right\}. \quad (5.66)$$

λ_k is the k^{th} root of $J_1(\lambda_k) = 0$. J_ν is the Bessel function of the first kind, solution to the differential equation [93],

$$\frac{d^2 J_\nu(r)}{dr^2} + \frac{1}{r} \frac{dJ_\nu(r)}{dr} + \left(1 - \frac{\nu^2}{r^2}\right) J_\nu(r) = 0. \quad (5.67)$$

Let $f(r, z) : L^{2*}([0, 1]^2 \rightarrow \mathbb{R})$ be a function in cylindrical coordinates (r, z) with no dependency on ϑ direction. It is periodic in z direction with period one, and vanishes at $r = 1$, $f(1, z) = 0$. Then, it can be expanded into a Fourier-Bessel series:

$$f(r, z) \approx \sum_{k=1}^N \sum_{l=0}^M J_1(\lambda_k r) (c_{kl} \cos(2\pi lz) + d_{kl} \sin(2\pi lz)), \quad (5.68)$$

with

$$\lim_{N, M \rightarrow \infty} \left\| f(r, z) - \sum_{k=1}^N \sum_{l=0}^M J_1(\lambda_k r) (c_{kl} \cos(2\pi lz) + d_{kl} \sin(2\pi lz)) \right\|_{2*} = 0. \quad (5.69)$$

c_{kl} and d_{kl} are called Fourier-Bessel coefficients. Since the function space is orthogonal, they can be obtained by integration. Note, that $d_{k0} \equiv 0$, since the corresponding sine function is zero.

Solving Poisson's Equation in the Axisymmetric Case

We need to find solutions to the vector Poisson's equation in ϑ direction, Eq. (5.2). The vector Laplace operator ϑ direction in cylindrical coordinates, with no dependence on ϑ (rotational symmetric), applied to the vector potential ψ reads as [68, Eq. (N) of Table A.7-2, p. 834]:

5. Solution Algorithm

$$\left[\nabla^2 \boldsymbol{\psi}\right]_{\vartheta} = \frac{\partial^2 \psi}{\partial r^2} + \frac{1}{r} \frac{\partial \psi}{\partial r} - \frac{\psi}{r^2} + \frac{\partial^2 \psi}{\partial z^2} = -\omega(r, z), \quad (5.70)$$

In the axisymmetric case, the vector potential $\boldsymbol{\psi} = \psi \mathbf{e}_{\vartheta}$ and the vorticity $\boldsymbol{\omega} = \omega \mathbf{e}_{\vartheta}$ only have a component in the ϑ direction. Expanding ψ yields:

$$\psi(r, z) = \sum_{k=1}^{\infty} \sum_{l=0}^{\infty} J_1(\lambda_k r) (c_{\psi,kl} \cos(2\pi l z) + d_{\psi,kl} \sin(2\pi l z)). \quad (5.71)$$

Expanding ω yields:

$$\omega(r, z) = \sum_{k=1}^{\infty} \sum_{l=0}^{\infty} J_1(\lambda_k r) (c_{\omega,kl} \cos(2\pi l z) + d_{\omega,kl} \sin(2\pi l z)), \quad (5.72)$$

A coordinate transformation of Eq. (5.67) with $\nu = 1$ yields:

$$\left(\frac{d^2}{dr^2} + \frac{1}{r} \frac{d}{dr} - \frac{1}{r^2}\right) J_1(\lambda_k r) = -\lambda_k^2 J_1(\lambda_k r). \quad (5.73)$$

Thus, the Laplace operator can be expressed with:

$$\begin{aligned} \left(\frac{\partial^2}{\partial r^2} + \frac{1}{r} \frac{\partial}{\partial r} - \frac{1}{r^2} + \frac{\partial^2}{\partial z^2}\right) J_1(\lambda_k r) (c_{\psi,kl} \cos(2\pi l z) + d_{\psi,kl} \sin(2\pi l z)) = \\ - (4\pi^2 l^2 + \lambda_k^2) J_1(\lambda_k r) (c_{\psi,kl} \cos(2\pi l z) + d_{\psi,kl} \sin(2\pi l z)). \end{aligned} \quad (5.74)$$

By inserting the expanded vorticity and vector potential, Eqs (5.71) and (5.72), into Eq. (5.70), using Eq. (5.74) and comparing the coefficients, we get for $c_{\psi,kl}$:

$$c_{\psi,kl} = -\frac{c_{\omega,kl}}{4\pi^2 l^2 + \lambda_k^2}, \quad (5.75)$$

and $d_{\psi,kl}$:

$$d_{\psi,kl} = -\frac{d_{\omega,kl}}{4\pi^2 l^2 + \lambda_k^2}. \quad (5.76)$$

The Curl Operator in the Axisymmetric Case

Expanding the velocity $u_{\omega,r}$ in r direction yields:

$$u_{\omega,r} = \sum_{k=1}^{\infty} \sum_{l=0}^{\infty} J_1(\lambda_k r) (c_{r,kl} \cos(2\pi l z) + d_{r,kl} \sin(2\pi l z)). \quad (5.77)$$

To get the velocity field $\mathbf{u}_{\omega} = (u_{\omega,r}, u_{\omega,z})$, we take the curl of $\boldsymbol{\psi} = \psi \mathbf{e}_{\vartheta}$. For $u_{\omega,r}$, we get [68, Eq. (G) of Table A.7-2, p. 834]:

5. Solution Algorithm

$$u_{\omega,r} = -\frac{\partial\psi}{\partial z}, \quad (5.78)$$

Inserting the expanded quantities, Eqs. (5.71) and (5.77), into Eq. (5.78), comparing the coefficients and using Eqs. (5.75) and (5.76) yields $c_{r,kl}$:

$$c_{r,kl} = 2\pi l d_{\psi,kl} = -\frac{1}{2\pi} \frac{l}{l^2 + (\lambda_k/2\pi)^2} d_{\omega,kl}, \quad (5.79)$$

and $d_{r,kl}$:

$$d_{r,kl} = -2\pi l c_{\psi,kl} = \frac{1}{2\pi} \frac{l}{l^2 + (\lambda_k/2\pi)^2} c_{\omega,kl}. \quad (5.80)$$

Putting Eqs. (5.79) and (5.80) into Eq. (5.77), $u_{\omega,r}$ reads as:

$$u_{\omega,r} = \frac{1}{2\pi} \sum_{k=1}^{\infty} \sum_{l=0}^{\infty} \frac{l}{l^2 + (\lambda_k/2\pi)^2} J_1(\lambda_k r) (c_{\omega,kl} \sin(2\pi l z) - d_{\omega,kl} \cos(2\pi l z)). \quad (5.81)$$

$u_{\omega,z}$ can be determined with [68, Eq. (I) of Table A.7-2, p. 834]:

$$u_{\omega,z} = \frac{1}{r} \frac{\partial(r\psi)}{\partial r}. \quad (5.82)$$

To solve Eq. (5.82), we need the identity [93, Eq. (9.1.30)]:

$$\left(\frac{1}{r^k} \frac{d}{dr} \right)^k (r^\nu J_\nu(r)) = r^{\nu-k} J_{\nu-k}(r), \quad (5.83)$$

with $k = 1$ and $\nu = 1$:

$$\frac{1}{r} \frac{d(rJ_1(r))}{dr} = J_0(r). \quad (5.84)$$

Applying a simple transformation, we get:

$$\frac{1}{r} \frac{d(rJ_1(\lambda_k r))}{dr} = \lambda_k J_0(\lambda_k r). \quad (5.85)$$

Inserting the expanded vector potential, Eq. (5.71), into Eq. (5.82), using Eqs. (5.75), (5.76) and (5.85) yields $c_{z,kl}$:

$$c_{z,kl} = \lambda_k c_{\psi,kl} = -\frac{\lambda_k}{4\pi^2 l^2 + \lambda_k^2} c_{\omega,kl}, \quad (5.86)$$

and $d_{z,kl}$:

$$d_{z,kl} = \lambda_k d_{\psi,kl} = -\frac{\lambda_k}{4\pi^2 l^2 + \lambda_k^2} d_{\omega,kl}. \quad (5.87)$$

5. Solution Algorithm

With Eqs. (5.86) and (5.87), the expanded velocity $u_{\omega,z}$ in z direction reads as:

$$u_{\omega,z} = - \sum_{k=1}^{\infty} \sum_{l=0}^{\infty} \frac{\lambda_k}{4\pi^2 l^2 + \lambda_k^2} J_0(\lambda_k r) (c_{\omega,kl} \cos(2\pi l z) + d_{\omega,kl} \sin(2\pi l z)). \quad (5.88)$$

Note, that J_0 is used here.

Finding the Best-fit Transform on an Arbitrary Grid

Expanding the vorticity ω_i , which is defined at the M moving mesh points \mathbf{x}_i , yields for two-dimensional geometries:

$$\omega_i \approx \sum_{k=0}^{N/2-1} \sum_{l=0}^{N/2-1} (a_{\omega,kl} \cos(2\pi(kx_i + ly_i)) + b_{\omega,kl} \sin(2\pi(kx_i + ly_i))), \quad (5.89)$$

and in the axisymmetric case:

$$\omega_i \approx \sum_{k=0}^N \sum_{l=0}^{N/2-1} J_1(\lambda_k r_i) (c_{\omega,kl} \cos(2\pi l z_i) + d_{\omega,kl} \sin(2\pi l z_i)). \quad (5.90)$$

N is the number of grid points of the fixed, Cartesian grid, $N = 1/\Delta_{\text{fix}}$. The well-known formulas for the inverse discrete Fourier transform cannot be applied when the data is given on a non-equidistant grid. Since the vorticity is defined at arbitrary locations, Eqs. (5.89) and (5.90) are in general not satisfied. Thus, the solution is to find the best-fit coefficients. The best-fit coefficients are defined as the coefficients that minimise the norm of the residual. For two-dimensional geometries, this corresponds to the following minimisation problem:

$$\min_{a_{kl}, b_{kl}} \left(\sum_{i=1}^M \left(\omega_i - \sum_{k=0}^{N/2-1} \sum_{l=0}^{N/2-1} (a_{\omega,kl} \cos(2\pi(kx_i + ly_i)) + b_{\omega,kl} \sin(2\pi(kx_i + ly_i))) \right)^2 \right). \quad (5.91)$$

In the axisymmetric case, the minimisation problem reads as:

$$\min_{c_{kl}, d_{kl}} \left(\sum_{i=1}^M r_i \left(\omega_i - \sum_{k=1}^N \sum_{l=0}^{N/2-1} J_1(\lambda_k r_i) (c_{\omega,kl} \cos(2\pi l z_i) + d_{\omega,kl} \sin(2\pi l z_i)) \right)^2 \right). \quad (5.92)$$

In matrix-vector form, Eq. (5.91) reads as:

$$\min_{e_j} \left(\sum_{i=1}^M \left(\omega_i(x_i, y_i) - \sum_{j=1}^K T_{ij} e_j \right)^2 \right), \quad (5.93)$$

5. Solution Algorithm

and Eq. (5.92) yields:

$$\min_{e_j} \left(\sum_{i=1}^M r_i \left(\omega_i(r_i, z_i) - \sum_{j=1}^K T_{ij} e_j \right)^2 \right), \quad (5.94)$$

$\mathbf{T} = T_{ij}$ is the transformation matrix and $\mathbf{e} = e_j$ is a vector with all non-trivial Fourier coefficients of length K . Note, that b_{00} and d_{k0} in Eqs. (5.91) and (5.92) are meaningless, since the corresponding sine function is identical to zero. Thus, they have to be excluded from \mathbf{e} . Otherwise, the transformation matrix would be singular. We demand that $\mathbf{T}^\top \cdot \mathbf{T}$ is invertible, i.e. there are more data points ω_i than the total number of coefficients, $M > K$. Thus, the solution \mathbf{e} to Eq. (5.93) is unique and given by [94]:

$$T_{ki} T_{ij} e_j = T_{ki} \omega_i, \quad (5.95)$$

For the solution to Eq. (5.94), a simple transformation is used to obtain Eq. (5.95):

$$\sqrt{r_i} T_{ij} \rightarrow T_{ij}, \quad \sqrt{r_i} \omega_i \rightarrow \omega_i. \quad (5.96)$$

The coefficient vector is obtained by:

$$e_j = (T_{kl} T_{lj})^{-1} T_{ki} \omega_i. \quad (5.97)$$

$(*)^{-1}$ denotes the inverse of a matrix. $(\mathbf{T}^\top \cdot \mathbf{T})^{-1} \cdot \mathbf{T}^\top = (T_{kl} T_{lj})^{-1} T_{ki}$ is called the pseudo inverse.

6. Verification

Verification of the implementation is done with two different approaches: First, the solution of the one-dimensional model, presented in Section 4.1, is compared to the result of the full model, which is also able to simulate an explosion inside an infinitely long cylinder and a sphere with centric ignition. Next, the flame front tracking algorithm is verified by comparing results from unconfined combustion inside a channel with almost constant pressure to the linear stability analysis. In the first section, the choice of the numerical parameters is explained.

6.1. Choice of Numerical Parameters

There are a number of numerical parameters that have to be set. Those parameters are the initial distance between two moving mesh points Δ , the number of flame front panels N_f , the number of vessel wall panels N_v and the time step Δt . The right choice ensures that the discretisation is good enough to resolve the flame front and capture the influence of the vorticity while keeping the computational efforts in limits. With the help of Δ , the program chooses the distance between two fixed grid points Δ_{fix} such that the minimisation problem of finding the Fourier coefficients of the vorticity is unique.

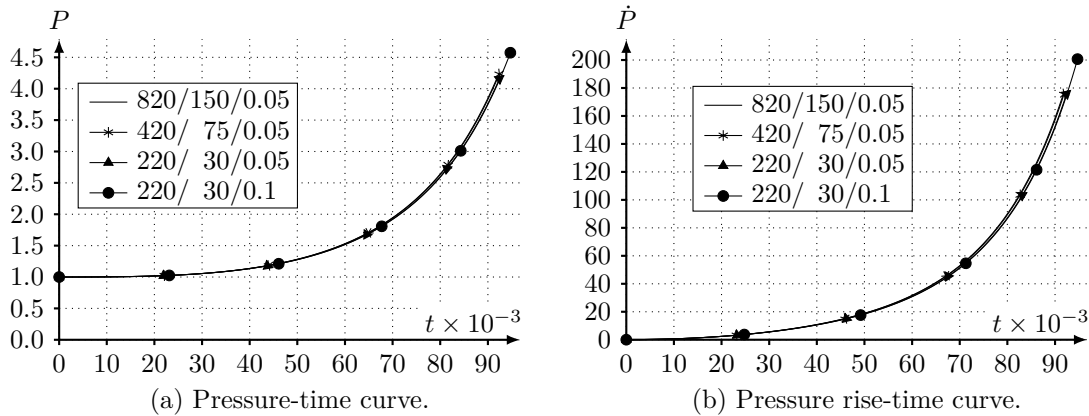


Figure 6.1.: Influence of the spatial discretisation on the pressure-time and pressure rise-time curves in a cylinder. Four different levels of discretisation are shown ($N_v/N_f/\Delta$).

The stabilisation number has to be large enough to guarantee a smooth flame front interface. Numerical experiments showed that a value of $S_t = 0.01$ is large enough to achieve this. When using only $N_f = 30$ flame front panels, the panels are so large that individual flame front panels become visible, see Figs. 6.3c and 6.3d. Thus, the flame front would

6. Verification

be underresolved. For $N_f = 75$, there are no individual panels visible any more, shown in Fig. 6.3b. To ensure high accuracy, $N_f = 150$ is chosen, see Fig. 6.3a.

The initial distance between two neighbouring, moving mesh points Δ influences the accuracy of the numerical solution of the vorticity transport equation. The influence of the vorticity is stronger in later stages of the combustion process. Since it is only non-zero in the burnt gas, enough grid points have to be inside the flame front. When choosing $\Delta = 0.05$, there are 16 Fourier modes available in each direction, $\Delta_{\text{fix}} = 0.0625$. Also, the number of moving mesh points in the burnt gas is sufficiently large, as shown in Fig. 6.4a, for $t = 0.06$. For $\Delta = 0.1$, only 8 Fourier modes are available in each direction, and the number of points inside the flame front becomes very low, as shown in Fig. 6.4d. Thus, $\Delta = 0.05$ is chosen for the simulations.

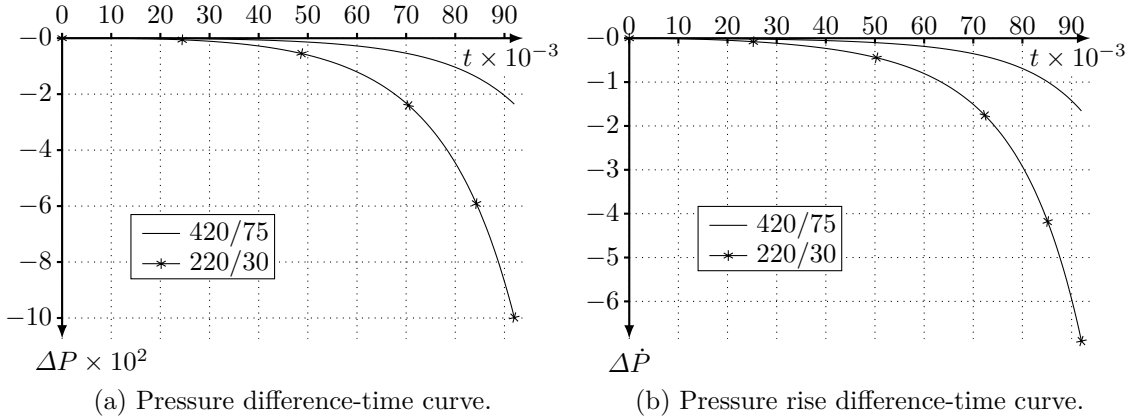


Figure 6.2.: The difference in pressure and pressure rise of two different numbers of vessel wall and flame front panels are shown. Basis of the comparison are the results from the simulation with the largest number (820/150) of panels of vessel wall and flame front (N_v/N_f).

The choice of the time step depends on the spatial discretisation. A finer spatial discretisation, especially of the flame front, calls for a smaller time step, because the numerical algorithm becomes unstable if the time step is too large. Additionally, a larger stabilisation number also requires a smaller time step. Otherwise, the flame front tracking is numerically unstable. Here, it is found that when $S_t = 0.01$ and $N_f = 150$, $\Delta t = 5 \times 10^{-6}$ is low enough to ensure a stable front tracking. For cylindrical vessels, the number of vessel wall panels is set to $N_v = 820$. To avoid numerical problems with the panel method, the corners were rounded.

Fig. 6.1 shows the influence of the spatial discretisation on the pressure. All simulations with $\Delta = 0.05$ yield a very similar pressure history. In the simulation with $\Delta = 0.1$, the flame front touches the vessel wall at a significantly later time $t = 0.0954$. Thus, the end pressure is larger as well, compared to the other three simulations.

To quantify the influence of the spatial discretisation, the difference of the pressure and pressure rise is computed and shown in Fig. 6.2. The basis for the comparison are the results from the simulation with the largest number of vessel wall and flame front panels ($N_v = 820/N_f = 150$). As expected, a better resolved vessel wall and flame front yields less deviation. The choice of $N_v = 820$ yields good results while keeping the simulation time low.

6. Verification

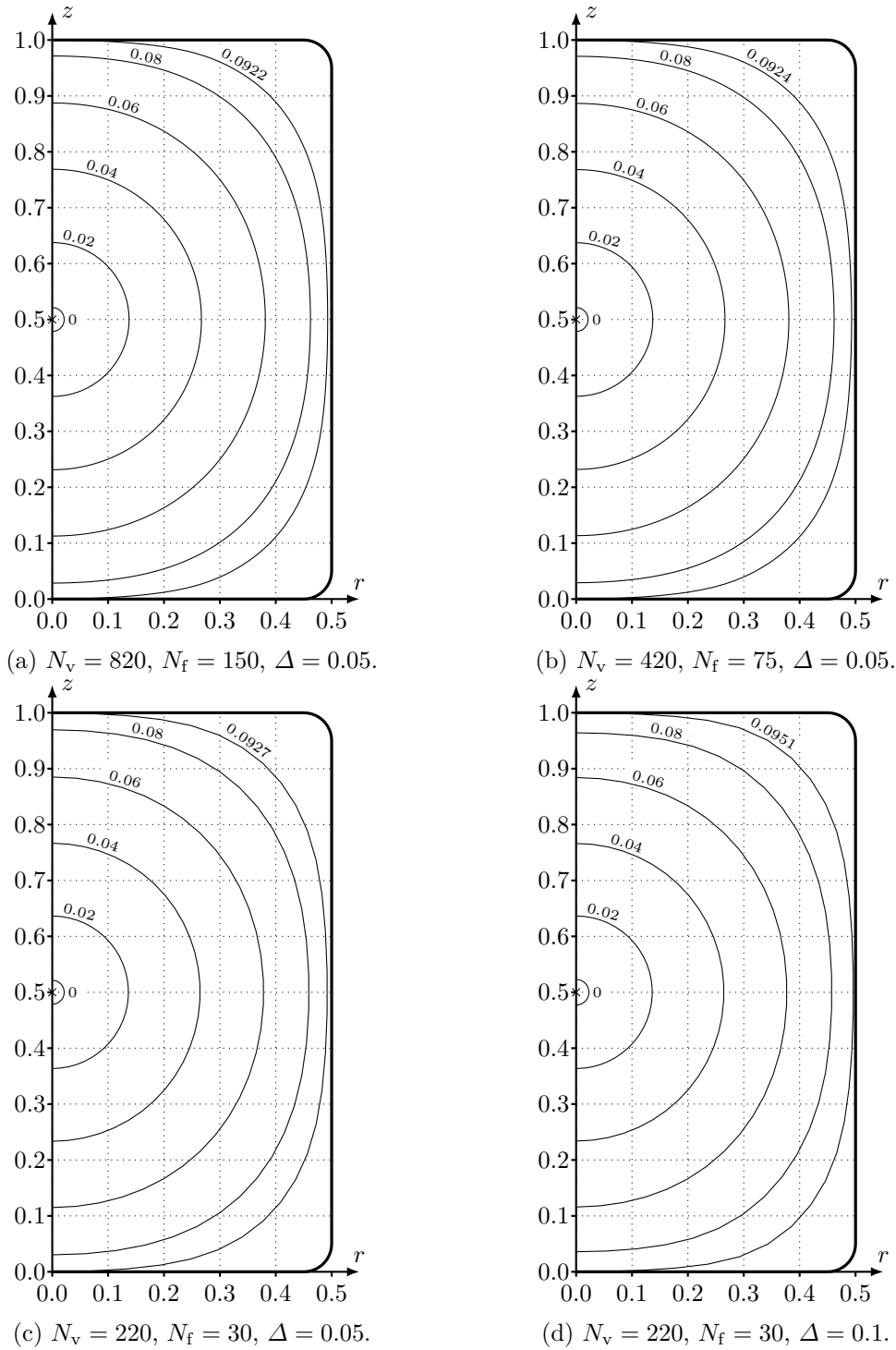


Figure 6.3.: Influence of the spatial discretisation on the shape of the flame front in a cylinder. The position of the flame front is shown for different times.

6. Verification

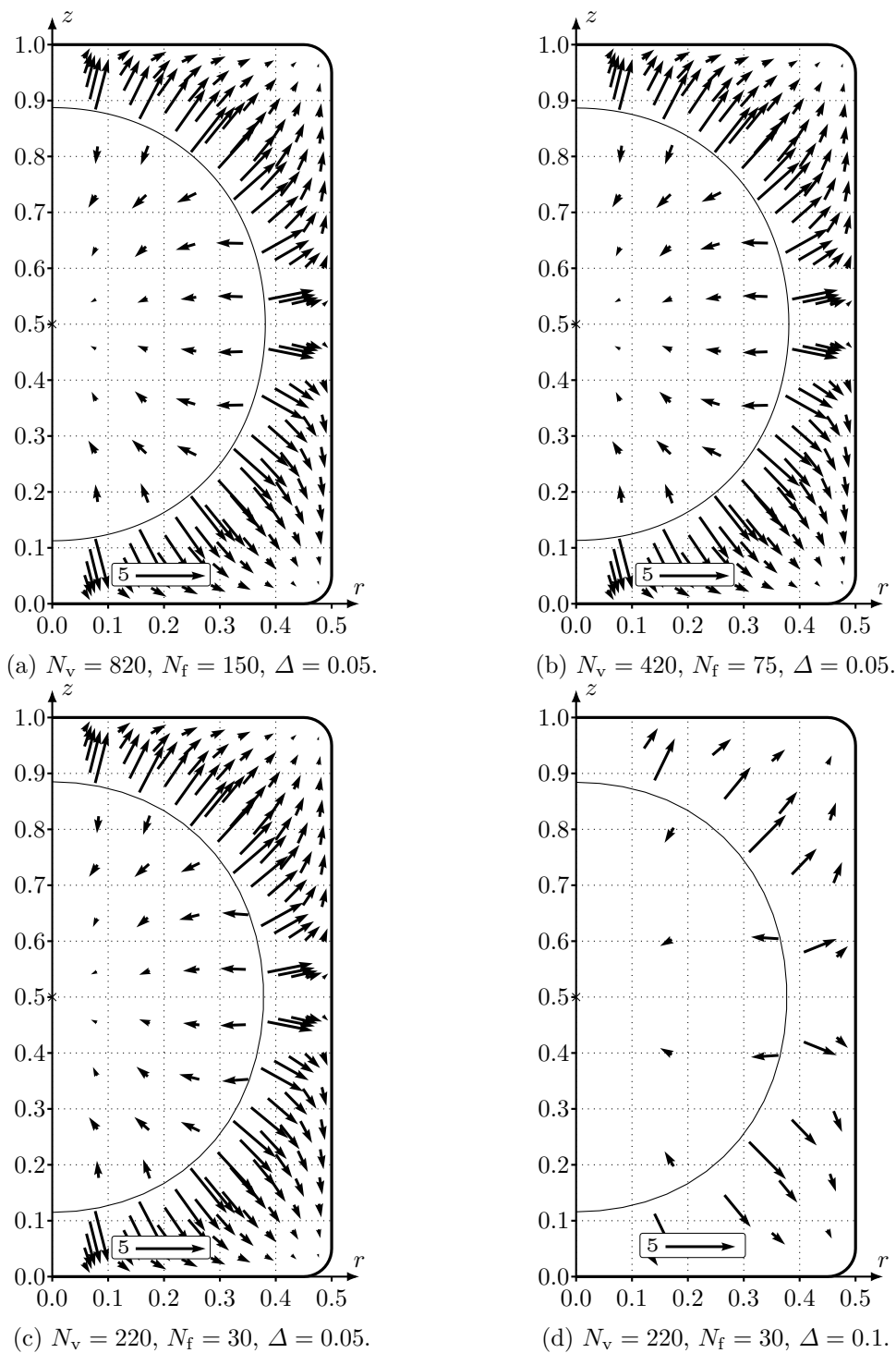


Figure 6.4.: Influence of the spatial discretisation on the velocity in a cylinder for time $t = 0.06$. The position of the flame front is shown for different times.

6.2. Comparison with the One-dimensional Model

The solution of the combustion inside an infinitely long cylinder or a sphere, where the ignition is at the centre, is known from the simplified, one-dimensional model, as outlined in Chapter 4.

For an infinitely long cylinder, Eqs. (4.9) and (4.10) have to be solved for $\gamma_u = \gamma_b$. For the pressure, the differential equation reads as:

$$\frac{dP}{dt} = 2(\gamma - 1) \Delta h_f r_f \left(1 - \frac{S_t}{2r_f}\right) P^{2-1/\gamma-\beta}, \quad (6.1)$$

and the equation for the radius of the flame front is:

$$\frac{dr_f}{dt} = \frac{r_f}{2} \frac{1}{\gamma} \frac{1}{P} \frac{dP}{dt} \left(r_f^{-2} - 1\right) + \left(1 - \frac{S_t}{2r_f}\right) P^{2(\gamma-1)/\gamma-\beta}. \quad (6.2)$$

For a sphere, setting $\gamma_u = \gamma_b$ in Eq. (4.17) yields:

$$\frac{dP}{dt} = 3(\gamma - 1) \Delta h_f r_f^2 \left(1 - \frac{S_t}{r_f}\right) P^{2-1/\gamma-\beta}, \quad (6.3)$$

and Eq. (4.18) yields:

$$\frac{dr_f}{dt} = \frac{r_f}{3} \frac{1}{\gamma} \frac{1}{P} \frac{dP}{dt} \left(r_f^{-3} - 1\right) + \left(1 - \frac{S_t}{r_f}\right) P^{2(\gamma-1)/\gamma-\beta}, \quad (6.4)$$

In this section, the pressure, pressure rise, radius and absolute flame speed are plotted against time. In all figures, the line with no markers is obtained by the simulation of the full model, and the line marked with a triangle is the result of the ordinary differential equations of the one-dimensional model. If the curves for equal β would deviate, this would imply that the implementation is not correct. Since the lines with and without markers coincide, no errors in the implementation have been found by this verification step.

The pressure-time curves show an exponential increase in time, see Figs. 6.5a and 6.6a. The reaction enthalpy Δh_f is chosen such that the end pressure is $p_e \approx 9$. With decreasing β , the pressure rise reaches a significant higher maximum value, as shown in Figs. 6.5b and 6.6b. $\beta = 0.5$ implies that the burning velocity is almost independent of pressure and temperature for $\gamma = 1.4$, as evaluation of the exponent of the second term in Eq. (6.2) indicates.

Due to the non-zero stabilisation number, the radius-time curve has a point of inflection, see Figs. 6.5c and 6.6c. Thus, the resulting flame front speed curves have a maximum, shown in Figs. 6.5d and 6.6d.

All results show that the full simulation almost perfectly matches the solution of the one-dimensional model. The parameters of the simulation were: $\Delta t = 10^{-5}/5 \times 10^{-5}$ (two-dimensional / axisymmetric case), $\Delta = 0.05$, $\Delta_{\text{fix}} = 0.0625$, $S_t = 0.01$, $\gamma = 1.4$, $r_i = 0.02$, $\Delta h_f = 20$, $N_f = 150$ and $N_v = 800$.

6. Verification

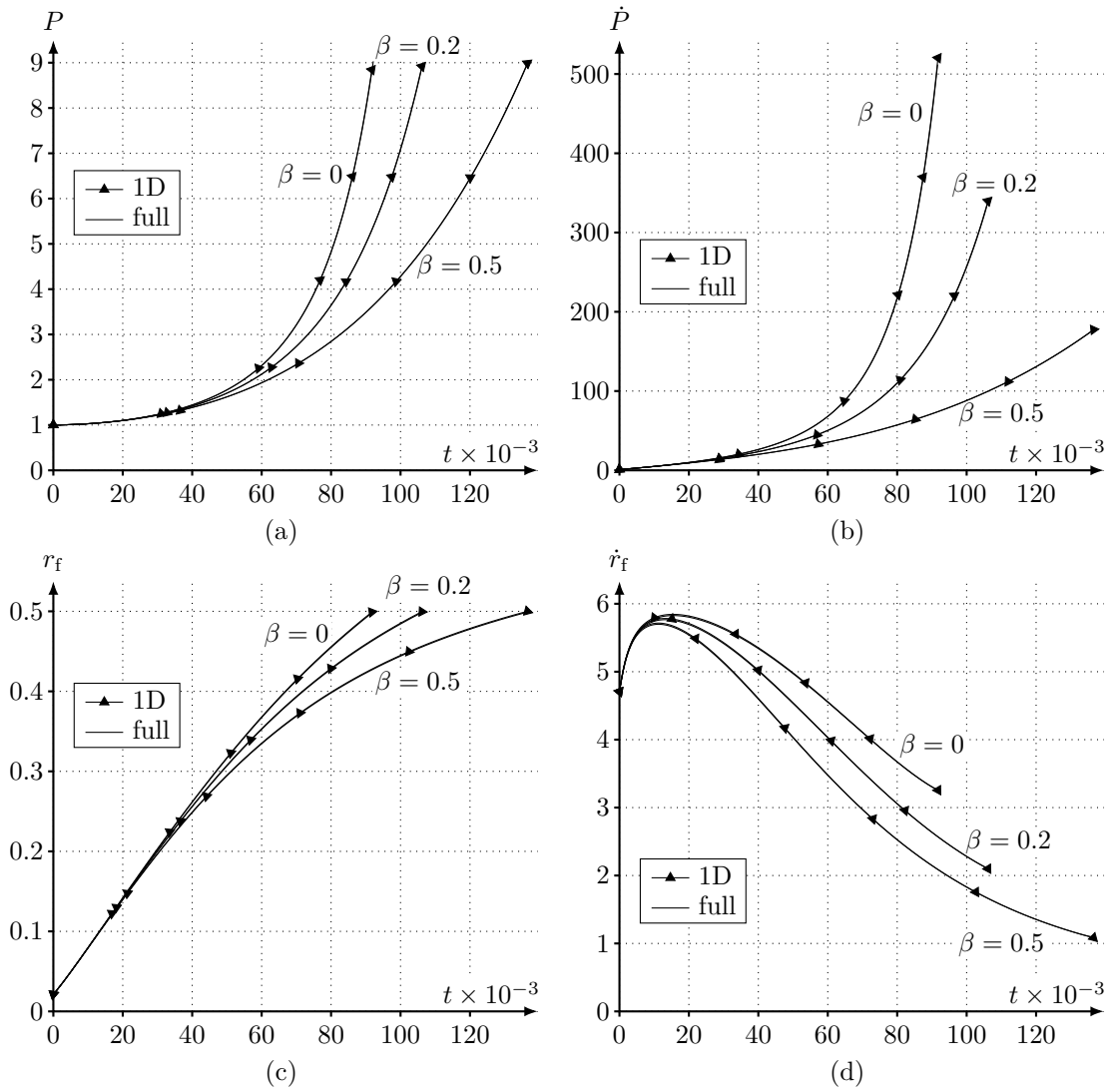


Figure 6.5.: Comparison of the (a) pressure, (b) pressure-rise, (c) radius and (d) flame speed-time curves of the full simulation and the one-dimensional model for an infinitely long cylinder with centric ignition. The corresponding curves coincide.

6. Verification

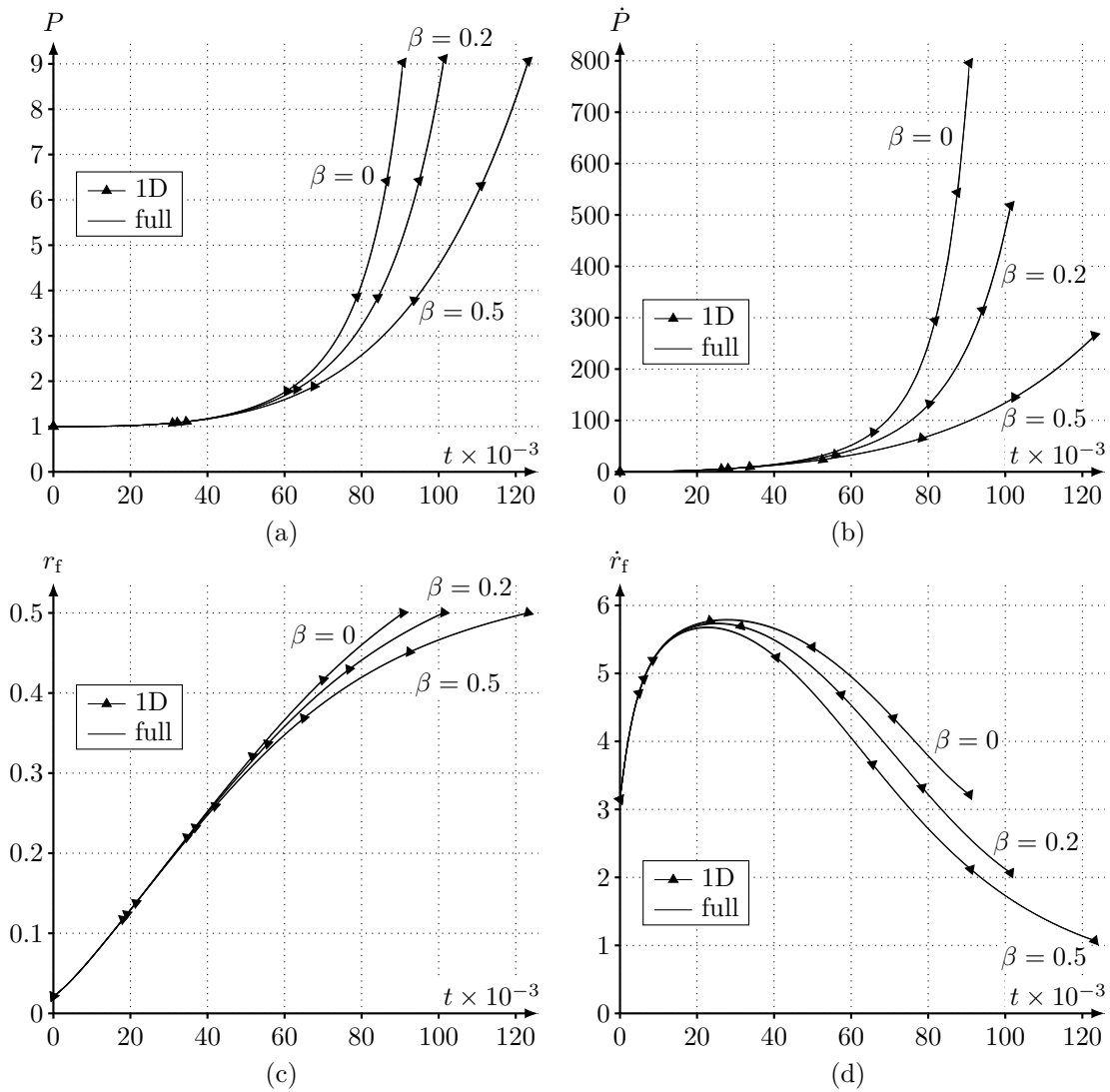


Figure 6.6.: Comparison of the (a) pressure, (b) pressure-rise, (c) radius and (d) flame speed-time curves of the full simulation and the one-dimensional model for a sphere with centric ignition. The corresponding curves coincide.

6.3. Comparison with Channel Flow

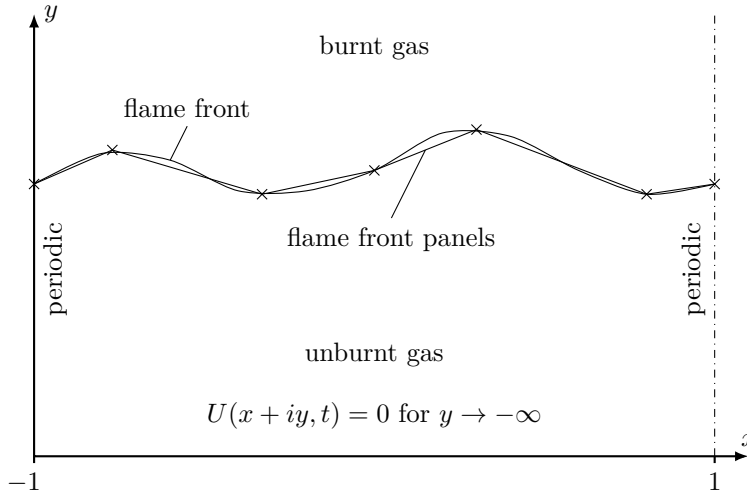


Figure 6.7.: Unconfined combustion: the flame front in a periodic channel. It moves towards the bottom into quiescent, unburnt gas [69, Fig. 5].

A simplified model is used to verify the implementation of the flame front tracking. Unconfined, planar, laminar combustion inside a channel of width 2 is assumed. At the walls at $x = -1$ and $x = 1$, periodic boundary conditions are prescribed, e.g. $\mathbf{u}(x = 2, y) = \mathbf{u}(x = 0, y)$. Since the pressure and the density are in leading order spatially uniform, the vorticity is not considered. The goal is to verify the range of stable and unstable perturbation modes as described in Section 2.4.

The flame front is assumed to be periodic in the x direction, and moves in the negative y direction into quiescent, unburnt gas, as shown in Fig. 6.7. To account for the periodic boundary conditions, the method of mirrored panels has been applied to get the fundamental solution for the velocity induced by a single panel [95]. The following parameters were used in the simulations: $\Delta t = 10^{-5}$, $S_t = 0.0416$, $\sigma = 6$, $\gamma = 1.4$, $\alpha_{\min} = 120^\circ$, $l_{\text{avg}} = 5 \times 10^{-3}$ and $N_f = 400$. Note, that the number of flame front panels changes with time.

The critical wavenumber is $k_c = 10$. This implies that all disturbances with a higher wavenumber, $k > k_c$, are stable and damped, and all disturbances with a lower wavenumber, $k < k_c$ are unstable and amplified.

To test the front tracking algorithm, an initially sinusoidal flame front is chosen, $t = 0$. In Fig. 6.8a, the initial wavenumber is $k_i = 9 < k_c$. Thus, this mode should be amplified according to linear stability analysis. In Fig. 6.8b, the initial wavenumber is $k_i = 11 > k_c$, which should result in a damping of this mode.

As shown in Fig. 6.8, the front tracking algorithm can reproduce the results from the linear stability analysis. For $t = 0.2$, the amplitude of the initial sine function grows the corresponding mode is unstable (Fig. 6.8a), and the sine function is damped when the corresponding mode is stable (Fig. 6.8b).

However, there are more unstable, low wave number instabilities which eventually develop, as can be seen for times $t > 0.4$. When comparing the results obtained from this simple

6. Verification

implementation to a level-set implementation, good agreement is found [66]. However, the method presented here has simulation times of only a few minutes, whereas other numerical implementations take much longer.

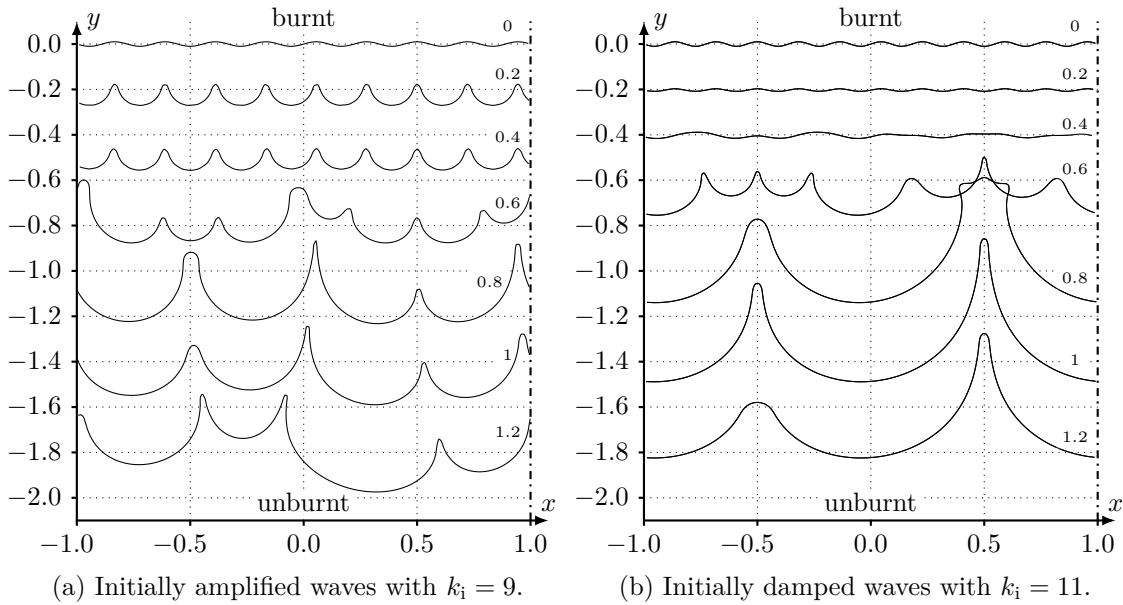


Figure 6.8.: Verification of the flame front tracking algorithm: The initial wavenumber at time $t = 0$ of the disturbance is (a) below and (b) above the critical wavenumber $k_c = 10$.

7. Results & Discussion

In this chapter, selected results obtained with the presented simulation framework are shown. Input data for the simulations are the vessel wall points, numerical and material parameters. For each recorded time step, the results from each simulation include the position of the flame front, the leading-order pressure and position, velocity, entropy and vorticity of the moving mesh points.

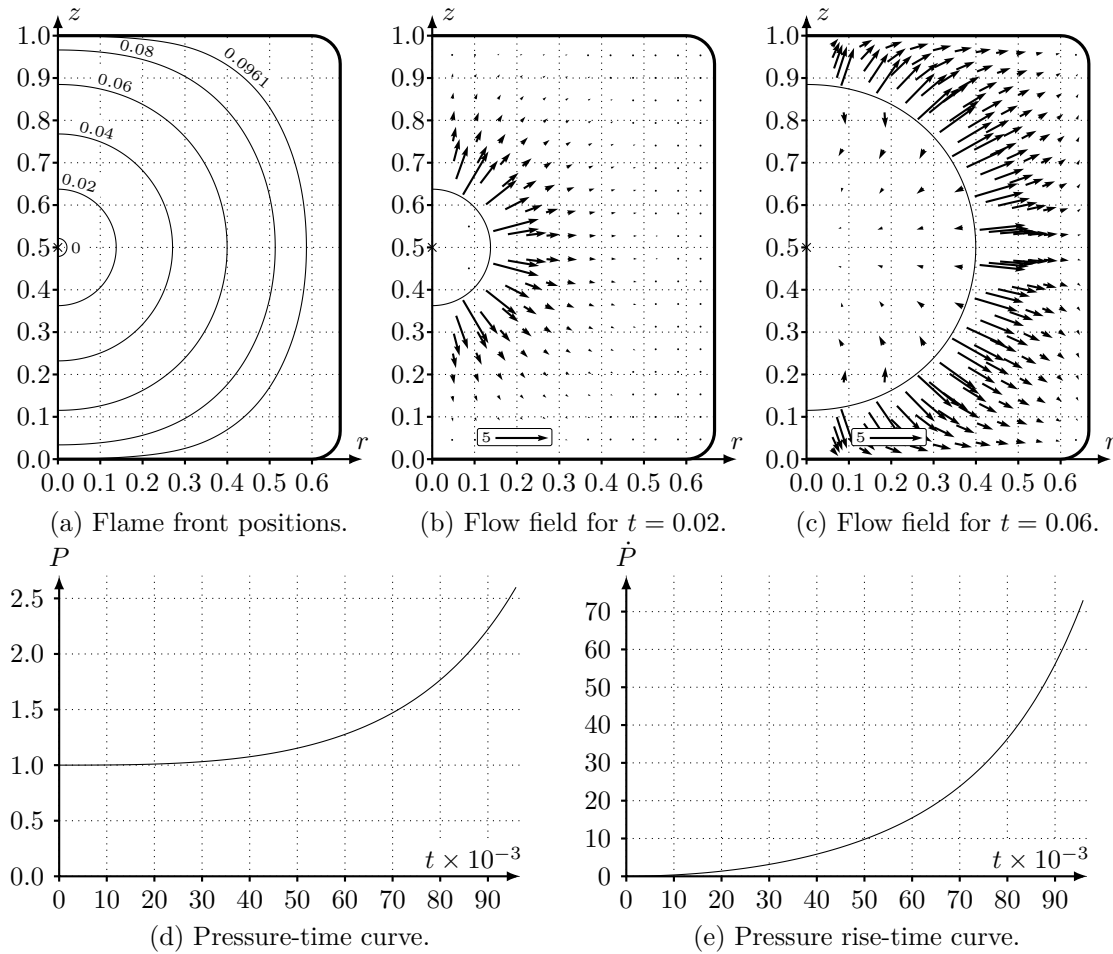


Figure 7.1.: Visualisation of the results of a simulation of an explosion with centric ignition inside a cylinder with an aspect ratio of 0.75. (a) The position of the flame front is drawn for different times. The flow field inside the vessel for (b) $t = 0.02$ and (c) $t = 0.06$ is shown. (d) The pressure-time and (d) pressure rise-time curve are plotted.

An overview of the obtained results is given in Fig. 7.1. The flame front position is drawn with a thin line, whereas the vessel wall is illustrated with a thick line, as seen Fig. 7.1a.

7. Results & Discussion

A cross marks the initial explosion location on the dash-dotted symmetry axis. In the example, the ignition is in the centre of the cylinder. The time step between two flame front curves is constant for each figure. Here, it is $\Delta t = 0.2$. Additionally, the front position of the last recorded time step, i.e. the time where the flame front touches the wall, is given.

The flow field is shown in Figs. 7.1b and 7.1c for two different times $t = 0.02$ and $t = 0.06$, respectively. The velocity field is evaluated at the moving mesh points. Thus, the position of the velocity arrows changes with time, as seen when comparing Figs. 7.1b and 7.1c. The arrow inside the box in the lower part of the figure shows the non-dimensional velocity scaling.

Main result for industrial application is the pressure-time curve, as shown in Fig. 7.1d. In this example, the flame front touches the vessel wall when the pressure is about $P \approx 2.6$. The pressure rise-time curve is shown in Fig. 7.1e. It is relevant for calculating the deflagration index.

Generally, one three-dimensional simulation takes about 2 h to 5 h on a 32-core workstation. The program makes extensive use of parallelisation techniques [96] to fully exploit the multi-core CPU and uses very little main memory. The run time strongly depends on the geometry of the vessel, the computer hardware and the chosen material and numerical parameters. It also depends on the location of ignition: Since the simulation stops once the flame front touches the wall, an off-centric ignition often leads to a shorter simulation time.

The chapter is structured as follows: The first section contains results which highlight the features and advantages of this model and implementation. The most important factors which influence the explosion process are shown. Comparing the pressure-time curves of the 1D model to the full model shows no significant differences when the volume of the vessels are the same. In the second section, comparison of experimental data with simulation results are given. In total, eleven different pressure-time curves of real dust explosions are compared.

7.1. Flame-flow Interaction

Since the flame front has an impact on the velocity field, and vice versa, different effects which change the explosion process can be identified. Among those, the shape of the vessel, the ignition location and the reaction enthalpy are shown in this section. If not noted differently, the following parameters were used in the simulations of this section: $\gamma = 1.4$, $\Delta h_f = 20$, $\beta = 0.2$, $\Delta = 0.05$, $\Delta t = 5 \times 10^{-6}$, 150 flame front panels and 820 vessel wall panels.

When changing the initial location of the explosion, a couple of different things happen: First, an off-centric ignition leads to a different contact time. The contact time is the time when the flame front first touches the vessel wall and the simulation stops. The change of the initial location of explosion can result in a later contact time, as shown in Fig. 7.3. Here, the contact time decreases from $t_e = 0.092$ to $t_e = 0.0615$. This happens for all cylindrical vessels. When the vessel shape is more complex, an ignition closer to the centre can lead to a smaller contact time, as shown when comparing Fig. 7.9a to Fig. 7.9b.

7. Results & Discussion

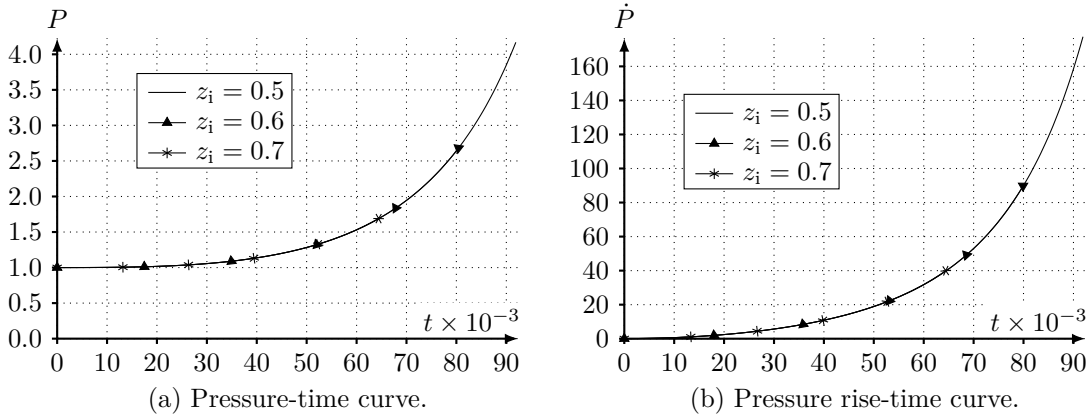


Figure 7.2.: Influence of the initial explosion location z_i on the pressure-time and pressure rise-time curves in a cylinder. The curves almost perfectly coincide.

Here, the contact time increases from $t_e = 0.0436$ to $t_e = 0.0504$. Centric ignition is defined as ignition in the middle of the symmetry axis $z_i = 0.5$.

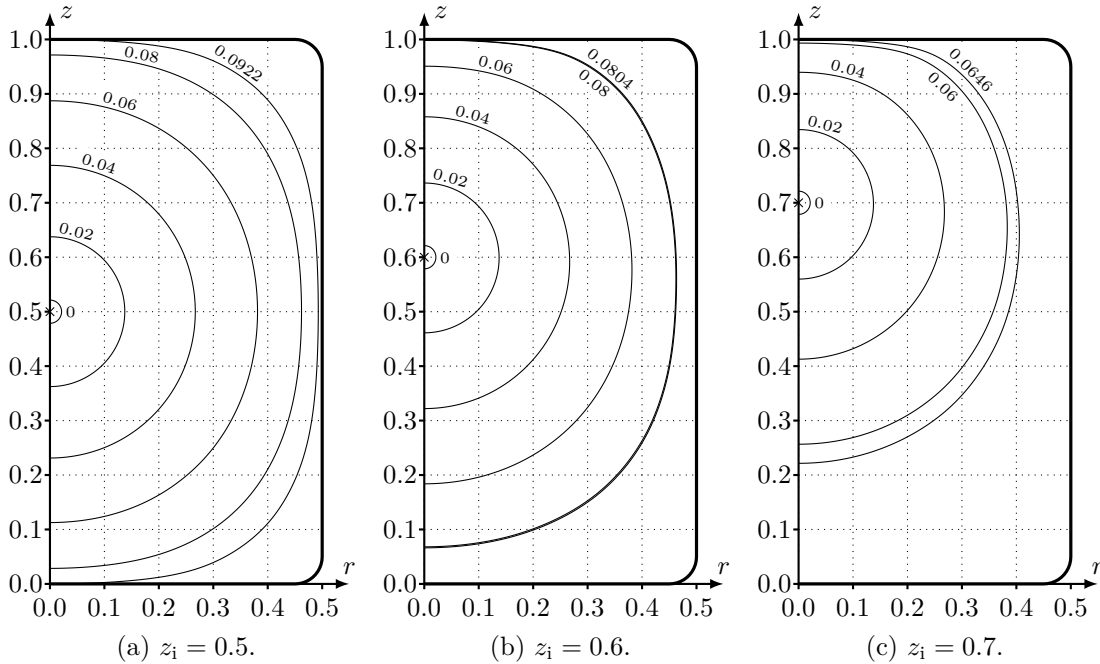


Figure 7.3.: Influence of the initial explosion location z_i on the flame front in a cylinder. The position of the flame front is shown for different times.

For cylindrical vessels, ignition off the centre of the symmetry axis also results in a loss of symmetry about $z = 0.5$, as shown when comparing Figs. 7.11e and 7.11f with Fig. 7.11d. This also implies a flame front which deviates significantly from a spherical shape at the end stage of the explosion, as shown in Fig. 7.3c. However, in the early process of an explosion, the influence of the vessel boundaries on the shape of the flame front is not very pronounced. This leads to an almost spherical flame front and symmetric flow field even for very off-centric ignition locations, see Fig. 7.11c. Also, the speed of the gas in the

7. Results & Discussion

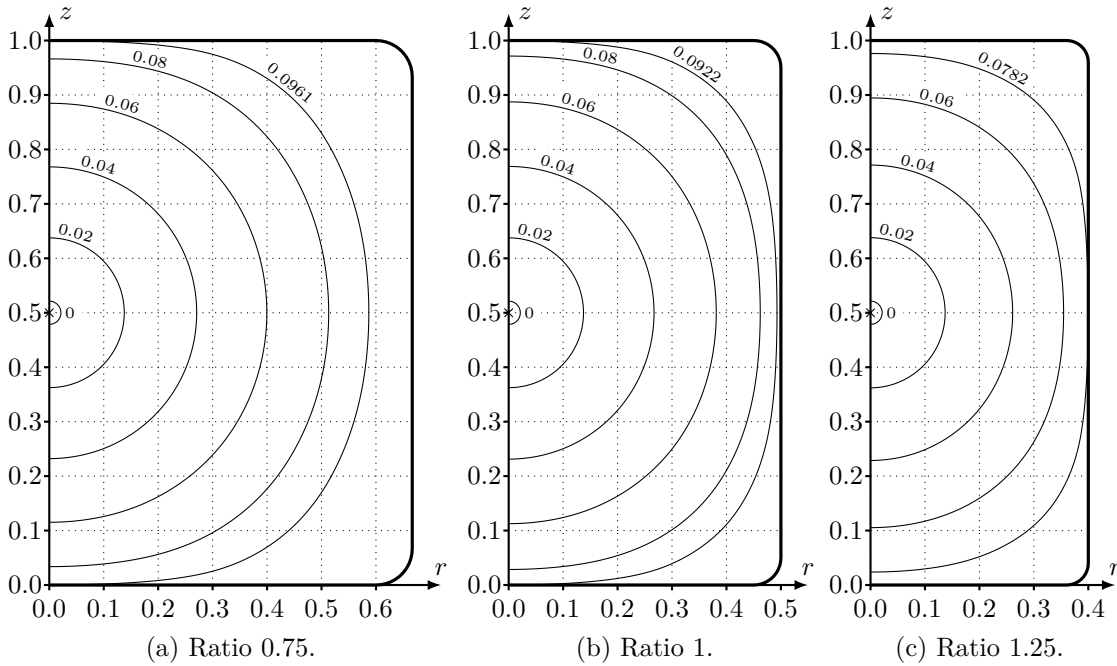


Figure 7.4.: Influence of the aspect ratio of a cylindrical vessel on the shape of the flame. The position of the flame front is shown for different times.

vicinity of the vessel wall is very low, cf. Figs. 7.11a, 7.11b and 7.11c.

Although the flow field is strongly influenced by the location of ignition, the pressure-time and pressure rise-time curves almost perfectly coincide, as shown in Fig. 7.2. The only notable difference is the pressure when the flame front touches the wall: It is much larger for centric ignition since the simulation stops later.

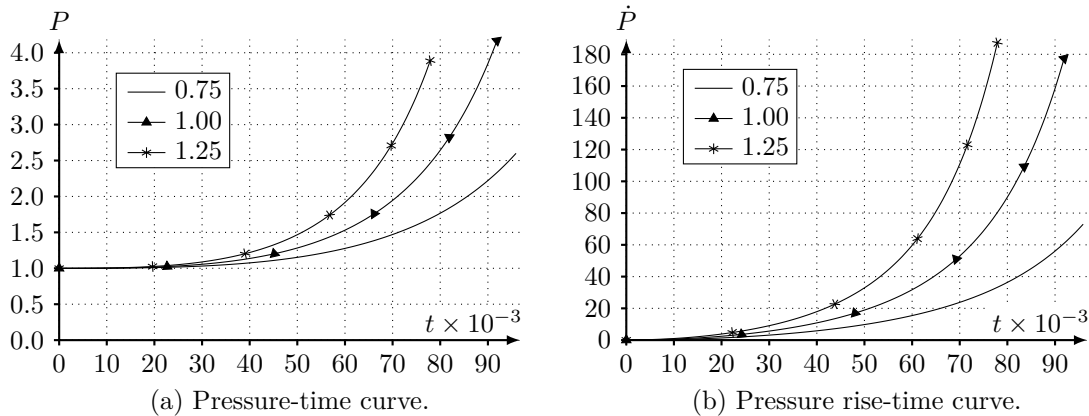


Figure 7.5.: Influence of the aspect ratio of a cylindrical vessel on the pressure-time and pressure rise-time curves.

The impact of the aspect ratio, i.e. the ratio of the height to diameter, of a cylindrical vessel on the shape of the flame front is shown in Fig. 7.4. Fig. 7.12 is an overlay of all vessel shapes and flame fronts of Fig. 7.4. Three different aspect ratios, 0.75, 1 and 1.25, were chosen, and ignition is always in the centre of the vessel.

7. Results & Discussion

As before, the flame front remains spherical during the first stages of the combustion process and is almost independent of the vessel shape, see e.g. time $t = 0.02$. For a vessel with a larger aspect ratio, the flame front touches the sidewalls first, Fig. 7.4c, whereas for cylinders with lower aspect ratios, the top walls are reached first, Figs. 7.4a and 7.4b. Up until about $t \approx 0.04$, no significant difference of the flame fronts between the three different vessels is seen, Fig. 7.12.

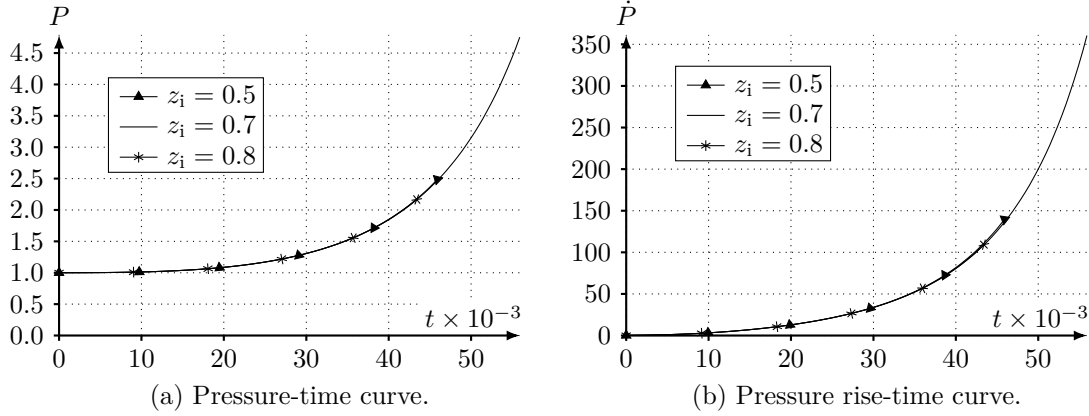


Figure 7.6.: Influence of the initial explosion location z_i on the pressure-time and pressure rise-time curves in a complex geometry. The curves almost perfectly coincide.

The velocity field, shown in Fig. 7.13, changes quantitatively for cylindrical vessel with different aspect ratios. For earlier times, $t = 0.02$, the speed of the fluid in the unburnt gas near the flame front is higher for vessels with a lower aspect ratio, e.g. for an aspect ratio of 0.75, see Fig. 7.13a, compared to the other two vessel shapes, Figs. 7.13b and 7.13c. Since ignition is at the centre, the flow field shows an additional symmetry about $z = 0.5$. For later stages, the flow field inside the vessels with the largest aspect ratio is influenced mostly by the side walls of the vessel, Fig. 7.13f. The velocity field of the other two vessels is more influenced by the top and bottom walls, Figs. 7.13d and 7.13e.

The pressure-time and pressure rise-time curves are significantly different when the aspect ratio of the vessel changes, as shown in Fig. 7.5. For an aspect ratio of 0.75, the flame front touches the vessel wall last, at $t = 0.0959$. However, the final pressure is lower than the one from more elongated vessels. This is due to the higher mass fraction of unburnt gas. The highest final pressure is reached when the aspect ratio is unity. Interestingly, the highest pressure rise is obtained in the most elongated vessel. This can be explained with the higher surface of the flame front, since the pressure change is directly proportional to it.

To show the capabilities of the newly developed method, a non-cylindrical vessel was simulated. The geometry is cylindrical on the top, and has a cone at the bottom. It could be a dust collector. When the initial explosion location is varied, the flame front touches the vessel wall at different times, as shown in Fig. 7.9. However, due to the more complex geometry, a centric ignition, Fig. 7.9a, does not necessarily imply a longer simulated time. Here, the contact time for one eccentric ignition is $t_e = 0.0504$, see Fig. 7.9b, compared to $t_e = 0.0436$ for centric ignition. Even when the location of ignition is chosen very close to the vessel wall, the flame front remains spherical up until $t \approx 0.02$, cf. Fig. 7.9c.

The velocity field for two different times is shown in Fig. 7.14. For $t = 0.02$, the flame

7. Results & Discussion

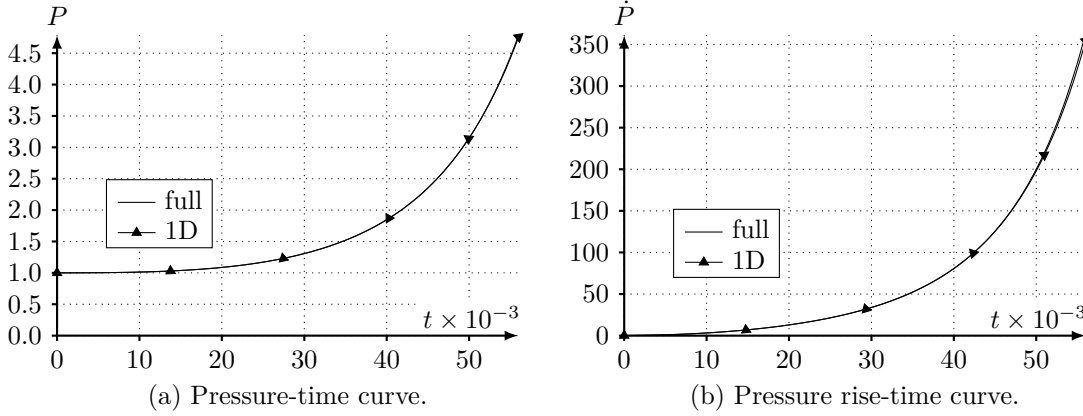


Figure 7.7.: Comparison of the pressure-time and pressure rise-time curves of the full and one-dimensional model in the complex geometry with $z_i = 0.2$. The one-dimensional model assumes a sphere which has the same volume as the geometry of the full model. The curves almost perfectly coincide.

front is close to the vessel wall for two cases, Figs. 7.14a and 7.14c. However, the influence of the vessel boundaries is still rather small, which results in an almost spherical flame front and a vanishing velocity field in the vicinity of the walls. For later times, the flame front gets closer to the walls, and eventually becomes more distorted, Fig. 7.14d.

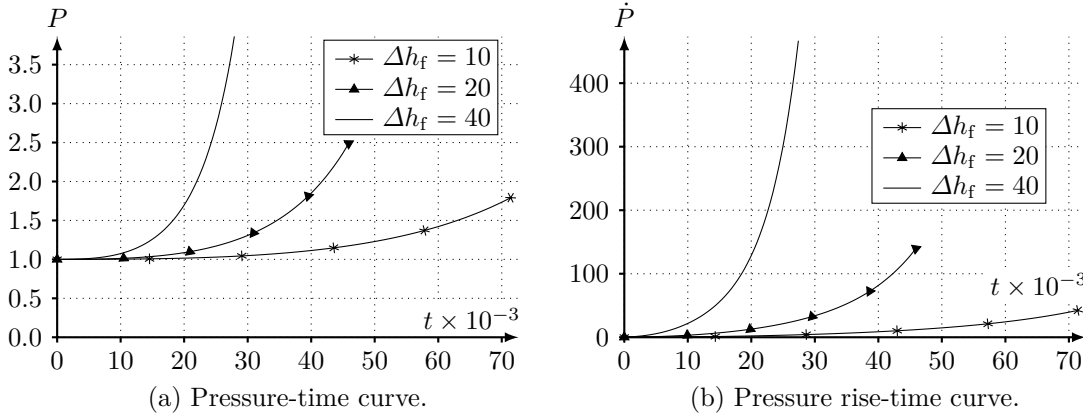


Figure 7.8.: Influence of reaction enthalpy Δh_f on the pressure-time and pressure rise-time curves in a complex geometry.

The pressure-time and pressure rise-time curves for different ignition locations almost coincide, see Fig. 7.6. The same trend as for cylindrical vessels is observed: The only difference is the final pressure before the simulation stops.

The comparison of the full and one-dimensional model shows almost no impact on the pressure-time and pressure rise-time curves, see Fig. 7.7. The one-dimensional simulation was done with a sphere which has the same volume as the complex geometry. This result is remarkable, since the geometry is not very well approximated by a sphere, and the flame front deviates significantly from a spherical shape.

A larger reaction enthalpy Δh_f results in a higher end pressure p_e . Additionally, the explosion is much more violent and faster. Three different values of Δh_f , 10, 20 and 40,

7. Results & Discussion

were studied. The flame front moves much faster when the reaction enthalpy is larger, as shown in Fig. 7.10. Note, that time between two consecutive flame front positions is not equal for the three cases ($\Delta h_f = 10$: $\Delta t = 0.02$, $\Delta h_f = 20$: $\Delta t = 0.01$, $\Delta h_f = 40$: $\Delta t = 0.005$). Also, the hydrodynamical instability is more pronounced for a larger reaction enthalpy. This manifests itself in the slightly buckled flame shape during the later stages of the explosion for $\Delta h_f = 40$ (Fig. 7.10c).

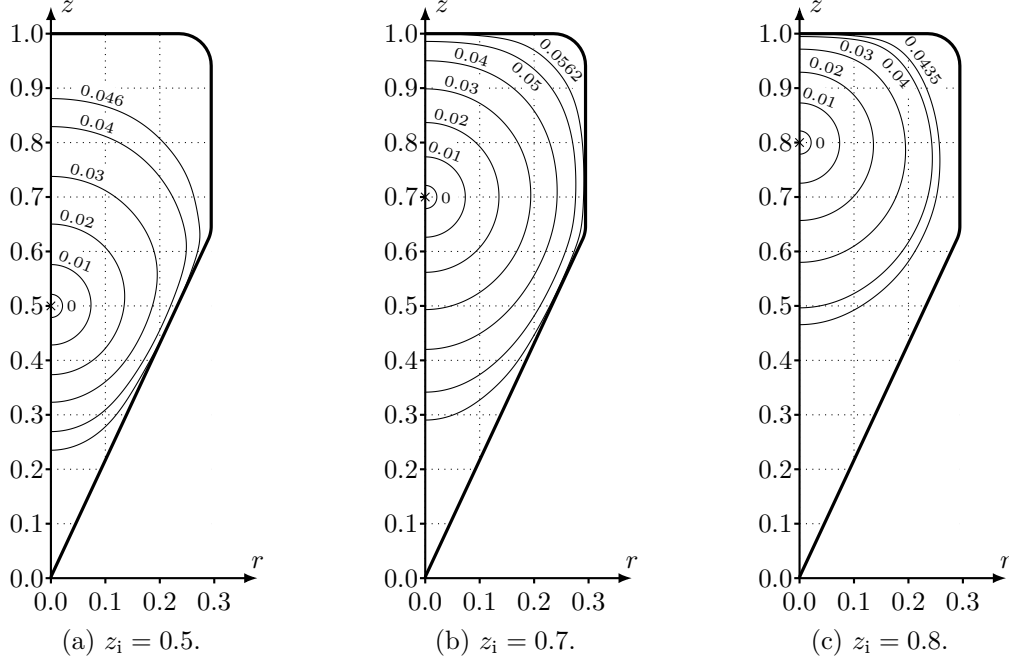


Figure 7.9.: Influence of the initial explosion location z_i on the shape of the flame front in a more complex geometry. The position of the flame front is shown for different times

As expected, a larger reaction enthalpy yields a higher final pressure, and a higher pressure rise, as shown in Fig. 7.8. The flow field for $\Delta h_f = 10$ is almost non-existent (Figs. 7.15a and 7.15d), compared to $\Delta h_f = 20$ (Figs. 7.15b and 7.15e) and $\Delta h_f = 40$ (Fig. 7.15c and 7.15f). This also explains why for a higher reaction enthalpy, the flame front adapts much more to the vessel wall: Imagine a vanishing reaction enthalpy $\Delta h_f \rightarrow 0$. Then, there would be no flow field at all, and the flame front would just be transported passively through quiescent gas. This also implies that it would remain perfectly spherical, since there is no influence of the vessel boundaries. Contrary, a very high reaction enthalpy yields much higher speeds. This results in a more pronounced influence of the vessel wall on the flow field, resulting in a more distorted flame front. Thus, the flame adapts more to the shape of the vessel when Δh_f is increased.

7. Results & Discussion

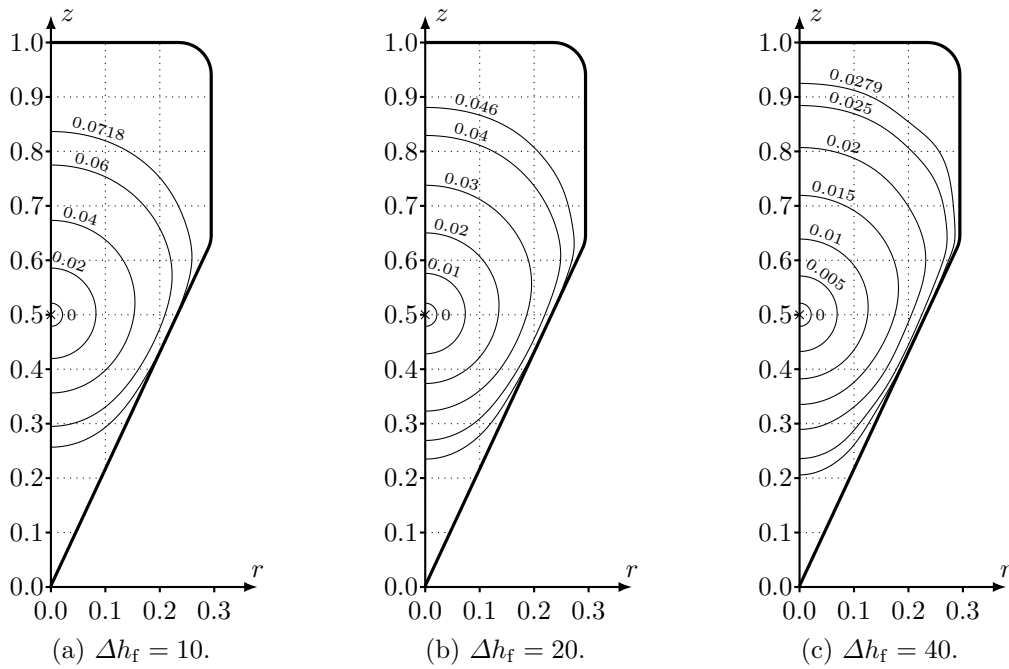


Figure 7.10.: Influence of the reaction enthalpy Δh_f on the shape of the flame front in a more complex geometry. The position of the flame front is shown for different times.

7. Results & Discussion

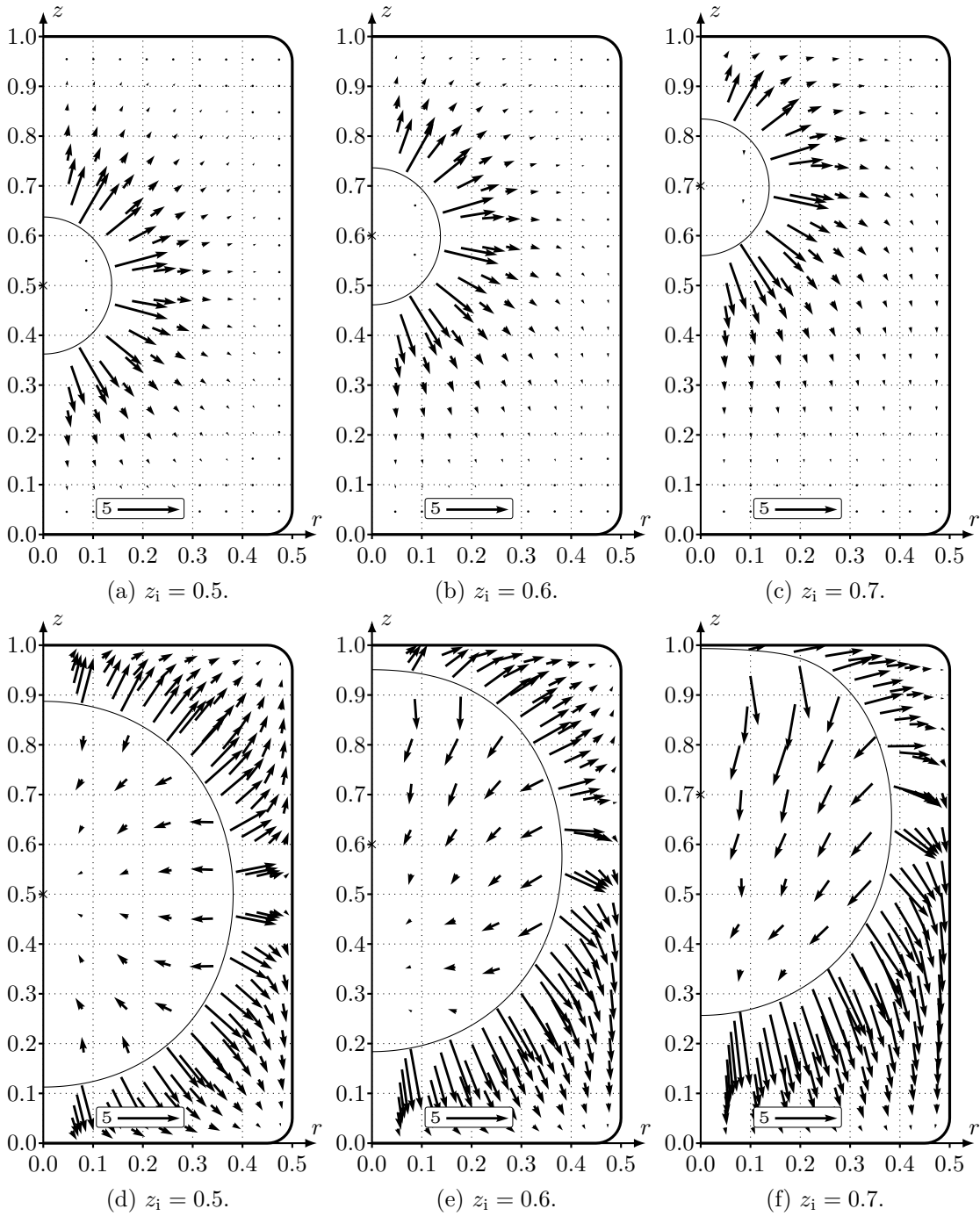


Figure 7.11.: Influence of the initial explosion location z_i on the flow field for $t = 0.02$ (top) and $t = 0.06$ (bottom) in a cylinder.

7. Results & Discussion

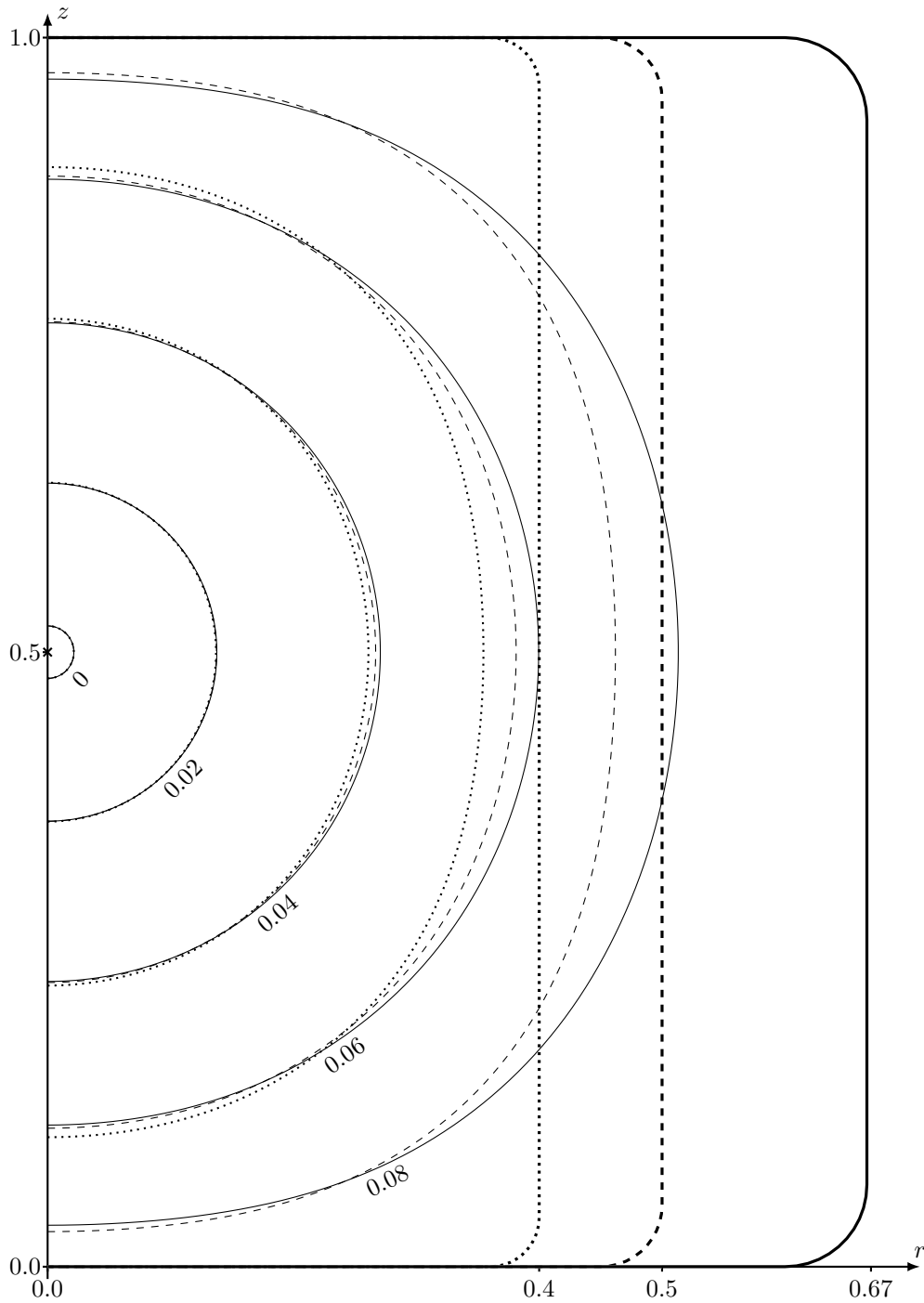


Figure 7.12.: Overlay of flame front positions for three different cylindrical vessels. All solid lines correspond to the vessel with an aspect ratio of 0.75, all dashed lines belong to the vessel with an aspect ratio of 1 and all dotted lines indicate a vessel with an aspect ratio of 1.25.

7. Results & Discussion

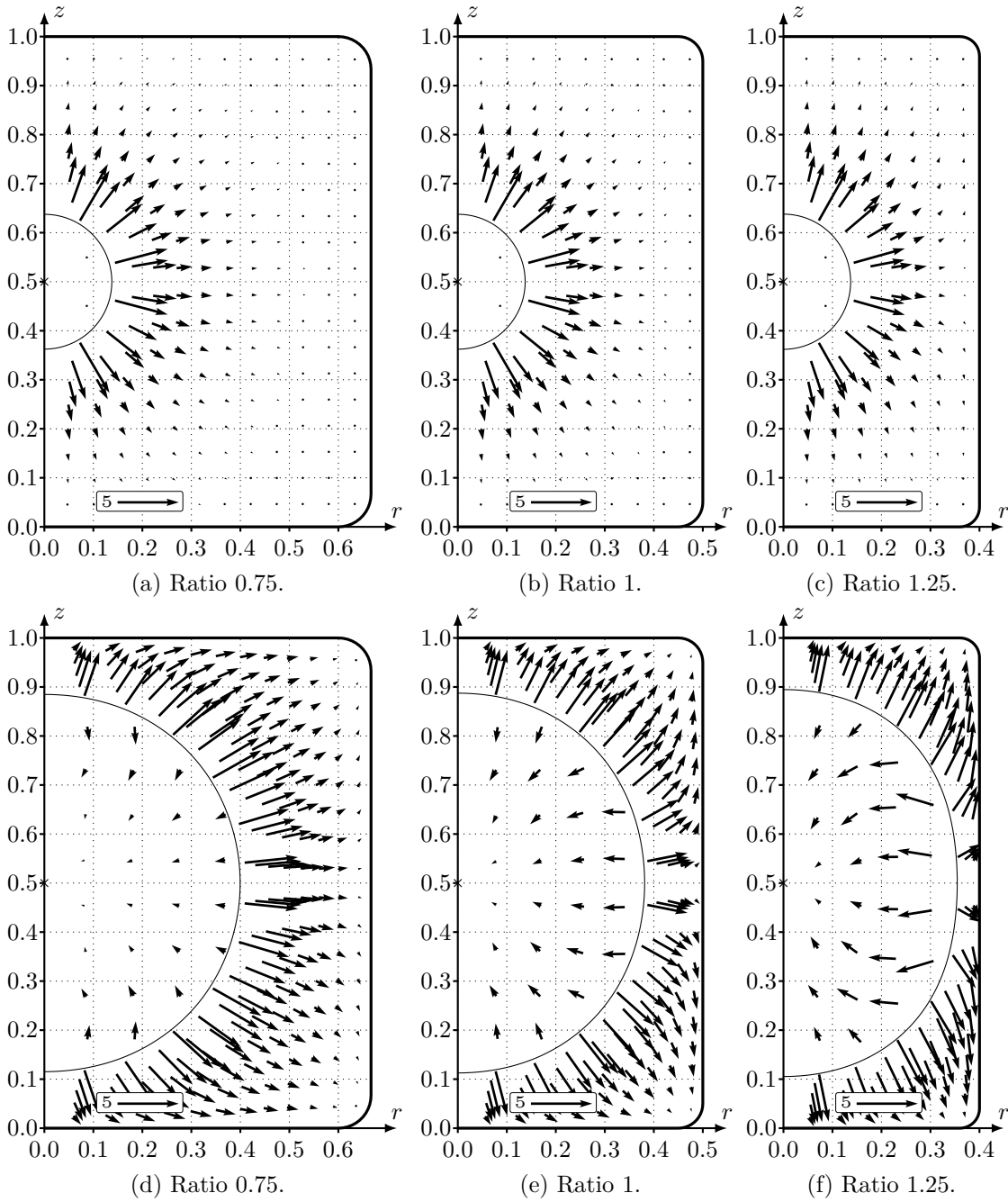


Figure 7.13.: Influence of the aspect ratio of a cylindrical vessel on the flow field for $t = 0.02$ (top) and $t = 0.06$ (bottom).

7. Results & Discussion

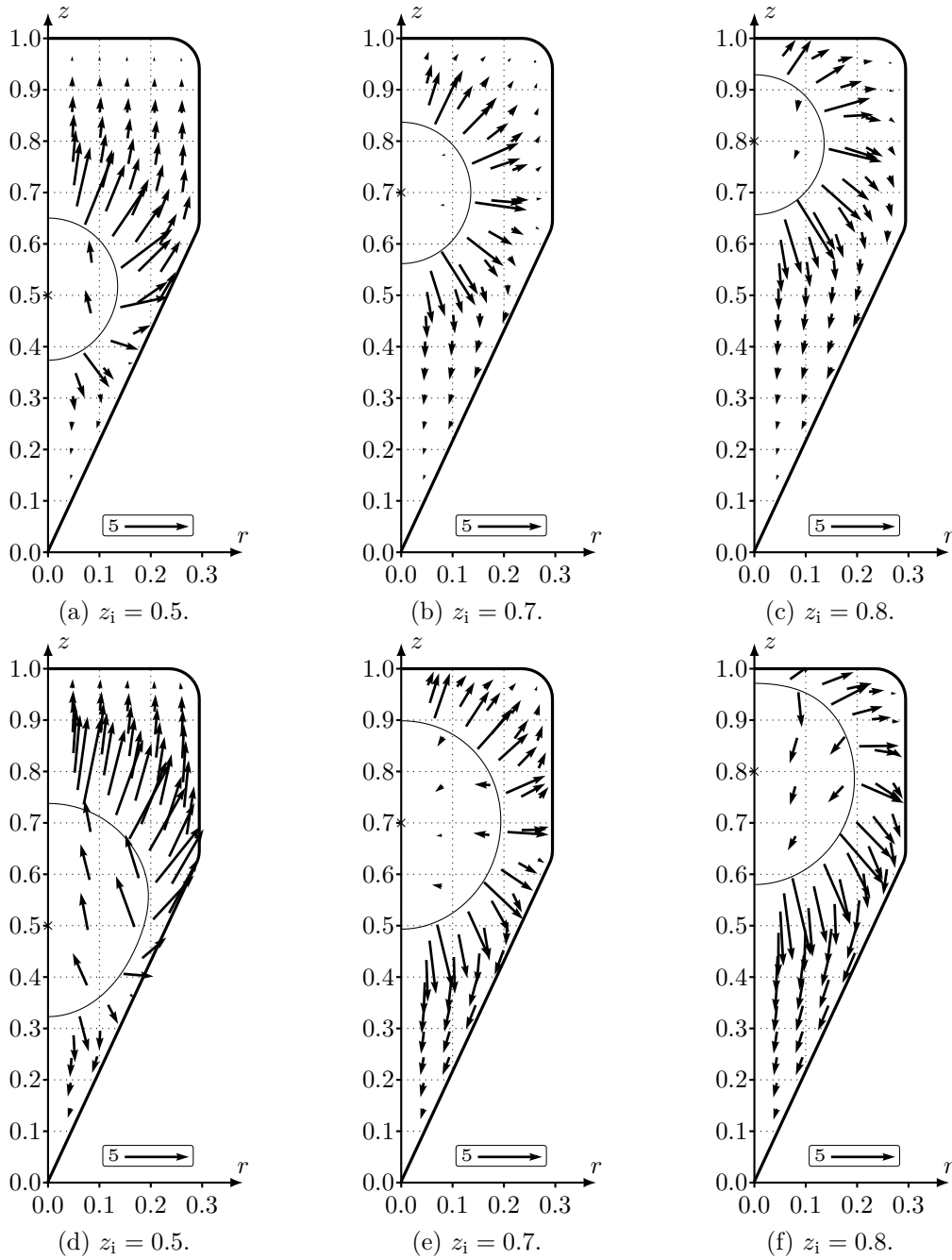


Figure 7.14.: Influence of the initial explosion location z_i on the flow field for $t = 0.02$ (top) and $t = 0.03$ (bottom) in a complex geometry.

7. Results & Discussion

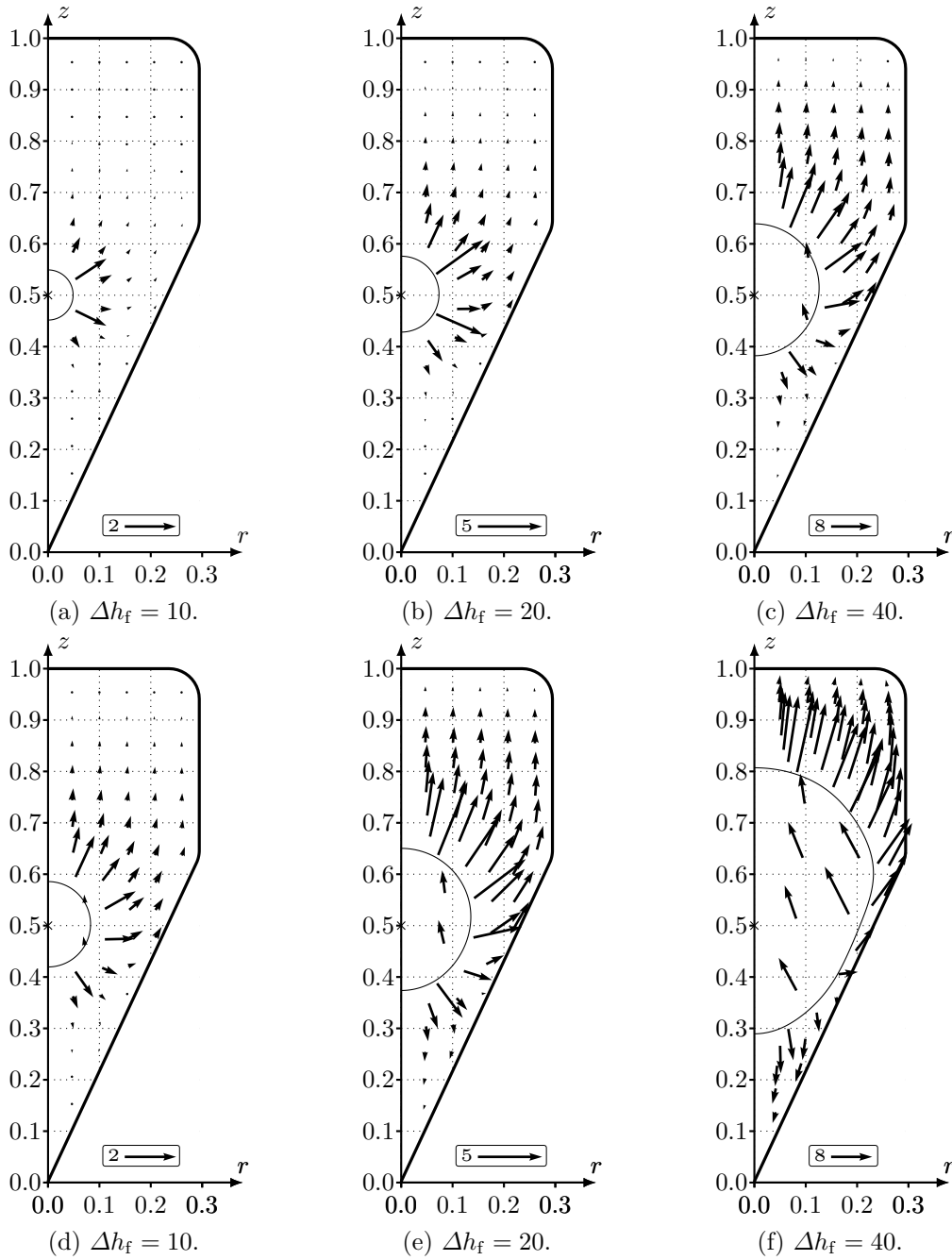


Figure 7.15.: Influence of the reaction enthalpy Δh_f on the flow field for $t = 0.01$ (top) and $t = 0.02$ (bottom) in a complex geometry. Note, that the velocity arrows are scaled differently from left to right.

7.2. Comparison with Experiments

Data from eleven different experiments, conducted in three different vessels, are available [97]. The experiments were done by IEP Technologies in Germany. All vessels are cylinders with an aspect ratio of one and rounded top and bottom edges. The vessel walls were not insulated. An overview over all experiments is given in Tab. 7.1. The dust inside the vessel was a standard test dust. The deflagration index was varied by changing the ignition delay. The ignition delay is the time interval between dispersion of the dust particles and the actual ignition. It is known from experiments [98, 99] that a larger ignition delay time leads to a less violent explosion, since the initial turbulence induced by the injection of the dust particles decays over time [100]. Thus, a longer ignition delay leads to lower values of \tilde{K}_{St} .

Table 7.1.: List of experiments [97] and simulation parameters.

name	\tilde{K}_{St}	\tilde{V}_v	\tilde{p}_e/\tilde{p}_i	Δh_f	\tilde{s}_{eff}^0	$p-t$ curve
A16	248 bar m/s	1 m ³	9.5	39.2	1.30 m/s	Fig. 7.18
A19	161 bar m/s	1 m ³	9.2	37.7	1.00 m/s	Fig. 7.19
A21	67 bar m/s	1 m ³	8.5	34.5	0.55 m/s	Fig. 7.20
D1	260 bar m/s	5 m ³	9.3	38.2	1.45 m/s	Fig. 7.21
D2	265 bar m/s	5 m ³	9.1	37.3	1.55 m/s	Fig. 7.22
D4	178 bar m/s	5 m ³	8.9	36.4	1.03 m/s	Fig. 7.23
D5	62 bar m/s	5 m ³	8.3	33.6	0.42 m/s	Fig. 7.24
C2	249 bar m/s	10 m ³	8.8	35.9	1.33 m/s	Fig. 7.25
C3	236 bar m/s	10 m ³	9.2	37.7	1.26 m/s	Fig. 7.26
C4	161 bar m/s	10 m ³	9.5	39.2	0.91 m/s	Fig. 7.27
C6	96 bar m/s	10 m ³	9.1	37.3	0.62 m/s	Fig. 7.28

Ignition was done with two 5 kJ pyrotechnic ignitors. The pressure was recorded with two piezoelectric pressure measurement chains. The range of reported end pressures was between 8.3 bar to 9.5 bar. The deflagration index was calculated using the isothermal model by Nagy et al., cf. Eq. (4.21), and is between 62 bar m/s to 265 bar m/s, and the volume of the vessels were 1 m³, 5 m³ and 10 m³. Since all vessels are cylindrical with an aspect ratio of one, they are geometrically similar.

For the simulations, material parameters for a corn starch-air mixture were taken from literature, $\gamma = 1.22$ and $\beta = 0.36$ [7]. This set of parameters yields a burning velocity that is almost independent of pressure and temperature. The reaction enthalpy Δh_f was chosen such that the (dimensionless) end pressure p_e after complete combustion of the simulation matches the experimental end pressure. The shape of the vessel was approximated by a cylinder with an aspect ratio of unity and rounded corners, as shown in Fig. 7.16. Thus, the additional flanges which were present on the vessels from the experiments were not considered in the geometry of the simulations. Since the model assumes an adiabatic vessel wall, heat losses to the surroundings during the explosion were not considered in the simulations.

The flame front and vessel wall were discretised with $N_f = 150$ and $N_v = 820$ panels, respectively. The stabilisation number was $S_t = 0.01$, the initial radius $r_i = 0.02$, the time step $\Delta t = 5 \times 10^{-6}$ and the distance between two mesh points $\Delta = 0.05$. Ignition is in the centre of the z axis.

7. Results & Discussion

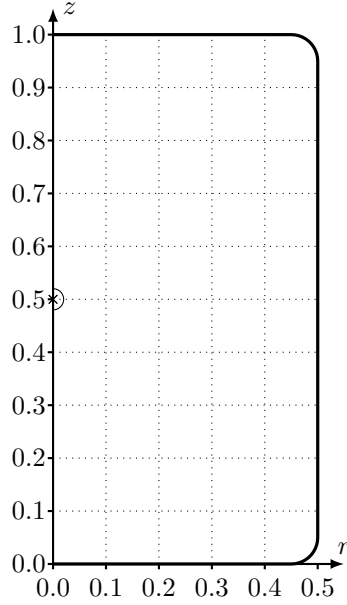


Figure 7.16.: Geometry of the vessel used for the simulations. It has an aspect ratio of one, and the corners are rounded. The explosion starts at the centre, and the initial flame front radius is $r_i = 0.02$.

Result of the experiments are the pressure-time curves. They start at an arbitrary start time $\tilde{t} = -1$ s and end at time $\tilde{t} = 4$ s. Thus, all pressure-time curves in this section are shifted so that the reported ignition time is at a dimensionless time $t = 0$. The pressure is given as gauge pressure, and its unit is bar. The experimental pressure-time curves are shifted by 1 bar, since $\tilde{p}_{\text{ref}} = 1$ bar. Additionally, the experimental data are non-dimensionalised by scaling the time to find the best fit to the simulations. With the available data, it is not possible to predict the experimental pressure-time curves.

It turns out that the shift to the reported ignition time does not suffice for good agreement between simulations and experiments. This can be due to an additional delay between the injection of the ignitors and the actual ignition of the suspended dust cloud. Thus, the pressure-time curves of the simulations are shifted in time. The necessary shift of each sample is chosen such that the final pressure from the simulation lies on the experimental pressure-time curve. The shift t_o of each individual simulation curve is reported in the figure caption. This delay is especially pronounced for experiments no. A16, D1, D2, C3 and C4 (Figs. 7.18, 7.21, 7.22, 7.25, 7.26 and 7.27), where an additional shift of more than $t = 0.04$ has been introduced. For two experiments, A21 and D5, very little delay is found (Figs. 7.20 and 7.24). By shifting the simulation data, excellent agreement between simulations and experiments is achieved.

From the characteristic reference time used to scale the experimental data, the burning velocity at reference conditions \tilde{s}_{eff}^0 can be computed. \tilde{s}_{eff}^0 is in the range of 0.42 m/s to 1.55 m/s. Fig. 7.17 illustrates the dependency of \tilde{s}_{eff}^0 on the deflagration index. It seems like the burning velocity increases linearly with the deflagration index. However, too little experimental data is available to validate this statement.

7. Results & Discussion

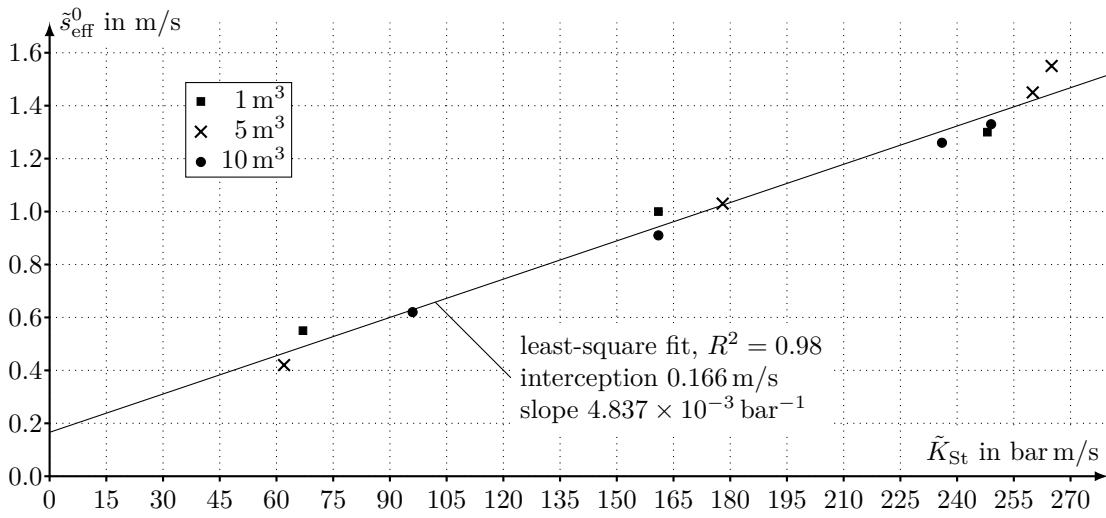


Figure 7.17.: The influence of the deflagration index \tilde{K}_{St} on the burning velocity \tilde{s}_{eff}^0 . The solid line is a least square fit with a coefficient of determination $R^2 = 0.98$.

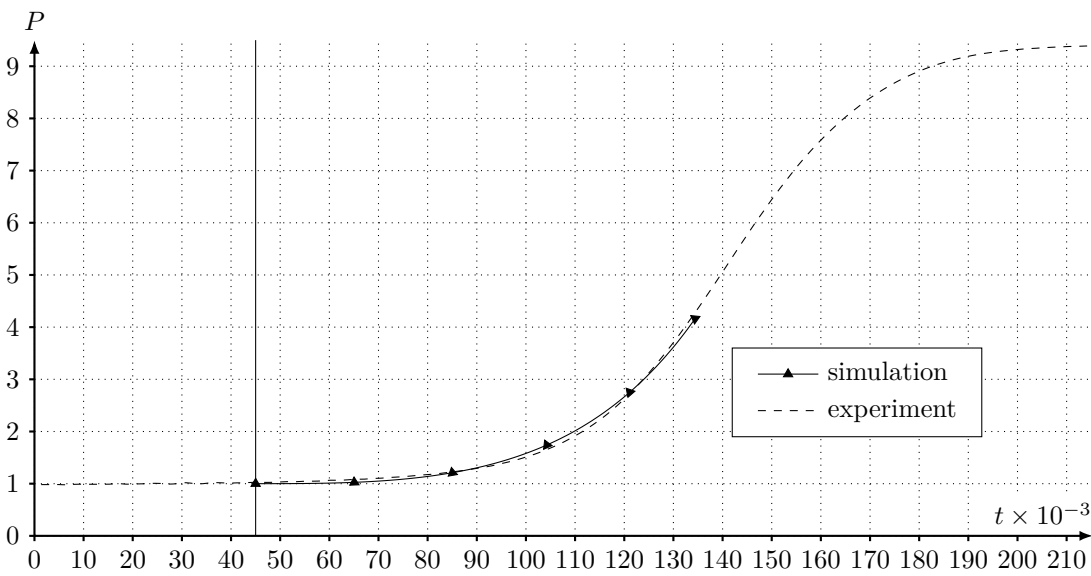


Figure 7.18.: Pressure-time curves of the simulation and experiment no. A16, $1 m^3$ cylinder, $\tilde{K}_{St} = 248 \text{ bar m/s}$, offset $t_o = 0.045$.

7. Results & Discussion

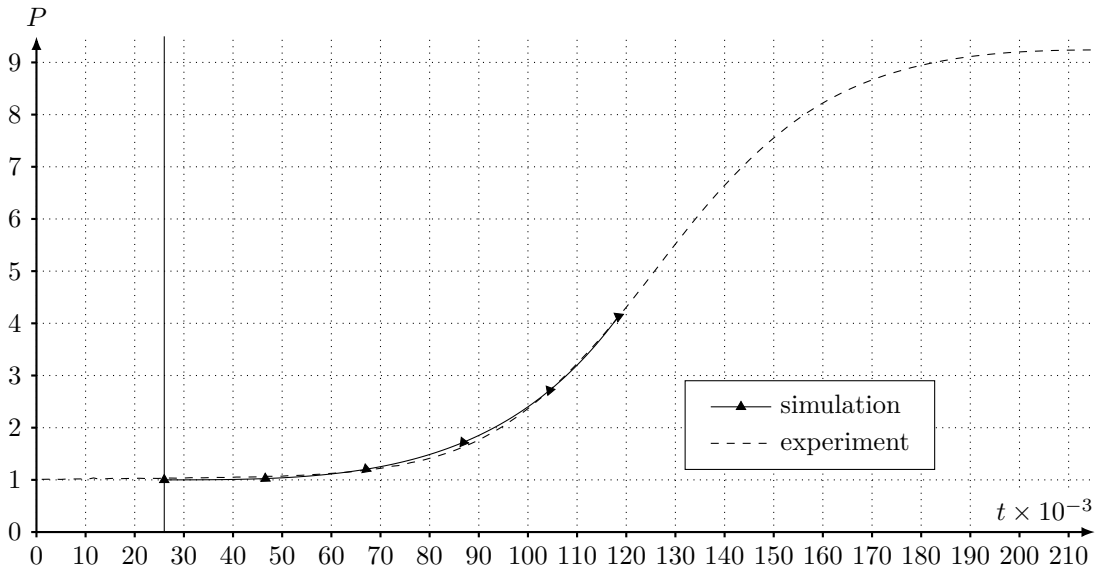


Figure 7.19.: Pressure-time curves of the simulation and experiment no. A19, 1 m^3 cylinder, $\tilde{K}_{\text{St}} = 161 \text{ bar m/s}$, offset $t_o = 0.026$.

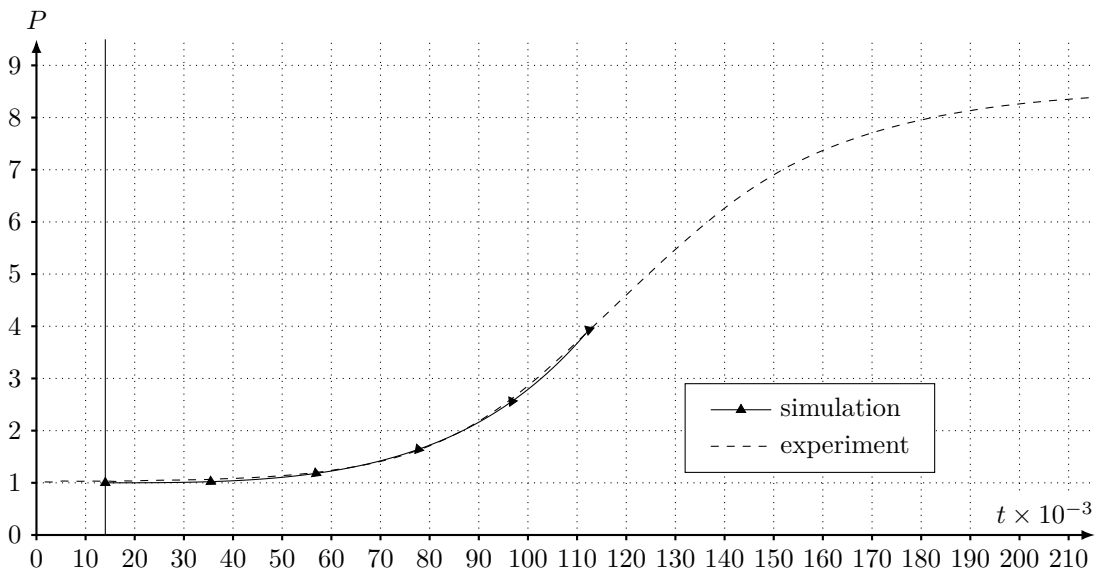


Figure 7.20.: Pressure-time curves of the simulation and experiment no. A21, 1 m^3 cylinder, $\tilde{K}_{\text{St}} = 67 \text{ bar m/s}$, offset $t_o = 0.014$.

7. Results & Discussion

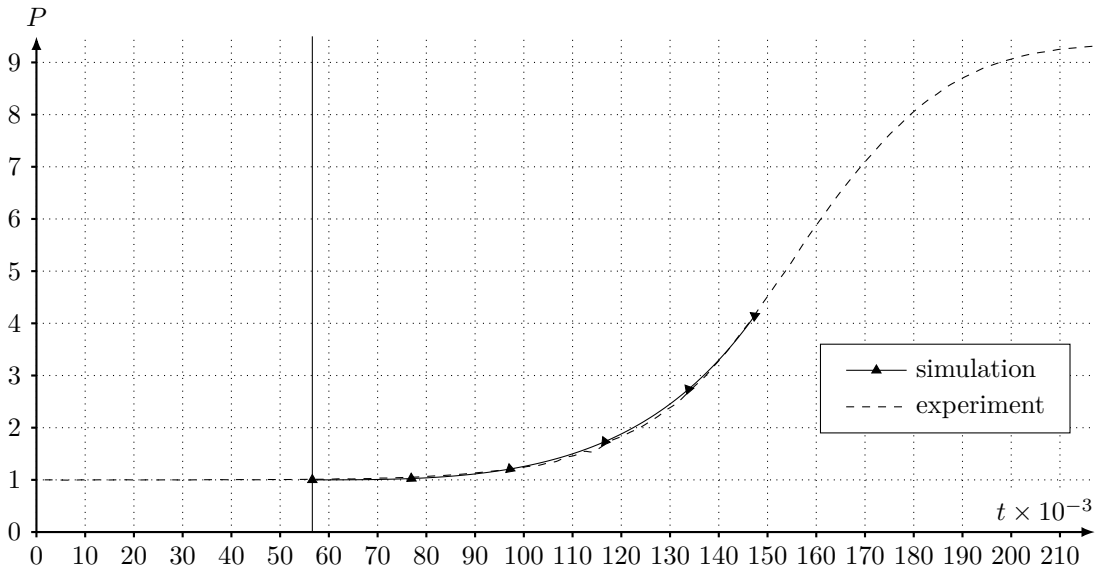


Figure 7.21.: Pressure-time curves of the simulation and experiment no. D1, 5 m³ cylinder, $\tilde{K}_{St} = 260$ bar m/s, offset $t_o = 0.057$.

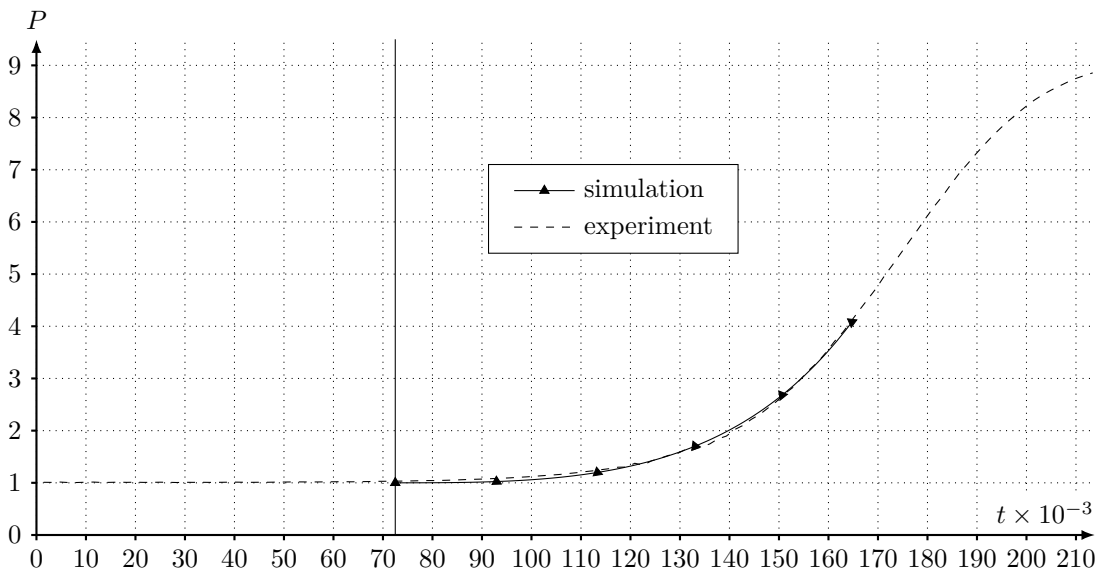


Figure 7.22.: Pressure-time curves of the simulation and experiment no. D2, 5 m³ cylinder, $\tilde{K}_{St} = 265$ bar m/s, offset $t_o = 0.073$.

7. Results & Discussion

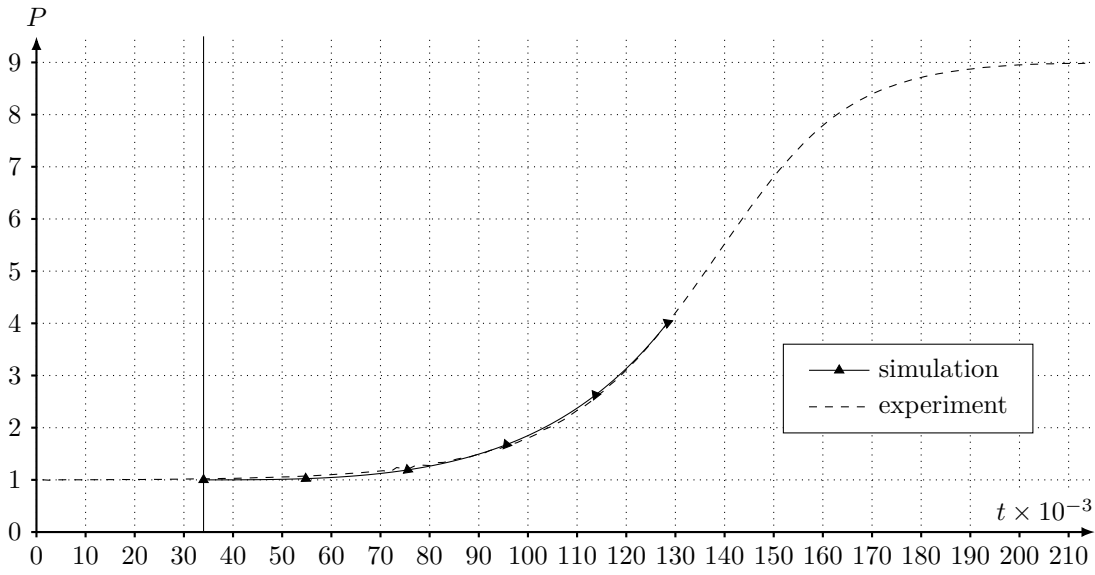


Figure 7.23.: Pressure-time curves of the simulation and experiment no. D4, 5 m³ cylinder, $\tilde{K}_{St} = 178$ bar m/s, offset $t_o = 0.034$.

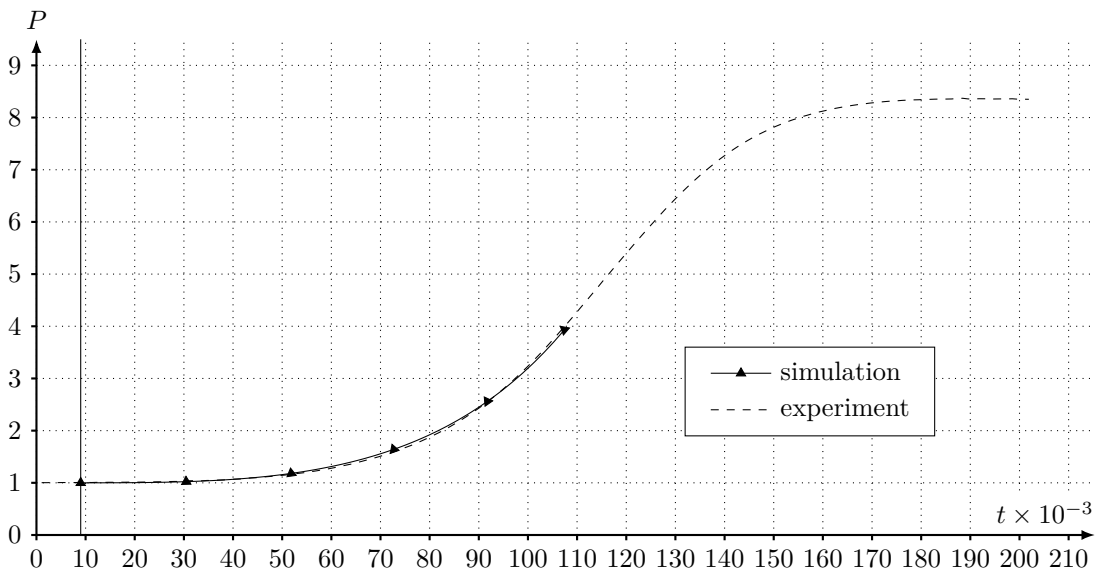


Figure 7.24.: Pressure-time curves of the simulation and experiment no. D5, 5 m³ cylinder, $\tilde{K}_{St} = 62$ bar m/s, offset $t_o = 0.009$.

7. Results & Discussion

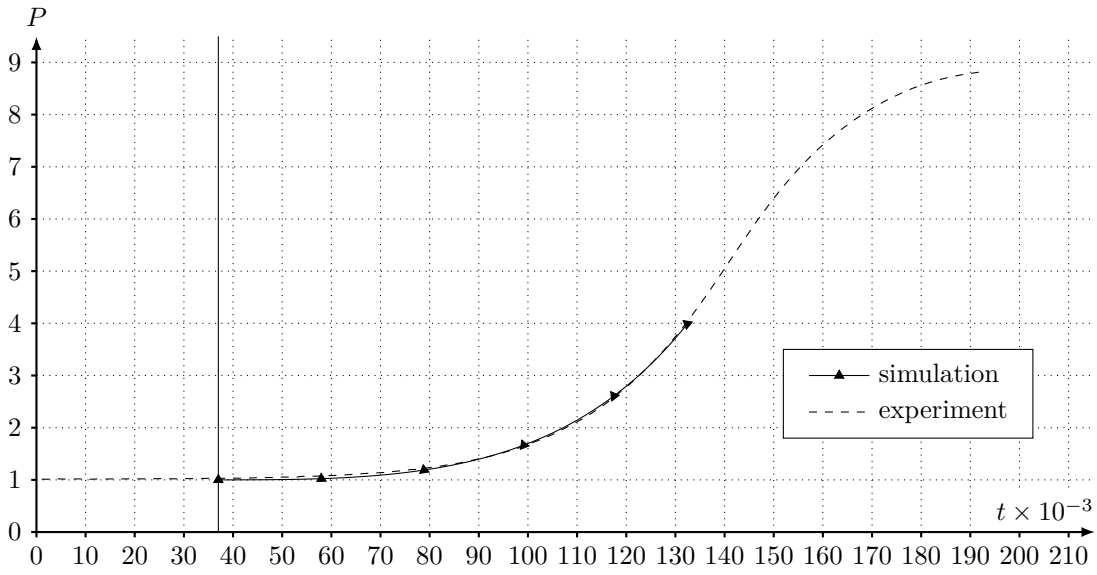


Figure 7.25.: Pressure-time curves of the simulation and experiment no. C2, 10 m³ cylinder, $\tilde{K}_{St} = 249$ bar m/s, offset $t_o = 0.037$.

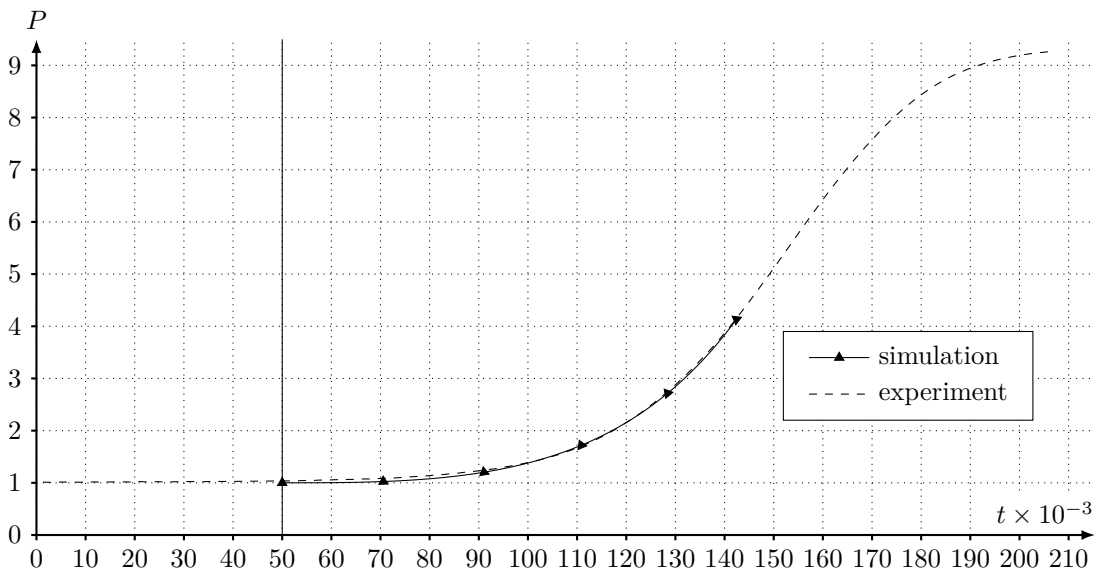


Figure 7.26.: Pressure-time curves of the simulation and experiment no. C3, 10 m³ cylinder, $\tilde{K}_{St} = 236$ bar m/s, offset $t_o = 0.05$.

7. Results & Discussion

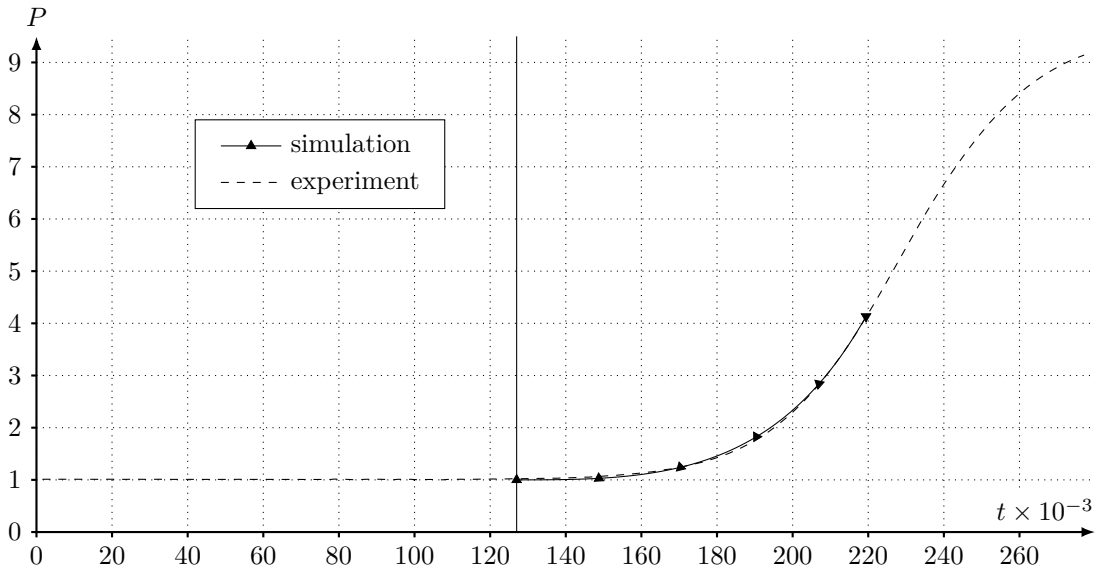


Figure 7.27.: Pressure-time curves of the simulation and experiment no. C4, 10 m^3 cylinder, $\tilde{K}_{\text{St}} = 161 \text{ bar m/s}$, offset $t_o = 0.127$.

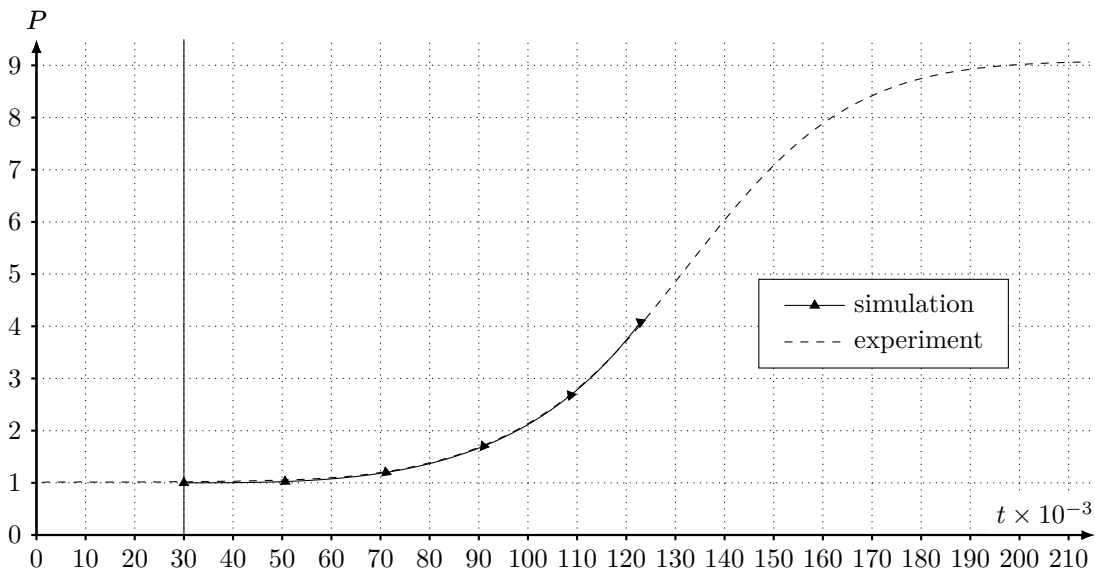


Figure 7.28.: Pressure-time curves of the simulation and experiment no. C6, 10 m^3 cylinder, $\tilde{K}_{\text{St}} = 96 \text{ bar m/s}$, offset $t_o = 0.03$.

8. Conclusion

An extension of the simple one-dimensional approximations for confined dust deflagration is presented. The resulting model accounts for flame-flow interactions and the influence of the non-spherical vessel wall. The numerical implementation is restricted to rotational symmetric geometries.

The aim of this thesis was to develop a reliable tool for explosion simulations. The implementation has been verified using simple test cases. The comparison with experimental data indicates that the burning velocity increases linearly with the deflagration index. However, more experiments have to be conducted to affirm this result.

Key Findings

By means of asymptotic expansion, the full model has been reduced significantly, as outlined in Chapter 3. This results in a problem statement with the following features: The flow is isentropic, except at the flame front where entropy is produced. The velocity divergence and leading-order pressure are time-dependent only. The unburnt gas has a uniform density and temperature, and the flow in the unburnt gas is irrotational.

First, we considered two-dimensional geometries. The results for two-dimensional geometries show a deviation of more than 30 %, when comparing the maximum rate of pressure rise in an infinitely long cylinder with the one in a sphere (Figs. 6.5b and 6.6b). Thus, approximating three-dimensional geometries by two-dimensional models seems unlikely to produce better results than the one-dimensional theory. This is also the reason why no two-dimensional results were shown in Chapter 7.

One additional aim of this work was to consider three-dimensional geometries. Due to the numerical complexity, only axisymmetric three dimensional geometries were considered. An axisymmetric geometry has an axis of rotation. Thus, the geometry and all quantities can be described by two independent variables (r, z) in cylindrical coordinates.

The results presented in Section 7.1 show the following: The shape of the flame front remains spherical during a rather large period of the explosion (Figs. 7.3, 7.4, 7.9 and 7.10). Only at later stages of the explosion, or when the ignition is off-centre, the flame front adapts significantly to the vessel shape (Fig. 7.4c). For vessels that have a more complex shape, the flame front can no longer be approximated by a sphere anymore (Figs. 7.9 and 7.10). Additionally, the reaction enthalpy has a major impact on the flame and flow field. (Fig. 7.10). The location of ignition does not change the pressure-time and pressure rise-time curves, except that the final pressure is different (Figs. 7.2 and 7.6).

One would expect that the pressure history in an arbitrarily shaped vessel deviates significantly from the one obtained by the one-dimensional approximation inside a sphere with the same volume as the vessel. However, it is remarkable that this is not the case: The

8. Conclusion

one-dimensional model from Section 6.2 predicts almost the same pressure-time curve than the full model, for a complex geometry (Fig. 7.7). The reason behind this remains unclear: When taking a look at the governing equations, it is not obvious that the pressure-time curve is independent from the vessel shape. Also, in this case the flame front adapts to the shape of the vessel and becomes non-spherical (Fig. 7.9b).

Limitations

The assumptions behind the model limit its applicability: First, it is assumed that the vessel wall is adiabatic. In experiments, this is almost never the case. However, the deflagration happens on a much faster time scale compared to heat conduction. Additionally, viscosity, thermal diffusion and gravity are neglected. Including those effects is not possible in the numerical framework of the implementation presented in this thesis.

The numerical treatment of the tracking of the flame front comes with a number of limitations. One is that the flame front has to remain stable by choosing a sufficiently high stabilisation number. A wrinkled flame front would lead to singularities in the jump of the vorticity, because the gradient of the curvature of the flame front is singular at a cusp. Additionally, the combination of moving marker points and the panel method does not cope well with a non-smooth flame front. However, the one-dimensional models currently used ignore the intrinsic hydrodynamic instabilities due to the symmetry constraints. For dust explosions, the instability does not play an important role, because the flame has a stabilising effect.

The simulation stops when the flame front touches the vessel wall. This is necessary, since the burnt gas is very hot and the heat loss to the surroundings is neglected. Once the flame front touches the vessel wall, there is a steep temperature gradient inside the vessel wall. Thus, the assumption of adiabatic boundaries becomes invalid. This can be a serious limitation: Consider a very elongated cylindrical vessel. After ignition, the flame front touches the vessel wall very early. Thus, only the first stages of the combustion process can be simulated. However, this problem could be solved by including a mechanism to slow down the flame front in the vicinity of the vessel wall. Eq. (2.8) could be extended:

$$\tilde{s}_{\text{eff}} = \left(1 - \tilde{\kappa} \tilde{l}_{\text{Ma}}^{\text{turb.}}\right) \left(\frac{\tilde{T}_{\text{u}}}{\tilde{T}_{\text{ref}}}\right)^2 \left(\frac{\tilde{p}_{\text{ref}}}{\tilde{p}}\right)^{\beta} \left(1 - \exp\left(\frac{\tilde{d}_{\text{n}}}{\tilde{d}^*}\right)\right) \tilde{s}_{\text{eff}}^0.$$

\tilde{d}_{n} is the wall normal distance of the flame front from the vessel wall, and \tilde{d}^* is a wall-influence parameter. This would lower the burning velocity when the flame front approaches the vessel wall. Thus, the pressure-time curve would experience a point of inflection and the maximum rate of pressure rise would not be at the end of the simulation anymore.

Future Improvements

In the numerical implementation, the ratios of specific heats in unburnt and burnt gas were assumed to be equal. This was done because the divergence of the velocity field becomes time-dependent only. Thus, a great simplification of the numerical procedure

8. Conclusion

was possible. However, accounting for different values of γ could be doable: One would have to find two different particulate solutions to Eq. (3.32) for unburnt and burnt gas. The resulting jump of the velocity at the flame front would have to be compensated by an additional boundary value problem at the flame front. This can be done by placing singular source and vortex sources along the flame front, to compensate for the jump of normal and tangential velocity, respectively.

In the industry, explosion vents are used to reduce the impact of an explosion on men and material. As a future extension, one could include such a feature in the framework of this implementation. However, one key assumption was that locally, the speed remains low compared to the speed of sound. In the vicinity of the explosion vent, this condition does not always hold. Thus, one would have to be very careful when including explosion venting in the future.

Two very basic models for the burning velocity have been combined. Due to the flexibility of the implementation, more complex descriptions of s_{eff} can be included in the numerical framework. A simple addition would be to introduce a dependency of the burning velocity on the normal distance of the vessel wall, as described before.

The numerical implementation is currently not optimised for maximum performance. Many numerical integrals and functions have to be evaluated millions of times. Currently, this is done without any optimisation. In the future, look-up tables and smart interpolation could yield significantly lower simulation run times.

Unique Aspects of this Work

The flame-flow interaction and the influence of the vessel wall on the flame front are the main new features, compared to the simple one-dimensional models, presented in this thesis. In the scientific literature, often only two-dimensional geometries are used. This poses a serious limitation for industrial applications, since no vessel types can be approximated by such geometries. Here, rotational symmetric, three-dimensional explosion events can be successfully simulated. This serves as a robust base for more advanced, but feasible explosion modelling in the process industry.

A. Rotational Symmetric Panel Velocity

In three dimensions, the potential of a point source is proportional to the inverse distance. q is the source strength per area:

$$\varphi = \frac{q}{4\pi} \frac{1}{\|\mathbf{x} - \mathbf{x}_s\|}, \quad (\text{A.1})$$

or, with $r' = \|\mathbf{x} - \mathbf{x}_s\|$:

$$\varphi = \frac{q}{4\pi} \frac{1}{r'}. \quad (\text{A.2})$$

This formulation has the advantage that it is independent of the choice of the coordinate system. Fig. A.1 shows an axisymmetric panel, which is a truncated cone. The task is to integrate the inverse of the distance r' from an arbitrary point (r, z) in the $\vartheta = 0$ plane over the surface of the truncated cone:

$$\varphi = \frac{q}{4\pi} \iint \frac{1}{r'} dO. \quad (\text{A.3})$$

With $dO = r_p d\vartheta'_p dz_p$, Eq. (A.3) reads as:

$$\varphi = \frac{q}{4\pi} \int_{z_1}^{z_2} \int_0^{2\pi} \frac{r_p}{r'} d\vartheta'_p dz_p = \frac{q}{2\pi} \int_{z_1}^{z_2} \int_0^{\pi} \frac{r_p}{r'} d\vartheta'_p dz_p. \quad (\text{A.4})$$

The integration over the panel angle ϑ'_p is done only between 0 and π because of the symmetry of the panel. In the $\vartheta = 0$ plane, (r_1, z_1) and (r_2, z_2) are the start and end point of the panel, respectively. For a rotational symmetric panel, as shown in Fig. A.1, we get for r' in cylinder coordinates (r, ϑ, z) :

$$r' = \sqrt{(r^2 + r_p^2 - 2rr_p \cos \vartheta'_p) + (z - z_p)^2}. \quad (\text{A.5})$$

Here, the law of cosines has been used and $\mathbf{x}_p = (r_p, \vartheta'_p, z_p)$ is a point on the surface of the panel. By some simple transformations, we get for r' :

$$r' = \sqrt{(r - r_p)^2 + (z - z_p)^2 + 4rr_p \sin^2 \vartheta'_p / 2}. \quad (\text{A.6})$$

Combining Eqs. (A.4) and (A.6) yields:

A. Rotational Symmetric Panel Velocity

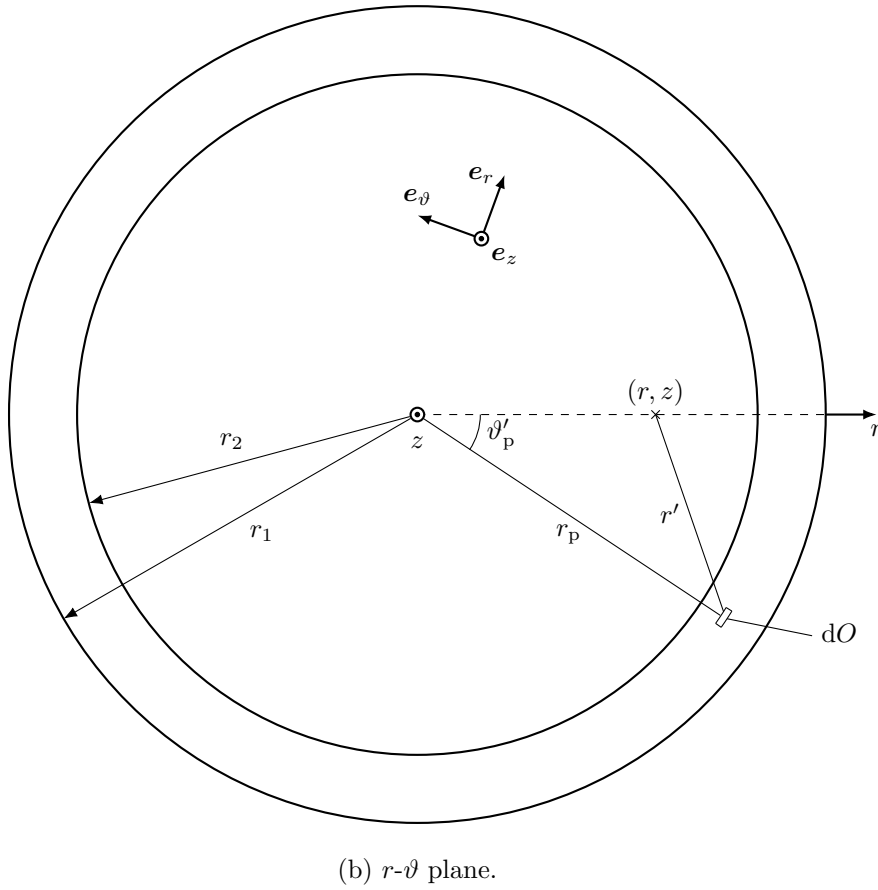
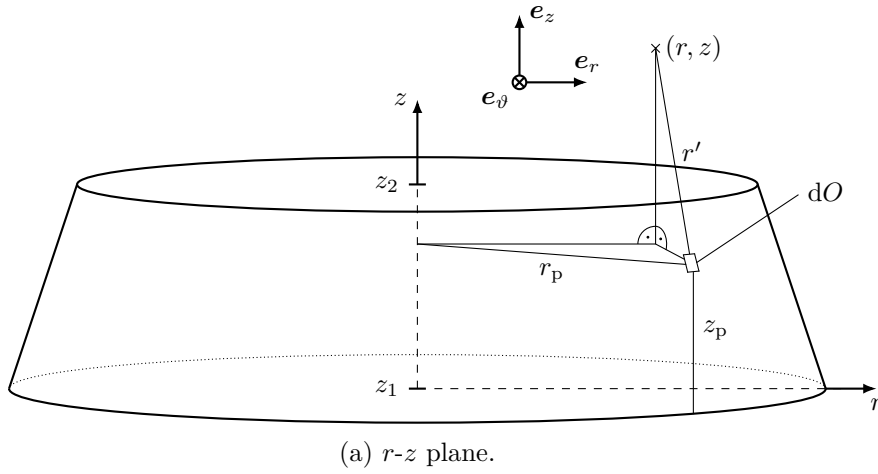


Figure A.1.: A rotational symmetric panel is a truncated cone. It is used to discretise flame front and vessel wall in the axisymmetric case. The total velocity induced by one panel is the surface integral of the velocity density over the surface of the panel. r' is the distance from an arbitrary point (r, z) in the $\vartheta = 0$ plane to a surface element dO of the panel.

A. Rotational Symmetric Panel Velocity

$$\varphi = \frac{q}{2\pi} \int_{z_1}^{z_2} \int_0^\pi \frac{r_p d\vartheta'_p dz_p}{\sqrt{(r-r_p)^2 + (z-z_p)^2 + 4rr_p \sin^2 \vartheta'_p/2}}. \quad (\text{A.7})$$

Transforming $\vartheta'_p/2 = \vartheta_p$ yields:

$$\varphi = \frac{q}{\pi} \int_{z_1}^{z_2} \int_0^{\pi/2} \frac{r_p d\vartheta_p dz_p}{\sqrt{(r-r_p)^2 + (z-z_p)^2 + 4rr_p \sin^2 \vartheta_p}}. \quad (\text{A.8})$$

For the velocity in radial direction u_r , we get:

$$u_r = \frac{\partial \varphi}{\partial r} = -\frac{q}{\pi} \int_{z_1}^{z_2} \int_0^{\pi/2} \frac{(r-r_p) + 2r_p \sin^2 \vartheta_p}{\left((r-r_p)^2 + (z-z_p)^2 + 4rr_p \sin^2 \vartheta_p\right)^{3/2}} r_p d\vartheta_p dz_p. \quad (\text{A.9})$$

The velocity u_z in z direction reads as:

$$u_z = \frac{\partial \varphi}{\partial z} = -\frac{q}{\pi} \int_{z_1}^{z_2} \int_0^{\pi/2} \frac{z-z_p}{\left((r-r_p)^2 + (z-z_p)^2 + 4rr_p \sin^2 \vartheta_p\right)^{3/2}} r_p d\vartheta_p dz_p. \quad (\text{A.10})$$

Next, we show that Eqs. (A.9) and (A.10) can be expressed with the help of complete elliptic integrals. We divide numerator and denominator by $\left((r-r_p)^2 + (z-z_p)^2\right)^{3/2}$ and get for u_r :

$$u_r = -\frac{q}{2\pi} \int_{z_1}^{z_2} \int_0^{\pi/2} \frac{(r-r_p) + 2r_p \sin^2 \vartheta_p}{\left((r-r_p)^2 + (z-z_p)^2\right)^{3/2}} \frac{1}{(1+m \sin^2 \vartheta_p)^{3/2}} r_p d\vartheta_p dz_p, \quad (\text{A.11})$$

and u_z :

$$u_z = -\frac{q}{2\pi} \int_{z_1}^{z_2} \int_0^{\pi/2} \frac{z-z_p}{\left((r-r_p)^2 + (z-z_p)^2\right)^{3/2}} \frac{1}{(1+m \sin^2 \vartheta_p)^{3/2}} r_p d\vartheta_p dz_p, \quad (\text{A.12})$$

where m is:

$$m = \frac{4rr_p}{(r-r_p)^2 + (z-z_p)^2}. \quad (\text{A.13})$$

We introduce a parameter $s \in [0, 1]$ as follows:

$$z_p(s) = z_1 + s(z_2 - z_1), \quad r_p(s) = r_1 + s(r_2 - r_1).$$

With $dz_p = (z_2 - z_1) ds$, u_r reads as:

A. Rotational Symmetric Panel Velocity

$$u_r = -\frac{q}{\pi} \int_0^1 \int_0^{\pi/2} \frac{(r - r_p(s)) + 2r_p(s) \sin^2 \vartheta_p}{\left((r - r_p(s))^2 + (z - z_p(s))^2\right)^{3/2}} \frac{r_p(s) (z_2 - z_1)}{(1 + m(s) \sin^2 \vartheta_p)^{3/2}} d\vartheta_p ds, \quad (\text{A.14})$$

and u_z reads as:

$$u_z = -\frac{q}{\pi} \int_0^1 \int_0^{\pi/2} \frac{z - z_p(s)}{\left((r - r_p(s))^2 + (z - z_p(s))^2\right)^{3/2}} \frac{r_p(s) (z_2 - z_1)}{(1 + m(s) \sin^2 \vartheta_p)^{3/2}} d\vartheta_p ds. \quad (\text{A.15})$$

By rewriting Eq. (A.14), we get for u_r :

$$u_r = -\frac{q}{\pi} \int_0^1 (r - r_p(s)) d(s) \int_0^{\pi/2} \frac{1 + e(s) \sin^2 \vartheta_p}{(1 + m(s) \sin^2 \vartheta_p)^{3/2}} d\vartheta_p ds, \quad (\text{A.16})$$

and for Eq. (A.15), we get u_z :

$$u_z = -\frac{q}{\pi} \int_0^1 (z - z_p(s)) d(s) \int_0^{\pi/2} \frac{1}{(1 + m(s) \sin^2 \vartheta_p)^{3/2}} d\vartheta_p ds, \quad (\text{A.17})$$

with

$$d(s) = \frac{r_p(s) (z_2 - z_1)}{\left((r - r_p(s))^2 + (z - z_p(s))^2\right)^{3/2}}, \quad (\text{A.18})$$

and

$$e(s) = \frac{2r_p(s)}{r - r_p(s)}. \quad (\text{A.19})$$

We need to evaluate integrals of the form,

$$\int_0^{\pi/2} \frac{\sin^2 \phi}{(1 + m \sin^2 \phi)^{3/2}} d\phi, \quad (\text{A.20})$$

and

$$\int_0^{\pi/2} \frac{1}{(1 + m \sin^2 \phi)^{3/2}} d\phi. \quad (\text{A.21})$$

With the complete elliptic integral of the first kind, K , defined as [92, Eq. (17.3.1)],

A. Rotational Symmetric Panel Velocity

$$K(m) = \int_0^{\pi/2} \frac{1}{\sqrt{1 - m \sin^2 \phi}} d\phi, \quad (\text{A.22})$$

and the complete integral of the second kind, E, defined as [92, Eq. (17.3.3)],

$$E(m) = \int_0^{\pi/2} \sqrt{1 - m \sin^2 \phi} d\phi, \quad (\text{A.23})$$

we can express Eq. (A.21) easily [101, Eqs. (19.2.7) and (19.6.1)]:

$$\int_0^{\pi/2} \frac{1}{(1 + m \sin^2 \phi)^{3/2}} d\phi = \frac{E(-m)}{1 + m}. \quad (\text{A.24})$$

For Eq. (A.20), the solution is obtained using a computer algebra system:

$$\int_0^{\pi/2} \frac{\sin^2 \phi}{(1 + m \sin^2 \phi)^{3/2}} d\phi = \frac{(1 + m) K(-m) - E(-m)}{m(1 + m)}, \quad (\text{A.25})$$

A simple transformation $\phi = \pi/2 - \theta$ yields the complete elliptic integral of first kind with negative parameter:

$$K(-m) = \frac{1}{\sqrt{1 + m}} K(m'), \quad (\text{A.26})$$

and of second kind:

$$E(-m) = \sqrt{1 + m} E(m'), \quad (\text{A.27})$$

with $m' = m/(1 + m)$. With Eqs. (A.24), (A.25), (A.26) and (A.27), we finally obtain u_r :

$$u_r = \frac{q}{\pi} \int_0^1 \frac{(r_p(s) - r) d(s)}{m(s) \sqrt{1 + m(s)}} ((m(s) - e(s)) E(m'(s)) + K(m'(s))) ds, \quad (\text{A.28})$$

and u_z :

$$u_z = \frac{q}{\pi} \int_0^1 (z_p(s) - z) d(s) \frac{E(m'(s))}{\sqrt{1 + m(s)}} ds. \quad (\text{A.29})$$

B. Numerical Details

In this chapter, some details about the numerical implementation are given. The implementation of the model described in the previous chapters was done in a computer program written in the C programming language. Additionally, the GSL library [102] was used for numerical integration and evaluation of elliptic integrals and Bessel functions. The CBLAS interface was used for basic linear algebra [103]. Output was done using the HDF5 library [104]. Pre and post processing tools were written in the Python programming language.

Calculation of the Curvature

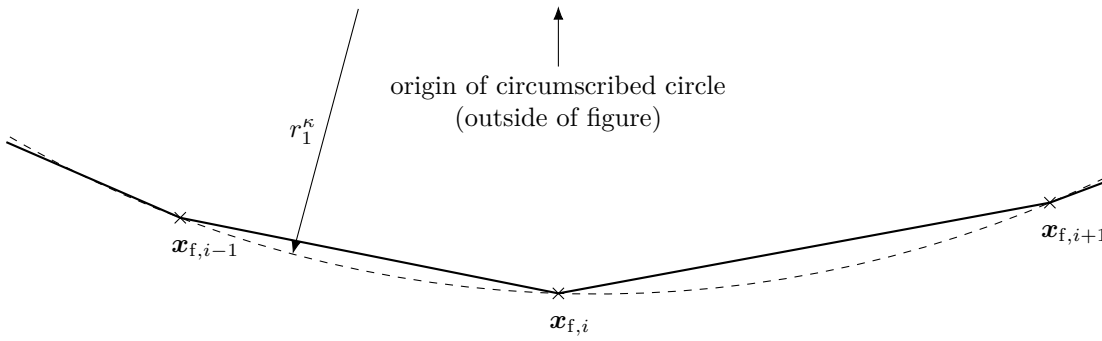


Figure B.1.: The first radius of curvature r_1^κ at a point $\mathbf{x}_{f,i}$ of the flame front is approximated by the radius of the circumscribed circle (- -) of the triangle which is formed by the point and its adjacent neighbours $\mathbf{x}_{f,i\pm 1}$.

The total curvature κ is the mean of the two main curvatures κ_1, κ_2 :

$$\kappa = \frac{1}{2} (\kappa_1 + \kappa_2), \quad (\text{B.1})$$

and the main curvature is the inverse of the main curvature radius r_i^κ :

$$\kappa_i = \frac{1}{r_i^\kappa} \quad (\text{B.2})$$

In 2D, one main curvature is zero, $\kappa_2 = 0$. Thus, the total curvature $\kappa^{2\text{D}}$ reads as:

$$\kappa^{2\text{D}} = \frac{\kappa_1}{2}. \quad (\text{B.3})$$

r_1^κ is the radius of the circumscribed circle of three neighbouring points, see Fig. B.1.

B. Numerical Details

For rotational symmetric geometries, one curvature is the inverse radius of the circumscribed circle, as described before. The other main curvature is obtained by the inverse radius of the sphere which has its origin on the rotation axis, and touches the middle of one panel, cf. Fig. B.2.

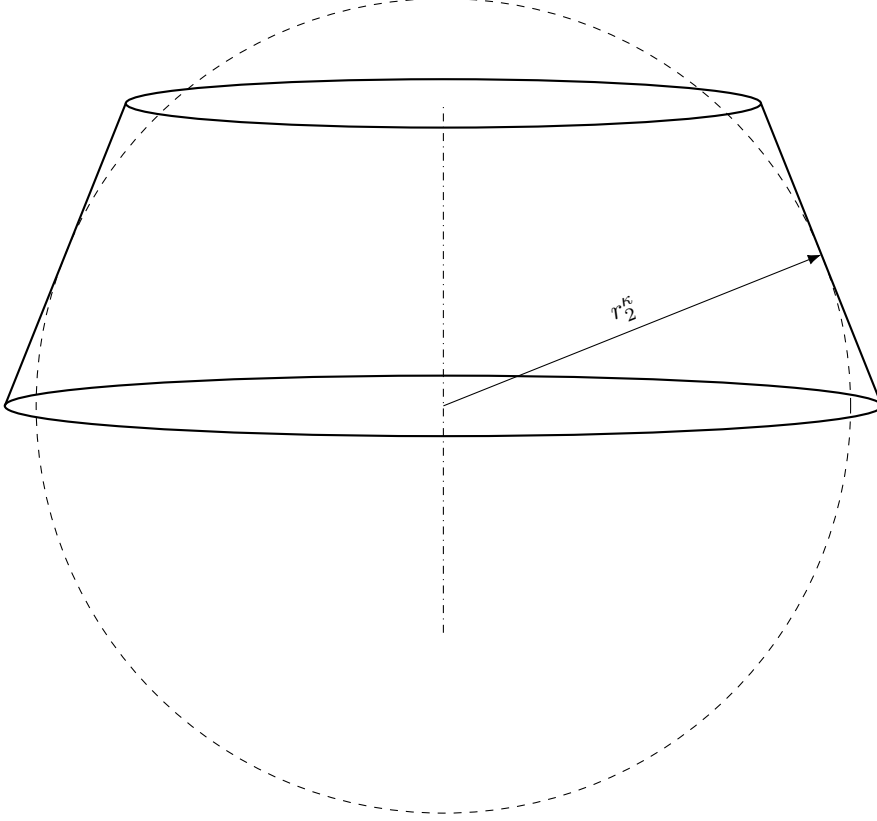


Figure B.2.: The radius of the circumscribed sphere inside a truncated cone is the second radius of curvature r_2^k .

Interpolation of the Material Derivative of the Velocity

The velocity at each panel edge is singular [90]. When a Lagrangian mesh point jumps over the flame front near the edge of a panel, its velocity in the vicinity of panel edges is interpolated using the next available non-interpolated value. If none exist, i.e. at the beginning of the simulation, it is set to zero.

Gradient Calculation on a Distorted Grid

Assume that we have a central point $\mathbf{x}_{ij} = \mathbf{x}^c$, and its four neighbours: $\mathbf{x}_{i-1,j} = \mathbf{x}^l$ (left), $\mathbf{x}_{i+1,j} = \mathbf{x}^r$ (right), $\mathbf{x}_{i,j-1} = \mathbf{x}^b$ (bottom) and $\mathbf{x}_{i,j+1} = \mathbf{x}^t$ (top). To obtain the gradient of a quantity b which is defined on those grid points, we expand b into a Taylor series about the central point \mathbf{x}^c . For Cartesian coordinates, we get:

B. Numerical Details

$$b^c \approx b^c \tag{B.4}$$

$$b^l \approx b^c - \Delta x^l \frac{\partial b^c}{\partial x} - \Delta y^l \frac{\partial b^c}{\partial y} + \frac{(\Delta x^l)^2}{2} \frac{\partial^2 b^c}{\partial x^2} + \frac{(\Delta y^l)^2}{2} \frac{\partial^2 b^c}{\partial y^2}, \tag{B.5}$$

$$b^r \approx b^c + \Delta x^r \frac{\partial b^c}{\partial x} + \Delta y^r \frac{\partial b^c}{\partial y} + \frac{(\Delta x^r)^2}{2} \frac{\partial^2 b^c}{\partial x^2} + \frac{(\Delta y^r)^2}{2} \frac{\partial^2 b^c}{\partial y^2}, \tag{B.6}$$

$$b^b \approx b^c - \Delta x^b \frac{\partial b^c}{\partial x} - \Delta y^b \frac{\partial b^c}{\partial y} + \frac{(\Delta x^b)^2}{2} \frac{\partial^2 b^c}{\partial x^2} + \frac{(\Delta y^b)^2}{2} \frac{\partial^2 b^c}{\partial y^2}, \tag{B.7}$$

$$b^t \approx b^c + \Delta x^t \frac{\partial b^c}{\partial x} + \Delta y^t \frac{\partial b^c}{\partial y} + \frac{(\Delta x^t)^2}{2} \frac{\partial^2 b^c}{\partial x^2} + \frac{(\Delta y^t)^2}{2} \frac{\partial^2 b^c}{\partial y^2}. \tag{B.8}$$

Δx and Δy are the x and y distances between the centre point and the corresponding point, e.g. $\Delta x^l = x^c - x^l$ and $\Delta y^t = y^t - y^c$. In cylindrical coordinates, x has to be replaced by the radius r , and y by the height z .

Now, we multiply Eqs. (B.4) to (B.8) with coefficients a^c , a^l , a^r , a^b and a^t , respectively:

$$a^c b^c \approx a^c b^c, \tag{B.9}$$

$$a^l b^l \approx a^l \left(b^c - \Delta x^l \frac{\partial b^c}{\partial x} - \Delta y^l \frac{\partial b^c}{\partial y} + \frac{(\Delta x^l)^2}{2} \frac{\partial^2 b^c}{\partial x^2} + \frac{(\Delta y^l)^2}{2} \frac{\partial^2 b^c}{\partial y^2} \right), \tag{B.10}$$

$$a^r b^r \approx a^r \left(b^c + \Delta x^r \frac{\partial b^c}{\partial x} + \Delta y^r \frac{\partial b^c}{\partial y} + \frac{(\Delta x^r)^2}{2} \frac{\partial^2 b^c}{\partial x^2} + \frac{(\Delta y^r)^2}{2} \frac{\partial^2 b^c}{\partial y^2} \right), \tag{B.11}$$

$$a^b b^b \approx a^b \left(b^c - \Delta x^b \frac{\partial b^c}{\partial x} - \Delta y^b \frac{\partial b^c}{\partial y} + \frac{(\Delta x^b)^2}{2} \frac{\partial^2 b^c}{\partial x^2} + \frac{(\Delta y^b)^2}{2} \frac{\partial^2 b^c}{\partial y^2} \right), \tag{B.12}$$

$$a^t b^t \approx a^t \left(b^c + \Delta x^t \frac{\partial b^c}{\partial x} + \Delta y^t \frac{\partial b^c}{\partial y} + \frac{(\Delta x^t)^2}{2} \frac{\partial^2 b^c}{\partial x^2} + \frac{(\Delta y^t)^2}{2} \frac{\partial^2 b^c}{\partial y^2} \right). \tag{B.13}$$

In order to get an expression for the gradient, we make the sum of Eqs. (B.9) to (B.13) and write:

B. Numerical Details

$$\begin{aligned}
a^c b^c + a^l b^l + a^r b^r + a^b b^b + a^t b^t &\approx \underbrace{(a^c + a^l + a^r + a^b + a^t)}_{=0} b^c \\
&+ \underbrace{(-a^l \Delta x^l + a^r \Delta x^r - a^b \Delta x^b + a^t \Delta x^t)}_{=1/0 \text{ (for } x/y \text{ direction)}} \frac{\partial b^c}{\partial x} \\
&+ \underbrace{(-a^l \Delta y^l + a^r \Delta y^r - a^b \Delta y^b + a^t \Delta y^t)}_{=0/1 \text{ (for } x/y \text{ direction)}} \frac{\partial b^c}{\partial y} \\
&+ \underbrace{\left(a^l \frac{(\Delta x^l)^2}{2} + a^r \frac{(\Delta x^r)^2}{2} + a^b \frac{(\Delta x^b)^2}{2} + a^t \frac{(\Delta x^t)^2}{2} \right)}_{=0} \frac{\partial^2 b^c}{\partial x^2} \\
&+ \underbrace{\left(a^l \frac{(\Delta y^l)^2}{2} + a^r \frac{(\Delta y^r)^2}{2} + a^b \frac{(\Delta y^b)^2}{2} + a^t \frac{(\Delta y^t)^2}{2} \right)}_{=0} \frac{\partial^2 b^c}{\partial y^2}. \quad (\text{B.14})
\end{aligned}$$

For the gradient, the first, fourth and fifth term in brackets on the right-hand side have to vanish. Depending on the direction of the gradient, either the second or third term have to be one, and the other zero. Thus, the discretised gradient is the linear combination of the values of b at the five involved grid points. The partial derivative with respect to x reads:

$$\frac{\partial b^c}{\partial x} \approx a_x^c b^c + a_x^l b^l + a_x^r b^r + a_x^b b^b + a_x^t b^t, \quad (\text{B.15})$$

The coefficients a_x are solution of the system of equations:

$$\begin{pmatrix} 1 & 1 & 1 & 1 & 1 \\ 0 & -\Delta x^l & \Delta x^r & -\Delta x^b & \Delta x^t \\ 0 & -\Delta y^l & \Delta y^r & -\Delta y^b & \Delta y^t \\ 0 & (\Delta x^l)^2 & (\Delta x^r)^2 & (\Delta x^b)^2 & (\Delta x^t)^2 \\ 0 & (\Delta y^l)^2 & (\Delta y^r)^2 & (\Delta y^b)^2 & (\Delta y^t)^2 \end{pmatrix} \begin{pmatrix} a_x^c \\ a_x^l \\ a_x^r \\ a_x^b \\ a_x^t \end{pmatrix} = \begin{pmatrix} 0 \\ 1 \\ 0 \\ 0 \\ 0 \end{pmatrix}. \quad (\text{B.16})$$

Similarly, the partial derivative with respect to y reads as:

$$\frac{\partial b^c}{\partial y} \approx a_y^c b^c + a_y^l b^l + a_y^r b^r + a_y^b b^b + a_y^t b^t. \quad (\text{B.17})$$

The coefficients a_y are solution to the linear system of equations:

$$\begin{pmatrix} 1 & 1 & 1 & 1 & 1 \\ 0 & -\Delta x^l & \Delta x^r & -\Delta x^b & \Delta x^t \\ 0 & -\Delta y^l & \Delta y^r & -\Delta y^b & \Delta y^t \\ 0 & (\Delta x^l)^2 & (\Delta x^r)^2 & (\Delta x^b)^2 & (\Delta x^t)^2 \\ 0 & (\Delta y^l)^2 & (\Delta y^r)^2 & (\Delta y^b)^2 & (\Delta y^t)^2 \end{pmatrix} \begin{pmatrix} a_y^c \\ a_y^l \\ a_y^r \\ a_y^b \\ a_y^t \end{pmatrix} = \begin{pmatrix} 0 \\ 0 \\ 1 \\ 0 \\ 0 \end{pmatrix}. \quad (\text{B.18})$$

B. Numerical Details

This central finite difference scheme is used to calculate the gradient of the entropy and the material derivative of the velocity. It is only needed for Lagrangian points which are in the burnt gas. Mesh points inside the burnt gas and in the vicinity of the flame front do not always have four neighbours which are inside the burnt gas. In such a case, suitable one-sided finite difference schemes are applied.

Initialisation

All numerical parameters are either provided or default values are used. The vessel wall panels are read from a file. Its location is mapped to a square with $[0, 1 - \Delta_{\text{fix}}]^2$. If the provided vessel wall points are outside of this square, the vessel is shifted and scaled, i.e. a geometrically similar vessel is found that fits in the area of computation. This is needed because then, Fourier transformations become easier. Then, the flame front is initialised as a sphere, with given initial radius and location. Next, the moving mesh points are evenly distributed inside the vessel. Additionally, points outside of the vessel are placed since it has to be guaranteed that the value of the vorticity outside the vessel is equal to zero for the least-square problem, Eq. (5.95).

Linear Equation Solver

Solving a linear system of equations is needed for finding (I) the source strengths of the vessel wall panels, (II) the coefficients for the finite differences gradient scheme and (III) the best Fourier transformation on the fixed mesh. Here, a direct, self-written linear equation solver was implemented, using LU decomposition. Pivoting was not necessary, since the matrices are diagonally dominant.

Elliptic Integrals and Bessel Functions

Routines provided by the GNU Scientific Library were used to evaluate elliptic integrals and Bessel functions [102]. No performance optimisation was done, i.e. no lookup table or interpolation between already known values. Since the argument to those functions is limited between zero and one, a faster implementation is possible in the future.

Numerical Integration

To evaluate the integral equations for rotational symmetric panels, a numerical integration scheme is required. Here, the ‘CQUAD doubly-adaptive integration’ routine `gsl_integration_cquad` from the GNU Scientific Library is used. This function implements the Clenshaw-Curtis quadrature rules [105]. It automatically divides the integration interval into smaller sub-intervals adaptively, i.e. a smaller interval where a larger error is observed. This function can handle most types of singularities and divergent integrals according to the manual [102].

B. Numerical Details

Solving a System of ODE

To solve a system of non-linear ordinary differential equations, a standard Python function from SciPy was used [106]. This is needed to solve the coupled system of ODE for the one-dimensional model.

Program Options

To run a simulation, one can specify a number of parameters, either via command line options, or by writing a configuration file. If no value is provided, a default value is used. All parameters are listed in Tab. B.1.

Table B.1.: Command line options for the `flamier` program, name: name of the parameter in the configuration file, option: name of the corresponding command line option.

name/option	description	default
<code>front-panel-angle/-a</code>	minimum angle α_{\min} between two front panels	0
<code>beta/-b</code>	pressure-dependency β of s_L	0
<code>config/-c</code>	name of the configuration file	—
<code>delta/-d</code>	initial distance Δ between moving mesh points	0.05
<code>end-time/-e</code>	end time	1
<code>front-panel-number/-f</code>	number of flame front panels	150
<code>h5file/-H</code>	name of HDF5 output file	<code>result.h5</code>
<code>reaction-enthalpy/-h</code>	reaction enthalpy Δh_f	20
<code>interpolation-area/-i</code>	radius of the interpolation area for $D\mathbf{u}/Dt$	1
<code>gamma/-k</code>	ratio of specific heats γ	1.4
<code>front-panel-length/-L</code>	average front panel length l_{avg}	1
<code>log/-l</code>	name of log file	<code>stdout</code>
<code>markstein-length/-M</code>	Markstein number Ma	0.01
<code>mode/-m</code>	mode of simulation: <code>periodic</code> , <code>twodim</code> , <code>rotsym</code>	<code>rotsym</code>
<code>workdir/-o</code>	working directory of the simulation	<code>.</code>
<code>init-radius/-r</code>	initial radius of the flame front r_i	0.01
<code>time-step/-t</code>	time step Δt	5×10^{-6}
<code>wavenumber/-W</code>	initial wavenumber of the flame front k_i	5
<code>write-interval/-w</code>	number of time steps between two writes	20
<code>init-x/-x</code>	initial x location of the explosion	0
<code>init-y/-x</code>	initial y/z location of the explosion	0

Bibliography

- [1] R. K. Eckhoff, *Dust Explosions in the Process Industries*. Burlington: Gulf Professional Publishing, 3rd ed., 2003.
- [2] “The Fire Triangle.” https://www.sc.edu/ehs/training/Fire/01_triangle.htm. accessed on 25 February 2019.
- [3] “OSH Answers Fact Sheets.” https://www.ccohs.ca/oshanswers/chemicals/combustible_dust.html. accessed on 25 February 2019.
- [4] W. Bartknecht and with a contribution from G. Zwahlen, *Dust Explosions: Course, Prevention, Protection*. Berlin, Heidelberg: Springer-Verlag, 1989.
- [5] C. K. Law, *Combustion Physics*. Cambridge University Press, 2006.
- [6] T. Poinot and D. Veynante, *Theoretical and Numerical Combustion*. self-published by the authors, 3rd ed., 2012.
- [7] J. Nagy and H. C. Verakis, *Development and Control of Dust Explosions*. Occupational Safety and Health, New York: CRC Press, 1983.
- [8] R. A. Ogle, *Dust Explosion Dynamics*. Butterworth-Heinemann, 2017.
- [9] P. E. Moore and D. J. Spring, “Design of Explosion Isolation Barriers,” *Process Safety and Environmental Protection*, vol. 83, no. 2, pp. 161–170, 2005. Hazards XVIII.
- [10] J. Nagy, J. W. Conn, and H. C. Verakis, “Explosion Development in a Closed Vessel,” tech. rep., US Bureau of Mines, 1969. Report of Investigations 7279.
- [11] D. Bradley and A. Mitcheson, “Mathematical solutions for explosions in spherical vessels,” *Combustion and Flame*, vol. 26, pp. 201–217, 1976.
- [12] R. A. Ogle, J. K. Beddow, A. F. Vetter, and L.-D. Chen, “A thermal theory of laminar premixed dust flame propagation,” *Combustion and Flame*, vol. 58, no. 1, pp. 77–79, 1984.
- [13] S. Nomura and T. Tanaka, “Theoretical analysis of dust explosions,” *Powder Technology*, vol. 71, no. 2, pp. 189–196, 1992.
- [14] “Staubbrände und Staubexplosionen; Gefahren, Beurteilung, Schutzmaßnahmen; Untersuchungsmethoden zur Ermittlung von sicherheitstechnischen Kenngrößen von Stäuben,” Standard VDI 2263 Blatt 1, Verein Deutscher Ingenieure, Dusseldorf, Germany, 1990.
- [15] P. Field, “Dust Explosions,” *Handbook of Powder Technology*, Amsterdam: Elsevier, 1982.
- [16] A. E. Dahoe, R. S. Cant, M. J. Pegg, and B. Scarlett, “On the transient flow in the 20-liter explosion sphere,” *Journal of Loss Prevention in the Process Industries*, vol. 14, no. 6, pp. 475–487, 2001.

Bibliography

- [17] “The 1 m³ vessel for determination of explosion severity – why use it?.” Brochure published by DEKRA Insight, 2016.
- [18] “Combustible Dust National Emphasis Program (Reissued),” Directive CPL 03-00-008, Occupational Safety and Health Administration, US Department of Labor, Washington, DC, USA, 2008.
- [19] “Hazard Communication Guidance for Combustible Dusts,” Communication OSHA 3371-08 2009, Occupational Safety and Health Administration, US Department of Labor, 2009.
- [20] K. L. Cashdollar, “Overview of dust explosibility characteristics,” *Journal of Loss Prevention in the Process Industries*, vol. 13, pp. 183–199, 2000.
- [21] N. A. Rahman and M. S. Takriff, “Consequence Modelling of a Dust Explosion,” *International Journal of Safety and Security Engineering*, vol. 3, no. 3, pp. 212–219, 2013.
- [22] P. R. Amyotte, S. Chippett, and M. Pegg, “Effects of turbulence on dust explosions,” *Progress in Energy and Combustion Science*, vol. 14, no. 4, pp. 293–310, 1988.
- [23] A. E. Dahoe, J. F. Zevenbergen, S. M. Lemkowitz, and B. Scarlett, “Dust explosions in spherical vessels: The role of flame thickness in the validity of the ‘cube-root law’,” *Journal of Loss Prevention in the Process Industries*, vol. 9, no. 1, pp. 33–44, 1996.
- [24] J. Jarosinski, “The Thickness of Laminar Flames,” *Combustion and Flame*, vol. 56, no. 3, pp. 337–342, 1984.
- [25] W. Jost, *Explosions- und Verbrennungsvorgänge in Gasen*. Berlin: Verlag von Julius Springer, 1939.
- [26] G. Zhen and W. Leuckel, “Effects of ignitors and turbulence on dust explosions,” *Journal of Loss Prevention in the Process Industries*, vol. 10, no. 5, pp. 317–324, 1997.
- [27] F. Tamanini, “The role of turbulence in dust explosions,” *Journal of Loss Prevention in the Process Industries*, vol. 11, no. 1, pp. 1–10, 1998. Paper presented at the Seventh Colloquium on Dust Explosions, Bergen, Norway, 23–26 June 1996.
- [28] K. V. Wingerden, “Simulations of dust explosion using a CFD-code,” in *Proc. 7th Int. Coll. on Dust Explosions, Bergen*, pp. 6–42, 1996.
- [29] T. Skjold, B. J. Arntzen, O. R. Hansen, O. J. Taraldset, I. E. Storvik, and R. K. Eckhoff, “Simulating Dust Explosions with the First Version of DESC,” *Process Safety and Environmental Protection*, vol. 83, no. 2, pp. 151–160, 2005. Hazards XVIII.
- [30] T. Skjold, “Review of the DESC project,” *Journal of Loss Prevention in the Process Industries*, vol. 20, no. 4, pp. 291–302, 2007. Selected Papers Presented at the Sixth International Symposium on Hazards, Prevention and Mitigation of Industrial Explosions.
- [31] G. Collecutt, D. Humphreys, and D. Proud, “CFD simulation of underground coal dust explosions and active explosion barriers.” Paper presented at the Seventh International Conference on CFD in the Minerals and Process Industries, CSIRO, Melbourne, Australia, 9–11 December 2009, 2009.

Bibliography

- [32] V. K. Bind, S. Roy, and C. Rajagopal, "CFD modelling of dust explosions: Rapid combustion in a 20 L apparatus," *The Canadian Journal of Chemical Engineering*, vol. 89, no. 4, pp. 663–670, 2010.
- [33] C. Murillo, O. Dufaud, N. Bardin-Monnier, O. López, F. Munoz, and L. Perrin, "Dust explosions: CFD modeling as a tool to characterize the relevant parameters of the dust dispersion," *Chemical Engineering Science*, vol. 104, pp. 103–116, 2013.
- [34] C. Murillo, N. Bardin-Monnier, C. Blanchard, D. Funfschilling, F. Munoz, N. Ratkovich, D. Vizcaya, and O. Dufaud, "CFD to Improve the Repeatability and Accuracy of Dust Explosion Tests in the 20-liters Sphere," *Chemical Engineering Transactions*, vol. 48, pp. 115–120, 2016.
- [35] M. Matalon, "Intrinsic Flame Instabilities in Premixed and Nonpremixed Combustion," *Annual Review of Fluid Mechanics*, vol. 39, no. 1, pp. 163–191, 2007.
- [36] N. Peters, *Turbulent Combustion*. Cambridge Monographs on Mechanics, Cambridge University Press, 2000.
- [37] R. K. Eckhoff, "Current status and expected future trends in dust explosion research," *Journal of Loss Prevention in the Process Industries*, vol. 18, no. 4, pp. 225–237, 2005. Selected Papers Presented at the International Conference on Bhopal Gas Tragedy and its Effects on Process Safety.
- [38] G. P. Smith, D. M. Golden, M. Frenklach, B. Eiteener, M. Goldenberg, C. T. Bowman, R. K. Hanson, W. C. Gardiner, V. V. Lissianski, and Z. W. Qin, "GRI-Mech 3.0."
- [39] P. Saxena and F. A. Williams, "Numerical and experimental studies of ethanol flames," *Proceedings of the Combustion Institute*, vol. 31, no. 1, pp. 1149–1156, 2007.
- [40] N. M. Marinov, "A detailed chemical kinetic model for high temperature ethanol oxidation," *International Journal of Chemical Kinetics*, vol. 31, no. 3, pp. 183–220, 1999.
- [41] K. Hoyermann, F. Mauß, and T. Zeuch, "A detailed chemical reaction mechanism for the oxidation of hydrocarbons and its application to the analysis of benzene formation in fuel-rich premixed laminar acetylene and propene flames," *Physical Chemistry Chemical Physics*, vol. 6, pp. 3824–3835, 2004.
- [42] T. Plessing, C. Kortschik, N. Peters, M. S. Mansour, and R. K. Cheng, "Measurements of the turbulent burning velocity and the structure of premixed flames on a low-swirl burner," *Proceedings of the Combustion Institute*, vol. 28, no. 1, pp. 359–366, 2000.
- [43] G. Darrieus, "Propagation d'un front de flamme," *La Technique Moderne*, vol. 30, p. 18, 1938.
- [44] L. D. Landau, "On the theory of slow combustion," *Acta Physicochim (USSR)*, vol. 19, pp. 77–85, 1944.
- [45] G. H. Markstein, "Experimental and Theoretical Studies of Flame-Front Stability," *Journal of the Aeronautical Sciences*, vol. 18, no. 3, pp. 199–209, 1951.

Bibliography

- [46] B. Karlovitz, D. W. Denniston, D. H. Knapschaefer, and F. E. Wells, "Studies on Turbulent flames: A. Flame Propagation Across Velocity Gradients B. Turbulence Measurement in Flames," *Symposium (International) on Combustion*, vol. 4, no. 1, pp. 613–620, 1953. Fourth Symposium (International) on Combustion.
- [47] W. Eckhaus, "Theory of flame-front stability," *Journal of Fluid Mechanics*, vol. 10, no. 1, pp. 80–100, 1961.
- [48] G. I. Sivashinsky, "On a distorted flame front as a hydrodynamic discontinuity," *Acta Astronautica*, vol. 3, no. 11, pp. 889–918, 1976.
- [49] M. Matalon and B. J. Matkowsky, "Flames as gasdynamic discontinuities," *Journal of Fluid Mechanics*, vol. 124, pp. 239–259, 1982.
- [50] P. Clavin and F. A. Williams, "Effects of molecular diffusion and of thermal expansion on the structure and dynamics of premixed flames in turbulent flows of large scale and low intensity," *Journal of Fluid Mechanics*, vol. 116, pp. 251–282, 1982.
- [51] A. G. Class, B. J. Matkowsky, and A. Y. Klimenko, "Stability of planar flames as gasdynamic discontinuities," *Journal of Fluid Mechanics*, vol. 491, pp. 51–63, 2003.
- [52] A. G. Class, B. J. Matkowsky, and A. Y. Klimenko, "A unified model of flames as gasdynamic discontinuities," *Journal of Fluid Mechanics*, vol. 491, pp. 11–49, 2003.
- [53] J. D. Buckmaster and G. S. S. Ludford, *Lectures on Mathematical Combustion*. CBMS-NSF Regional Conference Series in Applied Mathematics, Philadelphia, Pennsylvania: Society for Industrial and Applied Mathematics, 1983.
- [54] A. N. Lipatnikov, "Some Issues of Using Markstein Number for Modeling Premixed Turbulent Combustion," *Combustion Science and Technology*, vol. 119, no. 1-6, pp. 131–154, 1996.
- [55] B. Lewis and G. von Elbe, *Combustion, Flames and Explosions of Gases*. San Diego: Academic Press, third edition ed., 1987.
- [56] G. H. Markstein, "Perturbation Analysis of Stability and Response of Plane Flame Fronts," in *Nonsteady Flame Propagation* (G. H. Markstein, ed.), pp. 15–74, Pergamon Press, 1964.
- [57] S. B. Pope, *Turbulent Flows*. Cambridge, UK: Cambridge University Press, 2006. Fourth Printing.
- [58] A. Dahoe and L. de Goey, "On the determination of the laminar burning velocity from closed vessel gas explosions," *Journal of Loss Prevention in the Process Industries*, vol. 16, no. 6, pp. 457–478, 2003.
- [59] S. P. Sharma, D. D. Agrawal, and C. P. Gupta, "The pressure and temperature dependence of burning velocity in a spherical combustion bomb," *Symposium (International) on Combustion*, vol. 18, no. 1, pp. 493–501, 1981. Eighteenth Symposium (International) on Combustion.
- [60] V. S. Babkin and L. S. Kozachenko, "Study of normal burning velocity in methane-air mixtures at high pressures," *Combustion, Explosion and Shock Waves*, vol. 2, no. 3, pp. 46–52, 1966.
- [61] T. Iijima and T. Takeno, "Effects of temperature and pressure on burning velocity," *Combustion and Flame*, vol. 65, no. 1, pp. 35–43, 1986.

Bibliography

- [62] M. Metghalchi and J. C. Keck, "Burning velocities of mixtures of air with methanol, isooctane, and indolene at high pressure and temperature," *Combustion and Flame*, vol. 48, pp. 191–210, 1982.
- [63] C. Gößnitzer and H. Steinrück, "Flame propagation in arbitrarily shaped vessels," *PAMM*, vol. 18, no. 1, p. e201800130, 2018.
- [64] M. Matalon, "Flame Propagation in Closed Vessels," in *Modeling in Combustion Science* (J. Buckmaster and T. Takeno, eds.), pp. 163–175, 1994.
- [65] M. Matalon and P. Metzener, "The propagation of premixed flames in closed tubes," *Journal of Fluid Mechanics*, vol. 336, pp. 331—350, 1997.
- [66] Y. Rastigejev and M. Matalon, "Nonlinear evolution of hydrodynamically unstable premixed flames," *Journal of Fluid Mechanics*, vol. 554, pp. 371–392, 2006.
- [67] Y. Rastigejev and M. Matalon, "Numerical simulation of flames as gas-dynamic discontinuities," *Combustion Theory and Modelling*, vol. 10, no. 3, pp. 459–481, 2006.
- [68] R. B. Bird, W. E. Stewart, and E. N. Lightfoot, *Transport Phenomena*. New York: John Wiley & Sons, Inc., revised second ed., 2007.
- [69] C. Gößnitzer and H. Steinrück, "Exact Flame-Front Tracking in Premixed Low Mach Number Combustion," in *Proceedings of the 7th European Conference on Computational Fluid Dynamics* (R. Owen, R. de Borst, J. Reese, and C. Pearce, eds.), pp. 2605–2616, European Community on Computational Methods in Applied Sciences, 2018.
- [70] D. F. Elger, B. C. Williams, C. T. Crowe, and J. A. Roberson, *Engineering Fluid Mechanics*. John Wiley & Sons, Inc., 10th ed., 2014. SI Version.
- [71] C. J. Rallis and A. M. Garforth, "The determination of laminar burning velocity," *Progress in Energy and Combustion Science*, vol. 6, no. 4, pp. 303–329, 1980.
- [72] J. Vancoillie, J. Demuynck, J. Galle, S. Verhelst, and J. A. van Oijen, "A laminar burning velocity and flame thickness correlation for ethanol–air mixtures valid at spark-ignition engine conditions," *Fuel*, vol. 102, pp. 460–469, 2012. Special Section: ACS Clean Coal.
- [73] H. Schneider and C. Proust, "Determination of turbulent burning velocities of dust air mixtures with the open tube method," *Journal of Loss Prevention in the Process Industries*, vol. 20, no. 4, pp. 470–476, 2007. Selected Papers Presented at the Sixth International Symposium on Hazards, Prevention and Mitigation of Industrial Explosions.
- [74] L. Gillespie, M. Lawes, C. G. W. Sheppard, and R. Woolley, "Aspects of Laminar and Turbulent Burning Velocity Relevant to SI Engines," *SAE Technical Papers*, vol. 109, 03 2000.
- [75] J. D. Buckmaster, "An Introduction to Combustion Theory," in *The Mathematics of Combustion* (J. D. Buckmaster, ed.), *Frontiers in Applied Mathematics*, pp. 3–46, SIAM, 1985.
- [76] H. W. Emmons, "Gas Dynamical Aspects of Detonation," in *Fundamentals of Gas Dynamics* (H. W. Emmons, ed.), vol. III of *High Speed Aerodynamics and Jet Propulsion*, pp. 622–686, Princeton University Press, 1958.

Bibliography

- [77] H. W. Emmons, “Flow Discontinuities associated with Combustion,” in *Fundamentals of Gas Dynamics* (H. W. Emmons, ed.), vol. III of *High Speed Aerodynamics and Jet Propulsion*, pp. 584–621, Princeton University Press, 1958.
- [78] J.-Z. Wu, H.-Y. Ma, and M.-D. Zhou, *Vorticity and Vortex Dynamics*. Berlin, Heidelberg: Springer-Verlag, 2006.
- [79] G. K. G. K. Batchelor, *An Introduction to Fluid Dynamics*. Cambridge Mathematical Library, Cambridge University Press, 1967.
- [80] H. S. Tsien, “Influence of flame front on the flow field,” *Journal of Applied Mechanics*, vol. 18, no. 2, pp. 188–194, 1951.
- [81] R. A. Gross, “Low-speed combustion aerodynamics,” *Journal of Jet Propulsion*, vol. 24, no. 2, pp. 95–101, 1954.
- [82] M. Matalon, C. Cui, and J. K. Bechtold, “Hydrodynamic theory of premixed flames: effects of stoichiometry, variable transport coefficients and arbitrary reaction orders,” *Journal of Fluid Mechanics*, vol. 487, p. 179–210, 2003.
- [83] W. D. Hayes, “The vorticity jump across a gasdynamic discontinuity,” *Journal of Fluid Mechanics*, vol. 2, no. 6, pp. 595–600, 1957.
- [84] H. Mache, *Die Physik der Verbrennungerscheinungen*. Veit & Comp., 1918.
- [85] C. C. M. Luijten, E. Doosje, and L. P. H. de Goey, “Accurate analytical models for fractional pressure rise in constant volume combustion,” *International Journal of Thermal Sciences*, vol. 48, no. 6, pp. 1213–1222, 2009.
- [86] K. Saeed, “Evaluation of the Fractional Pressure Rise with Mass Fraction Burned in a Closed Vessel Combustion,” in *Proceedings of the European Combustion Meeting*, Citeseer, 2009.
- [87] S. Nomura and T. Tanaka, “Prediction of Maximum Rate of Pressure Rise Due to Dust Explosion in Closed Spherical and Nonspherical Vessels,” *Industrial & Engineering Chemistry Process Design and Development*, vol. 19, no. 3, pp. 451–459, 1980.
- [88] S. Osher and J. A. Sethian, “Fronts propagating with curvature-dependent speed: Algorithms based on Hamilton-Jacobi formulations,” *Journal of Computational Physics*, vol. 79, no. 1, pp. 12–49, 1988.
- [89] L. L. Erickson, “Panel methods: An introduction,” tech. rep., NASA Ames Research Center, Moffett Field, California, 1990.
- [90] J. Katz and A. Plotkin, *Low-Speed Aerodynamics*. Cambridge Aerospace Series, Cambridge University Press, 2nd ed., 2001.
- [91] T. Cebeci, *An Engineering Approach to the Calculation of Aerodynamic Flows*. Berlin, Heidelberg: Springer-Verlag, 1999.
- [92] L. M. Milne-Thomson, “Elliptic Integrals,” in *Handbook of Mathematic Functions* (M. Abramowitz and I. A. Stegun, eds.), Dover Books on Mathematics, pp. 587–626, New York: Dover Publications Inc., ninth printing ed., 1972.
- [93] F. W. J. Olver, “Bessel Functions of Integer Order,” in *Handbook of Mathematic Functions* (M. Abramowitz and I. A. Stegun, eds.), Dover Books on Mathematics, pp. 355–433, New York: Dover Publications Inc., ninth printing ed., 1972.

Bibliography

- [94] J. H. Gallier and J. Quaintance, *Fundamentals of Linear Algebra and Optimization*. Philadelphia: University of Pennsylvania, 2018. Syllabus of the course CIS 515, Fall 2018.
- [95] L. Greengard, “Potential Flow in Channels,” *SIAM Journal on Scientific and Statistical Computing*, vol. 11, no. 4, pp. 603–620, 1990.
- [96] The OpenMP Architecture Review Board, *OpenMP Application Programming Interface*, 2015. Version 4.5 November 2015.
- [97] R. Lade. personal communication, 2018.
- [98] P. G. J. van der Wel, J. P. W. van Veen, S. M. Lemkowitz, B. Scarlett, and C. J. M. van Wingerden, “An interpretation of dust explosion phenomena on the basis of time scales,” *Powder Technology*, vol. 71, no. 2, pp. 207–215, 1992.
- [99] G. Zhen and W. Leuckel, “Determination of Dust-Dispersion-Induced Turbulence and its Influence on Dust Explosions,” *Combustion Science and Technology*, vol. 113, no. 1, pp. 629–639, 1996.
- [100] Q. Zhang and B. Zhang, “Effect of ignition delay on explosion parameters of corn dust/air in confined chamber,” *Journal of Loss Prevention in the Process Industries*, vol. 33, pp. 23–28, 2015.
- [101] F. W. J. Olver, A. B. O. Daalhuis, D. W. Lozier, B. I. Schneider, R. F. Boisvert, C. W. Clark, B. R. Miller, and B. V. Saunders, “NIST Digital Library of Mathematical Functions.” <http://dlmf.nist.gov/>, Release 1.0.21 of 2018-12-15.
- [102] M. Galassi, J. Davies, J. Theiler, B. Gough, G. Jungman, P. Alken, M. Booth, F. Rossi, and R. Ulerich, *GNU Scientific Library*. GNU, 2016. Version 2.2.1.
- [103] J. J. Dongarra, “Basic Linear Algebra Subprograms Technical (BLAST) forum standard II,” *International Journal of High Performance Computing Applications*, vol. 16, pp. 1–111, 05 2002.
- [104] The HDF Group, *High Level Introduction to HDF5*, 2016. Version of September 23, 2016.
- [105] C. W. Clenshaw and A. R. Curtis, “A method for numerical integration on an automatic computer,” *Numerische Mathematik*, vol. 2, no. 1, pp. 197–205, 1960.
- [106] “SciPy.org Documentation: `scipy.integrate.odeint`.” <https://docs.scipy.org/doc/scipy-0.14.0/reference/generated/scipy.integrate.odeint.html>. accessed on 12 February 2019.

Lebenslauf

Name Clemens Gößnitzer
Geburtsdatum, Geburtsort 12. Juli 1992 in Mödling, Österreich
Staatsbürgerschaft Österreich
Adresse Große Neugasse 22–24/1/15
1040 Wien, Österreich

Schule

1998 – 2002 Volksschule Gänserndorf, Österreich
2002 – 2010 Konrad Lorenz Gymnasium, Gänserndorf, Österreich

Studium

2011 – 2014 Bachelorstudium Verfahrenstechnik, TU Wien, Österreich
Bachelorarbeit: *Expansion of cylindrical shock waves with counterpressure produced by instantaneous release of energy* betreut von Georg Meyer und Herbert Steinrück
2014 – 2016 Masterstudium Verfahrenstechnik, TU Wien, Österreich
Masterarbeit: *Development of a Multicomponent Adsorption Solver in OpenFOAM* betreut von Bahram Haddadi Sisakht, Christian Jordan und Michael Harasek
2016 – 2019 Doktoratsstudium Verfahrenstechnik, TU Wien, Österreich
Dissertation: *Simulation of the Flame-Flow Interaction of Dust Explosions in Closed Vessels* betreut von Herbert Steinrück

Beruf

2010 – 2011 Grundwehrdienst beim Österreichischen Bundesheer
2013 dreimonatiges Praktikum bei Voith Paper Rolls GmbH & Co KG, Wimpassing, Österreich
2016 – 2019 Projektassistent am Institut für Strömungsmechanik und Wärmeübertragung, TU Wien, Österreich